High pressure studies of superconductivity and anomalous normal states in novel quantum materials

Puthipong Worasaran

Department of Physics
University of Cambridge

This dissertation is submitted for the degree of
Doctor of Philosophy

Trinity College August 2021

I would like to dedicate this thesis to my father ...

Declaration

This thesis is the result of my own work and includes nothing which is the outcome of work done in collaboration except as declared in the Preface and specified in the text. I further state that no substantial part of my thesis has already been submitted, or, is being concurrently submitted for any such degree, diploma or other qualification at the University of Cambridge or any other University or similar institution except as declared in the Preface and specified in the text. It does not exceed the prescribed word limit for the relevant Degree Committee.

High pressure studies of superconductivity and anomalous normal states in novel quantum materials

This dissertation contains a wide range of studies of many intriguing physical systems, including a novel incommensurate host-guest structure, strange metal, low-dimensional system, iron-based superconductivity, and a geometrically frustrated magnetic system. We used pressure as the primary tool in our studies, not only as one of the tuning parameters for accessing or tuning away from the quantum critical point but also to enter novel phases that cannot usually be found in any materials at ambient conditions.

Sb (Chapter 4): High-pressure phase Sb-II exhibits a novel incommensurate host-guest structure, giving rise to exotic sliding mode between host and guest chain. In principle, this sliding mode has a very flat dispersion relation perpendicular to the chain, enhancing electron-phonon coupling greatly. This unusual phonon spectrum causes the normal-state resistivity at low temperature to be linear, as previously observed in Bi-III phase. However, it is not the case in Sb-II as it shows a quadratic Fermi liquid-like relation, suggesting the pinning of the phason mode. The phason-pinning is supported by the estimation of electron-phason coupling parameter $\lambda \sim 0.18$, which is surprisingly small. Furthermore, we observed an anomalous first-order transition at a high temperature in resistivity. Combining our results with the experiments from other literature that the interaction between host and guest chain is very strong in Sb-II, we propose that Sb-II may be the first material ever to exhibit Aubry's transition.

Ca_2RuO_4 (Chapter 5): Calcium ruthenate has a long history of studies due to its similarity in structure to cuprates. There are series of transitions in the crystal structure and magnetic ground state under pressure, going from an antiferromagnetic Mott insulator, itinerant ferromagnetic, to unconventional superconductivity. Our experiment has revealed a possibility of a new phase in Ca_2RuO_4. The most prominent features that we observed are (i) a cross-over from the power-law exponent $n = 4/3$ to $n = 1$ in resistivity from below and above 100 kbar (ii) a coexistence between a magnetic ordering and superconductivity. We interpret this to be

a cross-over between itinerant ferromagnetic state and itinerant antiferromagnetic state, or more general, a spin texture state.

YFe_2Ge_2 (Chapter 6): The anomaly in the low-temperature resistivity power-law exponent of the iron-based superconductor YFe_2Ge_2 has posed a question since its discovery. This work aims to answer this question. We found that the application of pressure can completely suppress superconductivity in YFe_2Ge_2. Moreover, the power-law study demonstrates the recovery of Fermi-liquid behaviour at high pressure. Our results support the picture that the exponent $3/2$ in the resistivity power-law temperature dependence emerges from its proximity to the quantum critical regime.

$PdCrO_2$ (Chapter 6): This work aims to explore any possible quantum critical point that may arise in the geometrically frustrated magnet $PdCrO_2$. It is shown that the transition temperature of antiferromagnetic ordering that arises in this system is very much pressure independent. However, resistivity measurement suggests that there may be a structural phase transition to some unknown phase above 80 kbar. The physics of the high-pressure phase are unknown and requires further studies.

Puthipong Worasaran
August 2021

Acknowledgements

First and foremost, I am very grateful to have Malte Grosche as my PhD supervisor. He is very kind, optimistic, enthusiastic, and very knowledgeable. He is always reachable to students, and our Wednesday group meetings have always been enjoyable. I really appreciate so many discussions he has given to me. Thank you also for his 50th birthday dinner - it was such a fantastic event!

I would like to express my deepest appreciation to Patricia Alireza, who always gives me a push and takes care of me in many ways. She trained me in the pressure work, gave me much advice on my health and life, sending me electronic piano during the lockdown, and much more.

I wish to thank Gil Lonzarich for many hours of fruitful discussions on my project. His view of physics really fascinates me, and I have learned so much from talking to him.

My life in QM has been really pleasant because of all my fellows. Jiasheng Chen - who I can always talk to over any matter and gives me many suggestions on my PhD life. Thank you also for having me as a part of many projects. Stephen Hodgson - my main collaborator in our big Sb-project and my chicken burger partner! Oliver Squire and Christian de Podesta always try to drag me out to the lab and journal club when I was writing my thesis. Thank you for our lunchtime together! Jordan Baglo, Keiron Murphy, Konstantin Semeniuk, Aleksandar Vasiljkovic, Thomas Gruner, Cheng Liu, Shiyu Deng, Alexander Eaton, Nicola Kelly, Ivan Kokanovic, Sofia Taylor-Coronel, Sian Dutton, Maximilian Daschner, Matthew Ken Heng, Gilles Rodway-Gant, Nicholas Popiel, Alex Hickey, Alex Davies, Indy Liu, Theo Weinberger, Srinivas Mandyam, Xiaotian Zhang, and Liam Nagle-Cocco - for very pleasant tea time together!

My entire work would not be possible without the funding from Trinity College. I really appreciate for making my study possible.

I would like to thank a small group of my friends, Nakarin Lohitsiri, Neptune Jin, Jiraborrirak Charoenpattarapreeda, Orarat Ginsawaeng, and Methawi Chomthong. We shared weekends doing many fun things together in Cambridge.

I would also like to extend my deepest gratitude to my family. My father raises my brother and me so well on his own after my mother passed away 23 years ago - thank you so much. Also, thanks to my brother - I am so lucky to have him as a brother!

Last but not least, I'm deeply indebted to my girlfriend, Gift Mungmeeprued, who always stays by my side and gives me so much love and support. She also has a lot of contributions to this thesis. Many figures are made with her help, and she also helps with the fitting. Thank you for being together all along; I really love our time together :)

Table of contents

List of figures

List of tables

Chapter 1

Introduction

Condensed matter physics (CMP) is one of the most active fields in physics. A condensed matter system is so complicated, which makes it so rich. The complexity of an exact calculation for any system is way beyond the ability of any human ever existed or even the most powerful computer available to date. However, this does not mean we cannot gain insights into such systems. Instead of focusing on and tracking every particle in a system, one has to adapt their point of view to focus on important degrees of freedom and interactions. Because of these complications, it usually happens that condensed matter physicists gain insights from experimental results then write down theories rather than getting a theory out purely from a mathematical point of view. This links theoretical CMP and experimental CMP very strongly compared to other branches in physics - high energy and general relativity, to name a few. As an experimentalist, we identify interesting materials and study various aspects of them, such as transport properties, thermodynamics properties, optical properties, and fermiology.

One interesting question is what happens to materials when we fine-tune them. There are a few ways to tune material, such as hydrostatic pressure, uniaxial strain, chemical doping, chemical substitution, and external fields. The role of hydrostatic pressure is to change the lattice constant. Consequently, it alters the wavefunction overlap, hopping parameter, and hence kinetic energy. In a strongly correlated system where there is competition between kinetic energy and interactions, pressure can fine-tune these parameters. Most of the time, pressure can drive materials to different phases, such as a magnetic phase, superconducting phase, or even a complete change in the crystal structure. The role of pressure alone gives us so many intriguing results in both fundamental studies and technological applications. For example, pressure can be used as a fine-tune parameter in quantum phase transition studies

[125]. Furthermore, carbonaceous sulfur hydride has been discovered to be room-temperature superconductivity under pressure [132].

In this dissertation, we studied four materials under a high-pressure environment. The first material is element Sb (antimony). At high pressure, antimony undergoes a structural transition and becomes an incommensurate host-guest crystal. Superconductivity in this Sb-II phase is believed to be mediated by phason. The very flat dispersion of phason gives rise to a large McMillan parameter, making the system an excellent place to study strong-coupling superconductivity. The second material is Ca_2RuO_4. There has been a long history of Sr_2RuO_4 for a few reasons: (i) It has the same structure as the cuprate (ii) Although not yet settled, it has an exotic order parameter, either p-wave [120] or multi-component [57]. The Ca-substitute version, Ca_2RuO_4, introduces distortions to the prototype Sr_2RuO_4. As it was speculated that high-pressure Ca_2RuO_4 should have a similar physics to Sr_2RuO_4 [98], we desire to study high-pressure Ca_2RuO_4 in greater detail. The third material is YFe_2Ge_2, which is an iron-based superconductor. The ability to grow high-quality YFe_2Ge_2 makes the material suitable for definitive studies. The last material is $PdCrO_2$, which is a geometrically frustrated magnet. It is natural to investigate the effect of pressure on the antiferromagnetic ordering that arises from the frustrating system, especially if we can suppress the magnetic order. Since there are many materials to review, we decide to give more detailed introductions at the starting of each chapter.

Chapter 2

Basic Notions

In this chapter, we discuss basic concepts in condensed matter physics that are related to our materials.

2.1 Landau-Fermi Liquid Theory

In the early condensed matter era, physicists explain metal, semi-conductor, and insulator using band theory. In this picture, insulators are materials whose chemical potential lies at an energy gap, unlike metals where the chemical potential is located far from any energy gap. For metals, we can also model the conduction electron subsystem as a non-interacting electron system (or electron gas) in a box (imagine our sample to be a container for conduction electrons). Then, we can find the ground state by solving the one-particle Schrödinger equation and implementing Pauli's exclusion principle. In the ground state, electrons form a three dimensional-ball (B^3) in k-space, called the Fermi sphere. The boundary of this ball is called the Fermi surface. The electrons that contribute to the electronic properties are only close to this Fermi surface (within the energy scale $\sim k_B T$) due to Pauli's exclusion principle that electrons deep down in the Fermi sphere are frozen.

However, this Fermi gas model is not complete because it does not consider the strong Coulomb's interaction between electrons. The Fermi liquid theory (invented by a Russian physicist Lev Landau - so it is sometimes called the Landau-Fermi liquid) corrected the Fermi gas model by taking into account the electron-electron interaction (hence the name Fermi liquid)! To appreciate the difficulty when we have this interaction, we quote the full

Hamiltonian

$$H = \sum_i \left(-\frac{\hbar^2}{2m}\nabla^2 + U(\boldsymbol{r}_i) \right) + \sum_{i<j} \frac{q^2}{4\pi\varepsilon_0 |\boldsymbol{r}_i - \boldsymbol{r}_j|} \tag{2.1}$$

With the interaction term, the Hamiltonian is not diagonalisable in terms of single-particle states, and there is no way to solve this exactly. How can we understand such a system then? The main idea here is the concept of *quasiparticle*. In the Fermi gas system, we can set the ground state as our vacuum (which is, of course, different from the real vacuum).

$$|\Omega_0\rangle : n_{\boldsymbol{p}\sigma} = \begin{cases} 1, \text{ if } |\boldsymbol{p}| \leqslant p_F \\ 0, \text{ if } |\boldsymbol{p}| > p_F \end{cases}$$

There are two types of elementary excitations of the system, *electrons* and *holes*.

$$\text{Single Electron State} : c^\dagger_{\boldsymbol{p}\sigma} |\Omega_0\rangle \text{ where } |\boldsymbol{p}| > p_F$$
$$\text{Single Hole State} : c_{\boldsymbol{p}\sigma} |\Omega_0\rangle \text{ where } |\boldsymbol{p}| \leqslant p_F$$

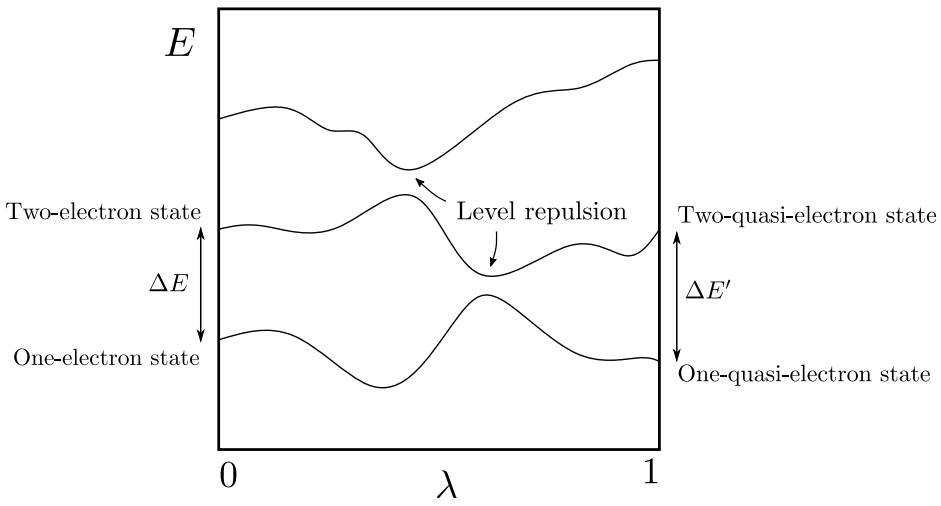

Fig. 2.1 The evolution of the energy levels of the free electron system to the interacting electron system.

Now, we turn on the interactions adiabatically. By that, we mean turning on the interactions very slowly (imagine we have Hamiltonian $H = H_0 + \lambda H_I$ and vary λ slowly from

zero to unity). A question arises naturally, what happens to these elementary excitations? Are they still well defined in the presence of interactions? To answer this question, we look at what happens to the system's energy levels as we turn on the interactions. Figure 2.1 shows the energy levels of three different states - one, two and three-electron states (by electron, we mean the elementary excitation as explained above, not referring to the actual electrons in solid in this sense). Now, going from the one-electron state to the two-electron state costs energy ΔE. This energy comes from adding a particle into the system. As we tune λ from 0 to 1, we would not expect a *level crossing* if our system is far from phase transition. The reason is that, as the levels come close to each other, the second-order term in the perturbation theory will make those two states repel each other. However, this is not true if the matrix element between those states is zero, and it is the case if the system undergoes phase transition because both states have different symmetries in the ground state. (Actually, not all continuous phase transitions break the symmetry of a system. The symmetry breaking picture comes from Ginzberg-Landau theory of phase transition only. Renormalisation analysis shows that the symmetries of two fixed points can be the same [156]. Topological phase transition is an example of this). When λ approaches unity, we arrive at the right side of the diagram. Since there is no level crossing, the state that used to be the one-electron state still has lower energy than the state that used to be the two-electron state (this applies to all other states), suggesting that we still have a well-defined particle-like excitation and $\Delta E'$ is the energy cost for putting this particle into our system. Since this new particle may have different properties from the original particle, we call them a quasiparticle. With the presence of interaction, electron evolves into quasi-electron, and hole evolves into quasi-hole. This is a beautiful one-to-one correspondence in Landau-Fermi Liquid theory!

Now, we would like to understand these quasiparticles better. We need to do everything more rigorously. Since we have quasi-electron and quasi-hole, which are particle-antiparticles, it is only natural for us to use the quantum field theory framework. The partition function for the free fermion system with the source terms at zero temperature is [5, 43, 86]

$$\begin{aligned}\mathscr{Z}_0 &= \int \mathscr{D}(\psi,\psi^*)\exp\left[i\int_0^t dt \sum_{\boldsymbol{k}}\left(i\psi_{\boldsymbol{k}}^*\dot{\psi}_{\boldsymbol{k}} - \xi_{\boldsymbol{k}}\psi_{\boldsymbol{k}}^*\psi_{\boldsymbol{k}} + j_{\boldsymbol{k}}^*\psi_{\boldsymbol{k}} + j_{\boldsymbol{k}}\psi_{\boldsymbol{k}}^*\right)\right] \\ &= \int \mathscr{D}(\psi,\psi^*)\exp\left[i\int_0^t dt \sum_{\boldsymbol{k}}\left(\psi_{\boldsymbol{k}}^*(i\partial_t - \xi_{\boldsymbol{k}})\psi_{\boldsymbol{k}} + j_{\boldsymbol{k}}^*\psi_{\boldsymbol{k}} + j_{\boldsymbol{k}}\psi_{\boldsymbol{k}}^*\right)\right]\end{aligned} \tag{2.2}$$

where $\psi_{\boldsymbol{k}}$ and $\psi^*_{\boldsymbol{k}}$ are anti-commuting Grassmann variables. Since the Green function is defined to be a time-ordered two-point correlation function

$$iG^{(0)}(\boldsymbol{k}, t-t') = \langle \psi_{\boldsymbol{k}}(t)\psi^*_{\boldsymbol{k}}(t')\rangle \tag{2.3}$$

we see that it is just a second derivative of the partition function with respect to the source terms

$$iG^{(0)}(\boldsymbol{k}, t) = -\frac{1}{\mathscr{Z}_0}\frac{\partial^2}{\partial j_{\boldsymbol{k}}\partial j^*_{\boldsymbol{k}}}\mathscr{Z}_0 \tag{2.4}$$

The partition function can be calculated using Gaussian integration,

$$\mathscr{Z}_0 = \mathscr{Z}_0(\boldsymbol{j}=0)\exp\left(\boldsymbol{j}^\dagger(i\partial_t - \xi_{\boldsymbol{k}})^{-1}\boldsymbol{j}\right) \tag{2.5}$$

We obtained the Green function immediately to be the inverse of the operator $(i\partial_t - \xi_{\boldsymbol{k}})$. Hence,

$$(i\partial_t - \xi_{\boldsymbol{k}})G^{(0)}(k, t-t') = \delta(t-t') \tag{2.6}$$

In the frequency space, we finally have

$$G^{(0)}(\boldsymbol{k}, \omega) = \frac{1}{\omega - \xi_{\boldsymbol{k}}} \tag{2.7}$$

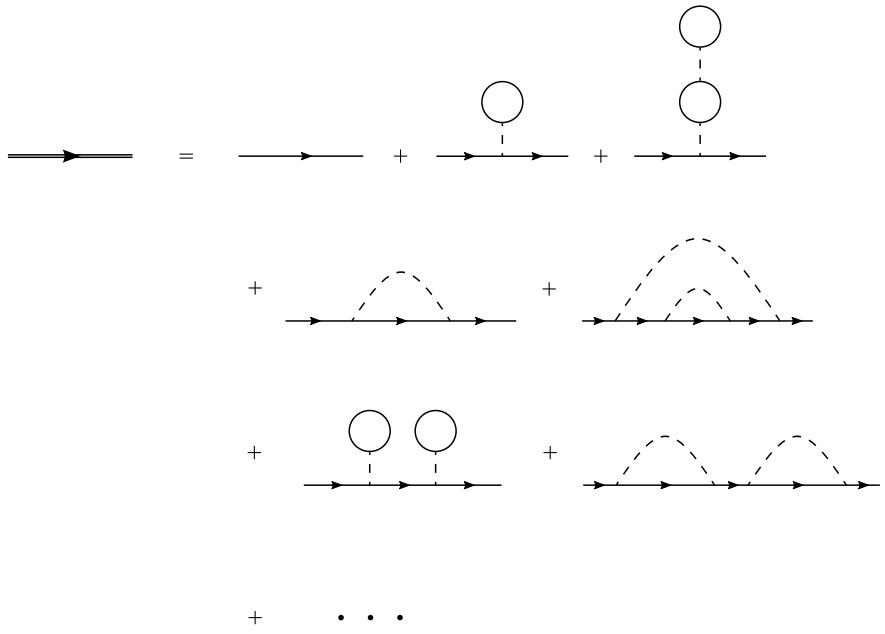

Fig. 2.2 Feynman diagrams of the interacting fermions.

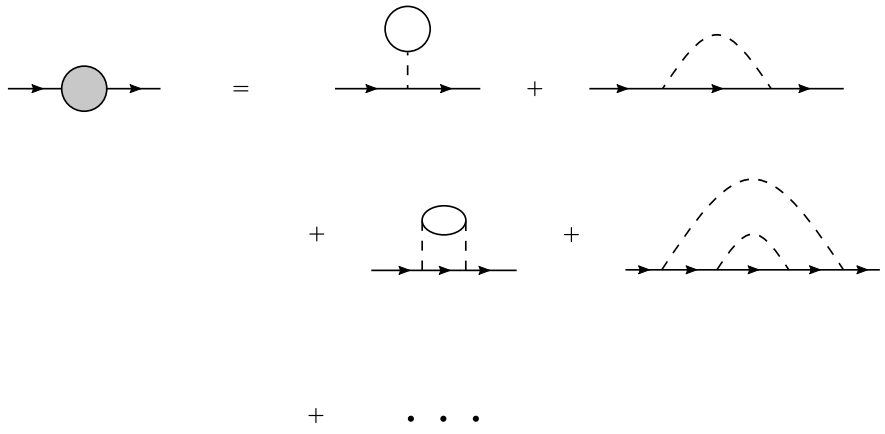

Fig. 2.3 1PI diagrams.

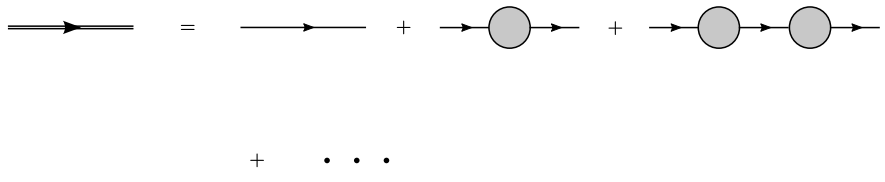

Fig. 2.4 Dressed propagator as an infinite sum of 1PI diagrams.

When the interaction is turned on, the propagator is modified by interactions. It is easier to write down the Feynman diagram rather than explaining things in words at this stage. Here, the single line propagator represents a bare electron, the dash line represents interaction between electrons, and the double line propagator represents a particle dressed by the interactions.

Some of the Feynman diagrams in figure 2.2 can be reduced into two or more diagrams connected by a single propagator in series. A diagram that cannot be reduced further is called a *1-part irreducible diagram* (or 1PI diagram). The 1PI diagram is represented as a shaded blob. The first few terms in the 1PI diagram are shown in figure 2.3. Finally, the dressed propagator can be written as an infinite summation of 1PI diagrams connected in series, as shown in figure 2.4. Denote the 1PI self-energy diagram by $\Sigma(\boldsymbol{k},\omega)$. The interacting Green function in momentum space becomes

$$\begin{aligned} G(\boldsymbol{k},\omega) =& G^{(0)}(\boldsymbol{k},\omega) + G^{(0)}(\boldsymbol{k},\omega)\Sigma(\boldsymbol{k},\omega)G^{(0)}(\boldsymbol{k},\omega) \\ &+ G^{(0)}(\boldsymbol{k},\omega)\Sigma(\boldsymbol{k},\omega)G^{(0)}(\boldsymbol{k},\omega)\Sigma(\boldsymbol{k},\omega)G^{(0)}(\boldsymbol{k},\omega) + \cdots \end{aligned} \tag{2.8}$$

The result of this sum is (we absorbed the $i\varepsilon$ description into the self-energy)

$$G(\boldsymbol{k},\omega) = \frac{1}{\left(G^{(0)}(\boldsymbol{k},\omega)\right)^{-1} - \Sigma(\boldsymbol{k},\omega)} \tag{2.9}$$

What does this equation tell us? Before that, we need to give two remarks about the quasiparticles. Firstly, the momentum of a quasiparticle does not change in turning on interactions because momentum is quantised due to a constrain in boundary conditions. Since adiabatic evolution is very slow, it will not cause a quasiparticle to jump from one momentum state to another. We can conclude that the momentum of quasiparticles does not change by the interactions. Secondly, quasiparticles are only well defined close to the Fermi surface. Why? It is because they are not free. They are allowed to interact with each other via 4-legs Feynman diagrams, meaning that a quasiparticle can disintegrate into a bunch of quasi-electrons and quasi-holes. Thus, they have a finite lifetime - and if their lifetimes are too short, we cannot say they behave like a well-defined particle anymore. When a quasiparticle is very close to the Fermi surface, however, its lifetime becomes very long because the phase-space volume of the final state after its disintegration is small (and that suppressed the scattering amplitude). Then, we can consider the wave vector to be very close to the Fermi wave vector throughout the analysis. The interacting Green function can then be

written as

$$G(\boldsymbol{k},\omega) = \frac{1}{\omega - v_F(k-k_F) - \Sigma(\boldsymbol{k},\omega)} \tag{2.10}$$

which has a pole at $\omega_p = v_F(k-k_F) + \Sigma(\boldsymbol{k},\omega_p)$. This is, of course, the dispersion relation of a quasi-particle. From the 1-1 correspondence between particle and quasi-particle, we know that $\omega_p|_{k=k_F} = 0$. This means ω_p can be written as

$$\omega_p = v_F^*(k-k_F) \tag{2.11}$$

where k is close to k_F. The effective Fermi velocity is

$$\begin{aligned} v_F^* = \frac{\partial \omega_p}{\partial k} &= \frac{\partial}{\partial k}\left(v_F(k-k_F) + \Sigma(k,\omega_p)\right) \\ &= v_F + \frac{\partial}{\partial k}\Sigma(k, v_F^*(k-k_F)) \\ &= v_F + \frac{\partial}{\partial k}\left[\Sigma(k,0) + v_F^*(k-k_F)\frac{\partial\Sigma(k,\omega)}{\partial\omega}\bigg|_{\omega=0}\right] \\ &= v_F + \frac{\partial\Sigma(k,0)}{\partial k} + v_F^*\frac{\partial\Sigma(k,\omega)}{\partial\omega}\bigg|_{\omega=0} \end{aligned} \tag{2.12}$$

By defining

$$Z \equiv \left(1 - \frac{\partial\Sigma(k,\omega)}{\partial\omega}\bigg|_{\omega=0}\right)^{-1} \tag{2.13}$$

the effective Fermi velocity becomes

$$v_F^* = Z\left(v_F + \frac{\partial\Sigma(k,0)}{\partial k}\right) \tag{2.14}$$

If the self-energy does not depend on the momentum, the effective mass of the particle reads

$$m^* = \frac{m}{Z} \tag{2.15}$$

The behaviour of the Green function in 2.10 is not very clear since the self-energy term also contains ω in it. To understand this Green function, we consider its behaviour around the pole by expanding the self-energy around ω_p

$$\Sigma(k,\omega) = \Sigma(k,\omega_p) + (\omega-\omega_p)\left(\frac{\partial\Sigma}{\partial\omega}\right)_{\omega=\omega_p} \tag{2.16}$$

the denominator is

$$\begin{aligned}\omega - v_F(k-k_F) - \Sigma(k,\omega) &= \omega - v_F(k-k_F) - \Sigma(k,\omega_p) - (\omega-\omega_p)\left(\frac{\partial\Sigma}{\partial\omega}\right)_{\omega=\omega_p} \\ &= \omega-\omega_p-(\omega-\omega_p)\left(\frac{\partial\Sigma}{\partial\omega}\right)_{\omega=\omega_p} \\ &\approx Z^{-1}(\omega-\omega_p)\end{aligned} \tag{2.17}$$

Substitute this into the Green function, we finally obtained

$$G(\boldsymbol{k},\omega) = \frac{Z}{\omega - v_F^*(k-k_F)} \tag{2.18}$$

where $Z = (1-(\partial\Sigma/\partial\omega_p))^{-1}$ and $v_F^* = p_F/m^*$. The denominator of the Green function confirms the particle behaviour of a quasi-particle, and effectively, it has a mass m^*. The effect of having interactions is equivalent to changing the mass. This is a remarkable result from Landau-Fermi liquid theory.

We have to be very careful because the Green function here contains only one part of the full Green function. The part that we quoted here is called the coherence Green function, and the incoherence Green function part was ignored. Where did the incoherent part go? We have to go back to the definition of the Green function. The non-interacting Green function is defined as

$$G^{(0)}(x-x',t-t') = \langle\Omega_0|\,T\,\psi(x,t)\psi^\dagger(x',t')\,|\Omega_0\rangle \tag{2.19}$$

which contains the term $\psi^\dagger(x,t)\,|\Omega_0\rangle$. In the non-interacting theory, this term is interpreted as a state of a single particle at the position (x,t) in spacetime. The interpretation of this non-interacting Green function is thus the probability amplitude to find a particle at (x,t) given that it was at (x',t') initially. Therefore, this corresponds to a single propagator line. When we go to the interacting theory, we evolve $|\Omega_0\rangle \to |\Omega\rangle$ but leave ψ and $\psi^\dagger$ unchanged. It is here that we missed the incoherence part. We know that the action of operators $(\psi,\psi^\dagger)$ to $|\Omega_0\rangle$ is to create a single hole or a single electron in the free theory, but that does not mean they create just only one quasi-particle when they act upon the interacting ground

state $|\Omega\rangle$! For instance, $\psi_{\boldsymbol{k}}^{\dagger}|\Omega\rangle$ also contains terms like two quasi-electrons plus one quasi-hole or three quasi-electrons plus two quasi-holes (or even 101 quasi-electrons plus 100 quasi-holes!). It contains many terms as long as the number of quasi-electrons minus the number of quasi-holes is one and the total momentum is $\boldsymbol{k}$. Accordingly, the interacting Green function must contain diagrams with many external legs (for example, three incoming quasiparticles and five outgoing quasiparticles, as shown in figure 2.5). These diagrams contribute to the incoherence part, and since they do not contain a particle with definite momentum (particles can exchange momenta with each other), we expect no singularity in this part. Consequently, the incoherence Green function only contributes to a smooth background in the full Green function. Finally, equation 2.18 gets modify to be (now, we also put the lifetime of a quasi-particle back into the imaginary part of the denominator)

$$G(\boldsymbol{k},\omega)=\frac{Z}{\omega-v_F^*(k-k_F)+i\tau\,\mathrm{sign}(k-k_F)}+\text{ (Smooth Background From Incoherence Part).} \tag{2.20}$$

By doing Fourier transform from frequency space to time on this Green function, one gets the number density of the real electrons in solid (why real electrons rather than quasi-particles? It is because $\psi^{\dagger}$ is the operator that create a real electron, and when it appears in $\langle\Omega|\,\psi^{\dagger}\psi\,|\Omega\rangle$, it counts the number of the real electrons),

$$n_{\boldsymbol{k}}=iG(\boldsymbol{k},t=0^{-}) \tag{2.21}$$

This becomes

$$n_{\boldsymbol{k}}=Z\theta(k_F-k)+(\text{Smooth Background}) \tag{2.22}$$

The plot of the number density as a function of wave vector is shown in figure 2.6. There is still a discontinuity at the Fermi surface with a size Z. This is the distribution at zero temperature (or ground state) of electrons. If one asks for the distribution of quasi-particle in the ground state, it is even easier to answer - there is no quasi-particle at zero temperature because the lowest energy state is the one without any quasi-particle!

By the same analogy to the renormalisation of the electron propagator, we also need to renormalise the interaction line. The result of doing so will modify the long-range interaction to be exponential short-range. This effect is the so-called Thomas-Fermi screening

The notion of the dressed particle is crucial since it gives the new language in which one can understand the physics of the system much more easily. For instance, the electron-

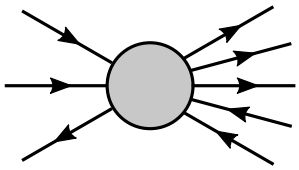

Fig. 2.5 An example of a diagram in the incoherence Green function.

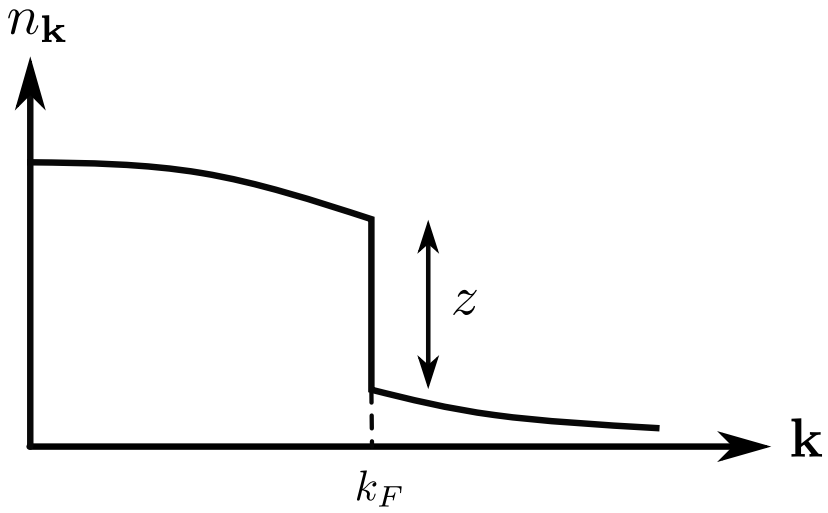

Fig. 2.6 Number density as a function of wave vector.

electron scattering can be calculated by just looking at how much phase space electrons occupy after their collision (by treating them as if they are free), and it contributes to the resistivity[1] at low temperature by the amount of $\rho_{e-e} \sim T^2$. The other important thing is the ability to explain how quantum oscillation happens in Fermi liquid[2].

To end the section on Fermi liquid theory, let's look briefly how we can obtain $\rho_{e-e} \sim T^2$. As we already discussed the notion of quasiparticle earlier, we can use the quasiparticle picture to calculate scattering rate. The most intuitive method to prove the T^2 power-law would be to use the phase space argument. A scattering of two particles $1+2 \to 3+4$ is equivalent to a decay of one particle into a hole and two particles $1 \to \bar{2}+3+4$. If the

[1]This way of explaining the T^2 law in resistivity does not sound correct but somehow gives the correct result. This should not be correct because the scattering between two electrons is elastic - meaning that there must not be any energy or momentum lost, and hence this scattering should not contribute to the resistivity. The correct explanation to this matter is still not settled despite the theory being developed since 1956. One possible explanation is that the electron-electron scatterings enhance them to scatter off with defects or phonons (defects destroy the discrete translational symmetry and hence the crystal momentum no longer conserves).

[2]This, on the other hand, does not give any prediction on other systems (it does not say that quantum oscillation should be seen in only Fermi liquid system). For instance, the quantum oscillation has also been observed in topological insulators such as SmB_6 [61]

energy of particle 1 is fixed to be E_1, the energy of other three particles have to lie within the shell of energy $(E_1 - E_F)$ from the Fermi surface. Quasiparticles 2 and 3 have freedom to choose energy within this region, and quasiparticle 4 is fixed by the conservation of energy. Therefore, the scattering rate must be proportional to $(E_1 - E_F)^2$ (which is the volume of phase space). At finite temperature T, the Fermi surface is smeared by thermal broadening, meaning that $(E_1 - E_F)$ is in the order of $k_B T$. Thus, resistivity is proportional to T^2.

2.2 Non-Fermi Liquid

Although Fermi liquid theory has succeeded in explaining low-temperature behaviour of various metallic materials, it fails to capture physics of many compounds such as the metallic phase in an underdoped [75] and overdoped [161] cuprate. The non-Fermi liquid criterion is reflected in the transport behaviours, such as resistivity, thermal conductivity, and optical conductivity. In resistivity measurement, we have non-Fermi liquid whenever resistivity at low tempemrature is not proportional to T^2. The early theory that tried to capture the non-Fermi liquid is called the 'marginal Fermi liquid theory' [148]. In Fermi-liquid, we have a well-defined peak in spectral representation. The width of the peak is determined by the imaginary part of self-energy term. To obtain a well-defined peak, we require that $\lim_{\omega\to 0} \mathrm{Im}\Sigma(\omega) = 0$ and is an even function. Therefore, $\mathrm{Im}\Sigma(\omega) \propto \omega^2$ to the lowest order of expansion. The real part of the self-energy can be obtained by the aids of Kramer-Kronig relations, which gives $\mathrm{Re}\Sigma(\omega) \propto \omega$ [26, 41]. On the other hand, the concept of a well-defined quasiparticle does not hold in non-Fermi liquid, meaning that the renormalisation Z must vanish to destroy the peak in spectral function $A(\omega)$. To get $Z = 0$, we need the differential $d\Sigma/d\omega$ to diverge at $\omega = 0$. For this condition to be met, Varma [148] proposed the self-energy to be $\mathrm{Im}\Sigma(\omega) \propto |\omega|$ and $\mathrm{Re}\Sigma(\omega) \propto \omega \ln|\omega|$. It is worth noting that this way of getting self-energy is purely by the phenomenological mean.

One of the important factors that breaks down the quasiparticle description is the existence long-range interaction between quasiparticles (another requirement is that the interaction must be repulsive in nature), which increases the scattering rate at low temperature and increase the width of the peak in spectral function [131]. When the system is at the border of magnetism, electrons interact via long-range spin-spin interaction. One of the standard approaches to deal with these systems is the *self-consistent renormalisation (SCR) theory*. This theory is essentially an effective theory where the fermionic field is integrated out, leaving with only local magnetisation $\boldsymbol{m}(\boldsymbol{r},t)$ as a dynamical variable [82]. The results

from SCR theory that will be related to out work is the power-law exponent in the transport measurements, which is as follows [87]:

1. At the critical boundary of the ferromagnetic phase at zero temperature, the resistivity follows the T^2-law with diverging A-coefficient. The temperature range for the T^2-law also shrinks to zero as the boundary is approached.

2. In 2D ferromagnetic, resistivity follows $R \sim T^{4/3}$, whereas 3D ferromagnetism gives $R \sim T^{5/3}$.

3. In 2D antiferromagnetic, resistivity follows $R \sim T$, whereas 3D antiferromagnetism gives $R \sim T^{3/2}$.

Note that the power-law behaviour above holds only when there is no magnetic long-range order. When there is a magnetic order presence in a system, the situation becomes very complicated and the exact form of resistivity is sensitive to the anisotropy on magnetic moments. However, if the magnon's dispersion relation is gapped, we expect the exponential (activation like) behaviour in resistivity. Therefore, the qualitative features in resistivity profile would not be very sentitive to the anisotropy. In the presence of strong uniaxial anisotropy, the contribution from the scattering with ferromagnetic reads [6, 55]

$$\rho_{FM} \propto T\Delta \left[1 + \frac{2T}{\Delta}\right] e^{-(\Delta/T)} \tag{2.23}$$

whereas the contribution from the scattering with antiferromagnetic reads [55]

$$\rho_{AFM} \propto \Delta^2 \sqrt{\frac{T}{\Delta}} \left[1 + \frac{2}{3}\left(\frac{T}{\Delta}\right) + \frac{2}{15}\left(\frac{T}{\Delta}\right)^2\right] e^{-(\Delta/T)} \tag{2.24}$$

2.3 Superconductivity

One of the most significant achievements in twentieth-century condensed matter physics is undeniably the discovery of superconductivity and the theory behind it. Superconductivity was first discovered in Mercury by Onnes in 1911, but it took almost half a century to understand the phenomenon. In those fifty years, many great physicists, such as Einstein, Heisenberg, Landau, Feynman, Born, and many more, have attempted to solve the mystery of superconductivity, but they failed. This in itself tells us how difficult this subject is. Then,

in 1957, three physicists, Bardeen, Cooper, and Schrieffer, proposed the microscopic theory of superconductivity, and the theory is named after them - the BCS theory!

The rough idea of the superconductivity is that electrons at the opposite side of Fermi surface[3], with the opposite spin, pair up together. This makes the excitation become gapped and causes a dissipationless flow

2.3.1 Phenomenological Approach

As the order parameter in a superconductor can be represented by a complex wave function[4] ψ, the Ginzberg-Landau free energy is

$$f(\psi,\boldsymbol{A}) = f_0 + \alpha|\psi|^2 + \frac{\beta}{2}|\psi|^4 + \frac{1}{2m}\left|(i\hbar\nabla - q\boldsymbol{A})\psi\right|^2 + \frac{1}{2\mu_0}(\nabla\times\boldsymbol{A} - \nabla\times\boldsymbol{A}_E)^2 \quad (2.25)$$

where $\boldsymbol{A}_E$ is a vector potential corresponding to an external field. By minimising the free energy with respect to ψ and $\boldsymbol{A}$, we obtained the so-called Ginzberg-Landau equations. The first GL equation reads

$$\frac{1}{2m}(-i\hbar\nabla - q\boldsymbol{A})^2\psi + (\alpha + \beta|\psi|^2)\psi = 0 \quad (2.26)$$

and the second GL reads

$$\boldsymbol{J}_s = \frac{n_s q^2}{m}\left(\frac{\hbar}{q}\nabla\theta - \boldsymbol{A}\right) \quad (2.27)$$

where $\boldsymbol{J}_s$ is superconducting current and θ is the phase in the superconducting wave function.

From these two GL equations, one can see that there are two length scales involved. The first one is the coherence length, which associates with the first GL equation. It tells us how fast the wave function can vary in inhomogeneous superconductivity (for example, how fast the wave function grows from zero at the surface to a constant value in bulk). The coherence length is defined to be

$$\xi = \left(\frac{\hbar^2}{2m|\alpha|}\right)^{1/2} \quad (2.28)$$

[3]The reason it has to be opposite is to maximise the phase space of both electrons after the scattering. If they are not opposite to each other, the phase space of states after collision gets significantly suppressed due to the momentum conservation constraint.

[4]This complex wave function ψ is interpreted as the wave function of centre of mass of a Cooper pair.

The second length scale associated with the second GL equation is the penetration depth, which tells us how far the magnetic field can penetrate into the superconducting bulk. The penetration depth is given by

$$\lambda = \left(\frac{m}{\mu_0 n_s q^2} \right)^{1/2} \tag{2.29}$$

The non-zero penetration depth tells us that superconductors expel flux, and the magnetic field should be zero in bulk - this is called the 'Meissner state'. However, it is possible to lower the GL free energy by letting a quantum flux pass through the superconductor in some circumstances. Doing so lowers the field energy but raises the stiffness energy (the gradient term) - this is called the 'vortex state'. When the field is very close to zero, the system is always in the Meissner state. When the external field is large enough, the vortex state is preferred. This critical field is given by

$$B_{c1} = \frac{\phi_0}{4\pi\lambda^2} \tag{2.30}$$

where $\phi_0 = h/2e$ is the quantum of flux. When the field is increased further, there will be more and more vortices in the material, and they finally form vortex lattice due to the vortex-vortex repulsion - this is called the 'Abrikosov flux lattice'. The lattice gets squeezed as the external field is larger (since there are more vortices). Once the lattice parameter reaches the coherence length, it loses the screening completely and, hence, is not superconducting anymore. This critical field is defined by

$$B_{c2} = \frac{\phi_0}{2\pi\xi^2} \tag{2.31}$$

It is clear that there should be two types of superconductors. Type-I superconductor is the one with $B_{c1} > B_{c2}$. This means that the vortex state does not exist in this type, and it goes from Meissner state to normal state directly under applied magnetic field. Type-II superconductor, in contrast, happens when $B_{c1} < B_{c2}$. The transitions in field of this type undergo from Meissner state to vortex state and finally normal state. These criteria can be translated into a dimensionless parameter $\kappa \equiv \lambda/\xi$. If $\kappa < 1/\sqrt{2}$, it is type-I superconductor. If $\kappa > 1/\sqrt{2}$, it is type-II superconductor.

2.3.2 Microscopic Description

Weak Coupling Limit

Although the GL phenomenological approach can predict a few superconductors' propertiess, it does not explain how superconductivity forms. To begin with, the interacting Hamiltonian in the Grand canonical ensemble casts the form.[5,6]

$$H = \sum_{\boldsymbol{k}} (\varepsilon_{\boldsymbol{k}} - \mu) a^{\dagger}_{\boldsymbol{k}\sigma} a_{\boldsymbol{k}\sigma} + \frac{g}{2V} \sum_{\boldsymbol{k}\boldsymbol{k}'\boldsymbol{q}} a^{\dagger}_{\boldsymbol{k}+\boldsymbol{q},\sigma} a^{\dagger}_{\boldsymbol{k}'-\boldsymbol{q},\sigma'} a_{\boldsymbol{k}'\sigma'} a_{\boldsymbol{k}\sigma} \tag{2.32}$$

In the mean field approximation where the fluctuation of the system is neglected, the effective Hamiltonian becomes

$$H_{\text{eff}} = \frac{1}{2} \sum_{\boldsymbol{k}} \left[\xi_{\boldsymbol{k}} \left(a^{\dagger}_{\boldsymbol{k}\sigma} a_{\boldsymbol{k}\sigma} + a^{\dagger}_{-\boldsymbol{k}\sigma} a_{-\boldsymbol{k}\sigma} \right) + \Delta \left(a^{\dagger}_{\boldsymbol{k}\uparrow} a^{\dagger}_{-\boldsymbol{k}\downarrow} + a_{\boldsymbol{k}\uparrow} a_{-\boldsymbol{k}\downarrow} \right) \right] \tag{2.33}$$

where the diagonal terms absorb both direct and exchange terms, and the off-diagonal terms are Bogoliubov terms. By diagonalising[7] H_{eff}, the energy spectrum shows the energy gap of 2Δ at the chemical potential. Thus, we can interpret parameter Δ to be the energy gap of the Bogoliubov excitation. By looking at the full Hamiltonian, we can see immediately that the energy gap is

$$\Delta = \frac{g}{V} \sum_{\boldsymbol{k}} \langle a_{-\boldsymbol{k}\downarrow} a_{\boldsymbol{k}\uparrow} \rangle \tag{2.34}$$

In the diagonal basis, the new creation and annihilation operators obey the anticommutation relation, suggesting the Fermi-Dirac distribution at finite temperature. Therefore, by evaluating the energy gap in the diagonal basis, one arrives at the expression

$$\Delta = \frac{|g|}{V} \sum_{\boldsymbol{k}} \frac{\Delta}{2E_{\boldsymbol{k}}} \left(1 - 2f(E_{\boldsymbol{k}}) \right) \tag{2.35}$$

[5]The ω and $\boldsymbol{k}$ independent coupling constant is a good approximation in the case of phonon mediated superconductor. Since the estimated form of the effective potential is proportional to $(\omega^2 - \omega_D^2)^{-1}$ and the Debye frequency is generally much larger than the temperature scale we usually consider, it means we can treat the potential to be just a constant.

[6]Einstein's summation convention is applied here in the spin indices.

[7]By using Bogoliubov transformation.

where $E_{\boldsymbol{k}} = \sqrt{\xi^2 + \Delta(T)^2}$. By changing the discrete summation into the integration, we obtain the self-consistent equation, called the 'BCS gap equation'

$$1 = |g| \int_0^{\hbar\omega_D} d\xi \mathscr{N}(\xi) \frac{1}{\sqrt{\xi^2 + \Delta(T)^2}} \tanh\left(\frac{\sqrt{\xi^2 + \Delta(T)^2}}{2k_B T}\right) \tag{2.36}$$

where $\mathscr{N}(\xi)$ is the density of state. This equation has to be solved numerically. However, one can extract some useful information by considering two limiting cases. The first one is $\Delta(T) \to 0$, which happens when the temperature reaches the critical temperature T_c. Plug in this condition to the gap equation, one obtains

$$k_B T_c = 1.13\hbar\omega_D \exp\left(-\frac{1}{\mathscr{N}(0)|g|}\right) \tag{2.37}$$

The second limit is the zero-temperature limit, where the energy gap becomes $\Delta(0)$. In this limit, one obtains

$$\Delta(0) = 1.76 k_B T_c \tag{2.38}$$

In parameter in the exponential in the first limiting case can be identified as electron-phonon coupling parameter $\lambda \equiv \mathscr{N}(0)|g|$. Thus, in achieving high critical temperature, we need high phonon frequency and strong electron-phonon coupling[8].

The value of the critical temperature or the energy gap can also be related to the coherence length and the Fermi velocity. The argument was given by Sir Brian Pippard as followed: since the dispersion relation got modified only in the vicinity of the Fermi surface, only electrons in the width δk form pairs. This width can be estimated to be the ratio of the energy gap to the gradient of the dispersion relation (which is the Fermi velocity), $\delta k \sim \Delta/\hbar v_F$. Using Heisenberg's uncertainty principle, we obtained the estimated size of Cooper's pair, which is basically the coherence length. By doing more careful analysis, the result can be expressed as

$$\xi(T) = \frac{\hbar v_F}{\pi\Delta(T)} \tag{2.39}$$

[8]Metallic hydrogen is a candidate for room temperature superconductor due to the very small mass of hydrogen atom and strong hydrogen bonds- hence very large phonon frequency [11].

At zero temperature, one arrived at the expression (upper critical field in terms of critical temperature)

$$B_{c2} = 1.22\phi_0 \left(\frac{k_B T_c}{\hbar v_F}\right)^2 \tag{2.40}$$

Strong Coupling Limit

When the electron-phonon couple becomes strong, the previous discussions do not hold anymore. One has to generalise the BCS gap equation to be

$$\Delta(\boldsymbol{k}, i\omega_n) = -k_B T \sum_{\boldsymbol{k}'} \sum_{n'=-\infty}^{\infty} V(\boldsymbol{k}-\boldsymbol{k}', i\omega_n - i\omega_{n'}) \Delta(\boldsymbol{k}', i\omega_{n'}) \left|G(\boldsymbol{k}', i\omega_{n'})\right|^2 \tag{2.41}$$

where ω_n is the Matsubara frequency for fermions. The result of the critical temperature in the strong coupling limit is given by the Eliashberg-McMillan theory

$$T_c = \frac{\Theta_D}{1.45} \exp\left(-\frac{1.04(1+\lambda)}{\lambda - \mu^*(1+0.62\lambda)}\right) \tag{2.42}$$

where μ^* is the Coulomb pseudopotential, which is given by

$$\mu^* = \frac{\mu}{1+\mu \ln\left(T_F/\Theta_D\right)} \tag{2.43}$$

The electron-phonon coupling constant, when taking into account the phonon density of state, is also modified to be

$$\lambda = 2\int_0^{\omega_D} d\omega \frac{\alpha^2(\omega) F(\omega)}{\omega} \tag{2.44}$$

where $F(\omega)$ is the phonon density of state and $\alpha(\omega)$ is the electron-phonon matrix element. Effectively, this term can be written as

$$\alpha^2 F(\omega) = \frac{1}{\hbar} \langle \mathscr{N}(0) \left|g_{\boldsymbol{q}}\right|^2 \delta(\omega - \nu_{\boldsymbol{q}}) \rangle_{\mathrm{FS}} \tag{2.45}$$

2.3.3 Unconventional Superconductivity

Although the understanding of superconductivity seems complete with the BCS theory, the discovery of superfluidity in ^{3}He opens up physicists to the possibility of pairing mechanisms

beyond BCS. Such a discovery is unexpected[9] because ^{3}He is a fermion and thus cannot undergo Bose-Einstein condensation. This discovery has led to the idea that ^{3}He atom tends to form pairs as in superconductivity. Since phonon does not exist in liquid, the interaction must be different from the conventional BCS theory. It turns out that the pairing mechanism in ^{3}He comes from magnetic fluctuation, giving rise to p-wave type in the ^{3}He-A phase, which is in contrast to the conventional s-wave pairing by phonon. This discovery has led physicists to speculate if Cooper's pair in metal also arise from other pairing mechanisms.

Unlike ^{3}He atom, electron carries an electric charge and repels each other strongly. One may ask how Cooper's pair formation is stable even with repulsive Coulomb interaction between electrons. The answer to this kind of question may differ between conventional superconductivity and unconventional superconductivity. In conventional superconductivity or BCS theory, electrons in Cooper's pair can avoid getting close to each other by having retarded attractive interaction. Since atoms are much heavier than electrons, the characteristic time scale for the lattice to relax back to its equilibrium position is much larger than the time scale associated with the electron's Fermi velocity. When an electron flies past a region in solid, it distorts lattice for an extended period, which can affect another electron when it passes this area later on. In this way, electrons can effectively attract each other via phonon mediation without getting close to each other, promoting s-wave pairing. This picture is confirmed by measuring the coherence length of Cooper's pair, which turns out to be much larger than the lattice constant. On the other hand, paired-electrons in unconventional superconductors can avoid the overlap by having a non-zero angular momentum in the spatial wave function. In other order parameters (such as p-wave and d-wave), the wave function vanishes when two electrons occupy the same position in space, minimising the overlap and coulomb interaction.

One signature of unconventional superconductivity is the gap structure. In contrast to conventional superconductor where the gap is uniform in every direction, the gap structure in an unconventional superconductor is non-uniform and averaged to zero throughout Fermi surface, that is [84]

$$\int_{\partial \mathscr{M}} \Delta(\mathbf{k}) = \mathbf{0} \tag{2.46}$$

where $\partial \mathscr{M}$ is the boundary of the Fermi surface. The zero-averaged gap structure also indicates that the superconducting transition temperature should be sensitive to the impurity

[9] As in conventional superconductivity, ^{3}He superfluidity gives a Nobel prize twice: one in 1996 for the discovery and one in 2003 for the theoretical work.

scattering. When there is a large amount of impurity in the material, electrons on the Fermi surface scatter each other randomly, making the gap parameter effectively zero and destroying superconductivity completely.

2.4 Mott Transition

In the band structure picture, whether a material behaves as a conductor or an insulator only depends on partially filled bands[10]. If there are any partially filled bands in the system, it is typically a conductor. However, the band structure picture completely neglects the electron-electron Coulomb's interaction. In some cases of half-filled systems where the band structure picture predicts them to be metallic, however, are insulating. This situation is entirely possible due to the strong electron-electron repulsion. When the system is exact half-filled, each lattice site is filled by exactly one electron, and they cannot move to the neighbouring sites. This causes the insulating behaviour, which is called the 'Mott insulator'[11].

This type of insulator also prefers to have antiferromagnetic order. To understand why, we can follow the qualitative argument here. If the interaction energy between electrons is very large but not infinite, the total energy of the system can be lowered by allowing an electron to hop to neighbouring sites (this is due to the Heisenberg uncertainty - if a particle is allowed to occupy larger space, it will have smaller energy). In order to do so, electrons in the nearest neighbour sites must have spins in the opposite direction to each other (otherwise, it is forbidden to hop around by Pauli's exclusion principle). The process of this hopping comes from the second-order perturbation theory[12]. This particular virtual process is called the superexchange.

To understand this in more detail, we look at the mean-field Hamiltonian, called the Hubbard Hamiltonian

$$H = -t \sum_{\langle ij \rangle} a^{\dagger}_{i\sigma} a_{i\sigma} + U \sum_{i} n_{i\uparrow} n_{i\downarrow} \tag{2.47}$$

Applying degenerate second-order perturbation and using the identity on Pauli's matrices

$$\sum_{i} \sigma^{i}_{\alpha\beta} \sigma^{i}_{\gamma\delta} = 2\delta_{\alpha\delta}\delta_{\beta\gamma} - \delta_{\alpha\beta}\delta_{\gamma\delta} \tag{2.48}$$

[10] An insulator that arises from the completely filled band is called the 'band insulator'

[11] There is also another type of insulator, which arises from the Anderson localisation. Sir Nevil Mott and Philip Anderson worked in Cavendish Laboratory and shared Nobel prize in the same year!

[12] So this hopping is actually a virtual process.

one arrived at the correction [5]

$$H' = \frac{4t^2}{U}\left(\boldsymbol{S}_1 \cdot \boldsymbol{S}_2 - \frac{1}{4}\right) \tag{2.49}$$

which suggests the Mott insulator to be the Heisenberg antiferromagnetic[13].

The fact that a strongly interacting half-filled system becomes insulating, as well as antiferromagnetic, has a deep connection to the nesting effect. The most intuitive way to understand this is as following: when a system undergoes antiferromagnetic transition, the 'magnetic' unit cell is doubled, shrinking Brillouin's zone by half and the introducing energy gap. Hence, the system becomes an insulator. However, we cannot tell how strong the interaction needs to be to have a magnetic ordering. To calculate the critical interaction strength, we need to look at Lindhard's function, defined by [54]

$$\chi^{(0)}(\boldsymbol{q}) = \sum_{\boldsymbol{p}} \frac{f_{\boldsymbol{p}} - f_{\boldsymbol{p}+\boldsymbol{q}}}{\varepsilon_{\boldsymbol{p}+\boldsymbol{q}} - \varepsilon_{\boldsymbol{p}}} \tag{2.50}$$

The susceptibility, calculated from the second-order perturbation theory (RPA approximation yields the same result), reads [54]

$$\chi(\boldsymbol{q}) = (g\mu_B)^2 \frac{\chi^{(0)}(\boldsymbol{q})}{1 - U\chi^{(0)}(\boldsymbol{q})} \tag{2.51}$$

Therefore, magnetic instability tends to happen at the wavevector of the peak in Lindhard's function.

2.5 Aubry's Transition

In this section, we discuss the role of interaction and the Aubry's transition. We postpone the discussion of sliding mode to chapter 4 on Sb-II. The general role of interactions between host and guest chains in an incommensurate system is to modulate the position of atoms in the chain. To understand the effect of interactions intuitively, we can simplify the system to have only one kind of chain in a perfect periodic potential, which comes from sub-lattice. The situation is shown in figure 2.7a. If the chain has finite rigidity, it is clear that there is a force acting on each atom, modulating the chain's atomic position. When the interaction

[13] Although it is relatively easy to solve the exact half-filled system, the case of away from half-filled' is extremely complicated. A strong interacting system close to half-filled with small amount of holes can be describe by effective t-J Hamiltonian [134].

is stronger, there is a higher tendency for atoms to reach minima of the potential, shown in figure 2.7b. In the extreme limit of very strong potential, we can see pictorially that all atoms will sit at the bottom of potential minima as in figure 2.7c. Since the number of atoms in the host and guest chain is not equal, defects of missing atoms are introduced (a small empty circle in figure 2.7c). This transition between the incommensurate phase and commensurate phase with defects is known as Aubry's transition. A rigorous analysis of this kind of system was done in the literature [13].

(a) Weak interaction between host and guest chains

(b) Intermediate interaction between host and guest chains

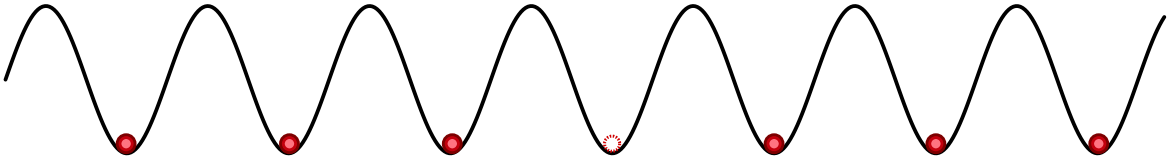

(c) Strong interaction between host and guest chains

Fig. 2.7 Figures showing Aubry's transition between incommensurate phase and commensurate phase with defects.

Chapter 3

Experimental Techniques

3.1 Pressure Cell Technique

3.1.1 Introduction

As pressure is one of the most important tuning parameters in condensed matter systems, there has been much development in techniques to achieve higher and higher pressure. The fact that we require such high pressure in our field of research (at least ten thousand bars up to a few hundred thousand bars) makes this work very difficult. There are a few types of pressure cells available to use. The suitability of the pressure cell depends on the nature of the projects. For relatively low pressure, one might consider setting up a piston-cylinder cell (PCC, or another name - 'clamp cell') [150]. For the PCC cell, one can reliably set it up for the pressure range up to 25-30 kbar. It is relatively easy to set up compared to other types of pressure cell due to the very large sample space (with the dimension of approximately 4mm × 4mm × 3cm). This means that we can use very large samples for the measurement, up to a millimetre. Apart from that, we also have advantages of using this PCC over other types of pressure cells: (i) multiple samples (up to five samples and one tin manometer) can be measured in the cell simultaneously. (ii) excellent hydrostaticity condition due to large sample space. However, to go higher than 30 kbar, one needs to consider using other types of pressure cells. There are two options - Bridgman anvil cell [25] and (Moissanite/Diamond) anvil cell. The Bridgman anvil cell can be pressurised up to above 100 kbar, and the sample space is large (2 mm). However, the nature of the gasket is porous (it is made of pyrophyllite) - it requires a pressure medium to be solid powder, in which Steatite is commonly used. By using a solid powder pressure medium, we trade off a homogeneity in the sample space. Thus, Bridgman anvil cell is suitable for only certain studies (such as to observe the existence

of superconductivity) but not so for wide range of studies such as to observe some subtle transition (ferromagnetism, antiferromagnetism, etc), tracking phase transition temperature as a function of pressure (as the transition would be generally very broad due to pressure inhomogeneity), or power law studies. Finally, we move to the moissanite anvil cell (MAC) and diamond anvil cell (DAC). We only used these MAC/DAC cells for our entire work in this dissertation. Hence, we will dedicate this section of pressure technique to describe the MAC/DAC.

3.1.2 Moissanite Anvil Cell and Diamond Anvil Cell

In the MAC cell (and DAC cell - they work the same way, only diamond is much harder than moissanite and much more expensive), it is one of the best kinds of cell that both give an excellent hydrostaticity and can go up to very high pressure. Depending on the size of the culet, DAC cells can potentially go up to many hundreds of kilobars or megabars. Moreover, we only use liquid medium to transmit pressure in this cell. That is why we expect a decent hydrostaticity in the MAC and DAC cells. The only trade-off of this anvil cell is that it is extremely difficult to set up. The working space in this cell is generally no more than 0.4mm in diameter and 0.1mm in thickness - everything has to be crammed into this space (a sample with four wires, a micro-coil, a ruby, and a pressure medium). The sample size is hence no larger than 200 microns in length and 40 microns in thickness. We will now describe each component in detail.

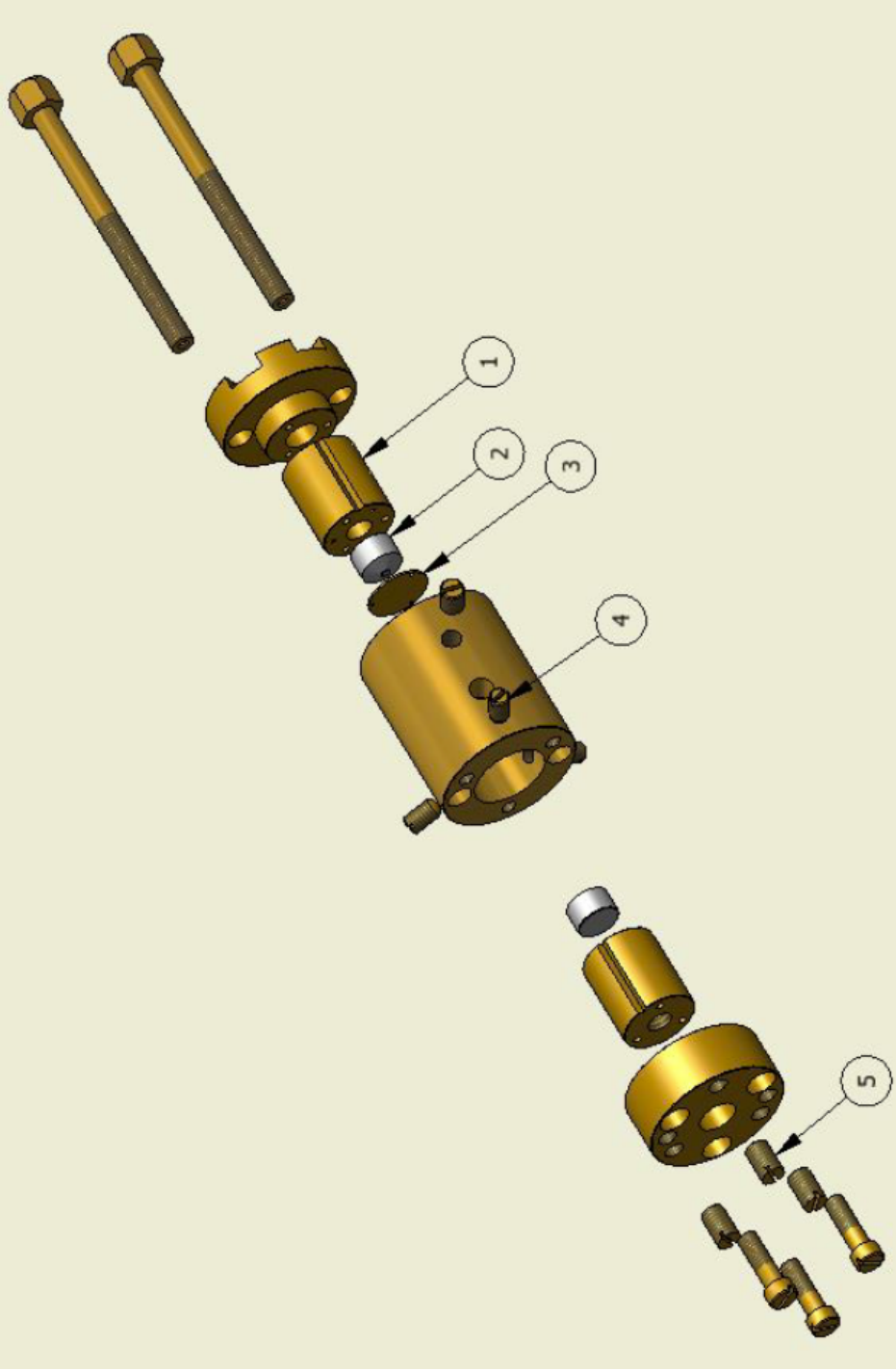

Fig. 3.1 The diagram showing components in pressure cell. The labels are: (1) piston - this is used to hold the anvil (2) anvil (3) gasket - for making the sample space and getting squashed by two anvils (4) guiding screw (5) tilting screws. The figure is taken from [32]

Material for the body

In one pressure cell, we can use it for many kinds of experiments, resistivity, AC susceptibility and TDO technique, by preparing the gasket in different ways. Therefore, we have to choose a material for the body that allows us to use it for all measurements mentioned above. A good candidate for this is the beryllium copper (BeCu), as it provides good strength and gives a low magnetic background.

Anvil

We mainly use two different types of anvil, moissanite and diamond, depending on the pressure range we aim for. For the pressure range of less than 120 kbar, moissanite works perfectly fine. Above this pressure, one needs to go for a diamond. Then, we need to polish the flat surface of the anvils to the desired diameter. To choose the culet size, in the case of moissanite, we follow the table (quoted from the manual made by Dr Patricia Alireza).

Culet Size (mm)	Estimated Maximum Pressure (kbar)
1.2	40
1.0	70
0.8	120

Table 3.1 Table shows the estimated maximum pressure that a pressure cell with different culet size is expected to reach.

And in the case of a diamond, the estimated maximum pressure follows a rule of thumb.

$$P_{\max} = \frac{125}{\big(d(\mathrm{mm})\big)^2} \quad \text{kbar} \tag{3.1}$$

where d is diameter of the culet in millimetre.

Finally, the most crucial step in preparing anvils is to align both anvils in such a way that they align in the x-y direction and parallel to each other. To see if they align in the x-y direction, we look at the silhouette as we shine light into a hole on the side of the pressure cell. To check if two anvils are parallel, we look at the interference pattern that arises between them. The pattern will be like Newton's rings if the surfaces are parallel to each other.

Gasket

A gasket is undoubtedly the most crucial element in the anvil cell. There are two types of gasket - metallic gasket and insulating gasket. There are equally advantages and disadvantages for both types of the gasket. For a metallic gasket, the advantage is that it is stable, but the disadvantage is that the wires/leads or sample in the cell can short to the gasket, which will make the cell unusable and needs to be reset. For an insulating gasket, the advantage is that it is really unlikely to have a short to any part of the cell, but the disadvantage is that it is not stable - the gasket can crumble and collapse very easily. Moreover, the pressure inside the insulating gasket is always prone to relax (sometimes even by a factor of two).

To set up a metallic gasket, we start with choosing the suitable material for this. There are primarily three candidates - beryllium copper (BeCu), stainless steel 316, and alloy MP35 (nickel-cobalt base). The material we use highly depends on the type of measurement and target pressure. For AC susceptibility or tunnel diode oscillator (TDO) measurement, BeCu is the only option as it gives the smallest magnetic background amongst the three of them. Stainless steel and MP35 are highly magnetic and hence give too large background and are not suitable for any magnetic property measurement. For transport measurement (resistivity), the option is more open. BeCu is the standard material for relatively low pressure (up to 100 kbar) because it is easy to work with (as it is soft but needs to be heat-treated later). However, one can also use stainless steel with moissanite to improve the stability of the gasket with the trade-off that it is harder to work with. For diamond, we have to go for MP35 as it is the most rigid material amongst the three to stand the tremendous force we use with diamond.

A table below shows the yield strength of each material

Material	Yield Strength (GPa)
BeCu half-hardened	0.59
BeCu half-hardened and ageging at 370 C for 10 minutes	1.2
Stainless Steel 316	1.5
MP35	2.2

Table 3.2 Mechanical yield strength of a few candidate materials to be used for gasket.

Then, the gasket needs to be pre-indented - to make the part at the centre become very thin. Since the physics of the gasket is rather complicated (very non-linear, and one has to take into account deformations), the pressure is not simply $P = F/A$ but depends highly on the gasket's thickness. The theory of gasket is provided in the Dunstan 1989 article

[50]. It is generally known that the thinner the gasket, the higher the pressure it can reach. For resistivity measurement, the gasket has to be pre-indented down below 100 microns. However, the AC susceptibility measurement needs a thicker gasket to obtain more turns of a micro-coil we put inside the pressure region. The usual thickness for both AC susceptibility and TDO cells is 140 microns. The next step is to make a hole at the centre of the gasket. As a rule of thumb, the hole should not be larger than half the size of the culet. For instance, with a 0.8 mm culet, the maximum size of the hole should be 0.4 mm. The smaller the hole, the better the stability of the gasket. The final step for the gasket preparation is to insulate it. There are many ways of doing insulation, and it also depends on what type of measurement one needs to do. For resistivity, one usually carves two beds and fills them with insulation (which is made of Stycast 1266 mixed with alumina oxide power). For the AC susceptibility, one makes two narrow channels using a scalpel and fills them with the insulation.

There are fewer steps to do to set up an insulating gasket, but it is only suitable for resistivity measurement (since one cannot make channels on it). Instead of just drilling half of the size of the culet, we remove the whole flat area. Then fill the hole with the prepared cubic boron nitride powder (the way to prepare this powder is to mix cubic boron nitrite with Stycast 1266 in the ratio 12:1 and grind it very well) and press it very hard. Finally, this will give us an insulating gasket. One has to drill a hole of less than half the size of a culet, and the gasket is ready.

Pressure Medium

The next step is to choose what pressure medium to use. There are, again, many options one can choose, depending on how much hydrostaticity one would like to acquire. We can classify pressure medium in four groups as follows: (i) solid pressure medium (ii) 'oil' type (iii) organic fluid (iv) condensed gas. The solid pressure medium, such as NaCl, is the easiest one to load because there is no risk of leaking, and it does not compress (that means there will be no movement inside the gasket - then the low risk of wires getting destroyed). However, they give the worst homogeneity amongst the four groups. Oil type pressure mediums, such as Glycerol and Daphne Oil 7474, on the other hand, give much better homogeneity than the solid medium but are a little bit harder to make it work because of the possibility of leaking and more compressibility. Organic fluids, such as 4:1 methanol-ethanol and 1:1 pentane-isopentane, is much more challenging than the two former groups for a few reasons: (1) high volatility (2) aggressiveness toward epoxy and insulation (3) high risk of leaking and high compressibility. To use organic fluid, we must submerge the whole pressure cell in the

liquid when we close it due to high volatility (it evaporates too fast). The homogeneity from the organic fluid is also much better than both solid pressure medium and oil type. Finally, the condensed gases, such as argon and nitrogen, are the best pressure medium in terms of homogeneity. It is neither easier nor harder to load compare to organic fluids. The easy aspect of the condensed gases is that they are usually very inert - hence they do not damage epoxy and insulation. The problematic aspect is that it is very compressible - once pressure is applied, the hole inside may close and destroy wires/leads.

The table below shows the hydrostaticity limit of each medium. The data was acquired from [143].

Type	Pressure Medium	Estimated Hydrostatic Limit (kbar)
Solid	NaCl	15
Oil	Glycerine	50
	Silicon Oil	35
	Daphne 7373	40
	Daphne 7474	60
Organic	1:1 n-pentane and isopentane	85
	4:1 methanol and ethanol	90
	Petroleum Ether	95
Condensed Gas	Nitrogen	>100
	Argon	>100
	Helium	>100

Table 3.3 Hydrostatic limit of some pressure media. The data was acquired from [143].

Ruby Fluorescence

The pressure inside a sample space is usually measured using a tin manometer in a piston-cylinder or Bridgman cell. Tin undergoes superconductivity at 3.72 K at ambient pressure, and this transition changes under pressure. Therefore, pressure is measured by measuring superconducting transition temperature. This can be done efficiently and accurately in the pressure cells mentioned above since they have large chamber spaces. On the other hand, the space inside the MAC/DAC is very limited, and another way of measuring pressure must be employed.

In the case of the anvil cell, we gauge pressure inside the cell using Ruby Fluorescence. Ruby is made of $\alpha - Al_2O_3$ with some impurity of Cr^{3+} in it. There is some good literature on the physics of optical properties of ruby in high pressure [139]. We shall not go into much detail here. To summarise things briefly, we quoted a figure of the energy spectrum of Cr^{3+} in ruby from the paper [139]. There is a strong crystal field in the environment of Cr^{3+} atoms. Hence, we expect series of crystal field splitting in the energy spectrum. Figure 3.2 includes the effect of crystal field, electron-electron coupling and spin-orbit coupling. Some of the energy levels are broadened into energy bands. In this case, they are the U, Y, and X bands, which absorb green and blue light (that is why ruby is pinkish or reddish). In our experiment, we use a green laser to excite electrons to the U band. Subsequently, they relaxed to the ground state via the process ${}^4T_2 \rightarrow {}^2E \rightarrow {}^4A_2$. The energy differences between ${}^2E$ states and ${}^4A_2$ give visible light in the red spectrum - we called them R_1 and R_2 lines. The spectrum of these two lines shifts upward in high pressure. Therefore, we can gauge pressure by a mean of measuring the shift in photon frequency. Since the R_1 line gives a stronger and sharper signal than the R_2 line, we use it as a reference.

At relatively low pressure, the relationship between pressure and wavelength at room temperature (293 K) very well follows the equation [139]

$$P = (18700 \pm 300) \ln\left(\lambda/\lambda_0\right) \text{ kbar} \tag{3.2}$$

where λ_0 is the wavelength of R_1 line at ambient pressure, which is 694.30 nm in our case.

Since we measure pressure by ruby fluorescence only at room temperature, it is only natural to ask how reliable it is at low temperature (which is the temperature we usually are interested in). One may expect pressure to drop once the system is cooldown to cryogenic temperature. However, measurements using tin and lead show that the drop in pressure from room temperature to low temperature is usually less than two kbar. Thus measuring pressure by mean of ruby fluorescence at room temperature is quite reliable.

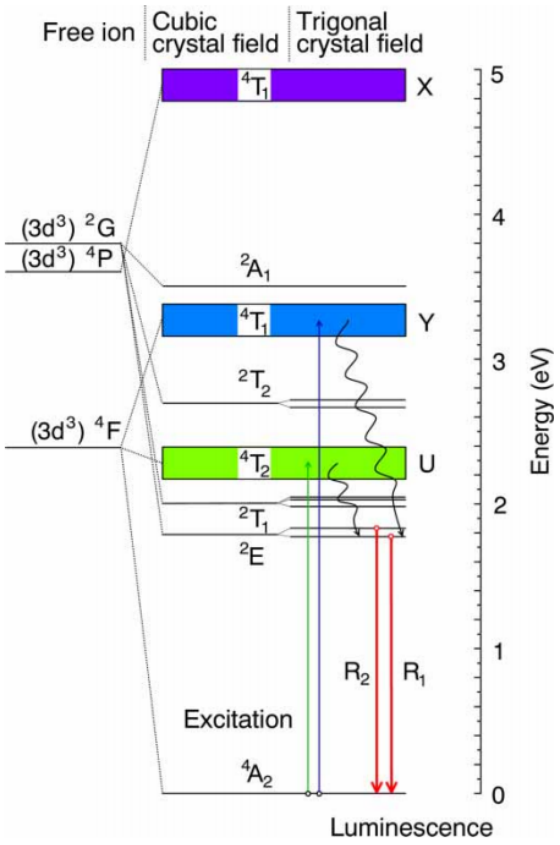

Fig. 3.2 Energy spectrum of Cr^{3+} in ruby in the presence of crystal field. This figure is taken from [139].

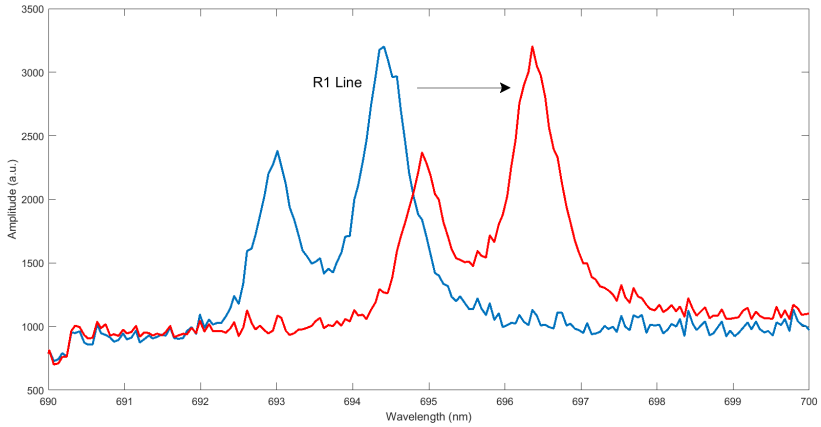

Fig. 3.3 The ruby spectrum from a pressure cell. A green laser is used to illuminate the ruby. The blue curve is at ambient pressure and the red curve is at 58 kbar.

3.2 Measurement Systems

3.2.1 Physical Property Measurement System (PPMS)

PPMS is a cryostat made by Quantum Design company (QD). It is a convenient and versatile measurement system. There are many different kinds of measurements in this system - resistivity, AC susceptibility and heat capacity, to name three. The temperature range that PPMS can go without helium-3 probe is between 2 K and 400 K. The cooling system uses liquid nitrogen to cool down to 77 K and followed by liquid helium-4 to cool down to 4.2 K. To cool the system further to the base temperature, which is 2 K, it needs to pump out helium gas to go to significantly lower pressure. By doing so, it lowers the boiling point of helium. As there is a limited amount of helium one can pump out, we have to keep feeding helium into a pot. It is just an optimisation problem of how much helium should be fed into the system per unit time. If it is too fast, it will not be able to go down much below 4.2 K, but if it is too slow, it can stay at the base temperature for only a short amount of time (until helium is empty). The work of controlling the flow rate when the system initially cool down is done automatically - called the 'pot operation'. There are basically two impedance tubes - the large one and the small one (capillary). When the system starts cooling down below 10 K, the large impedance tube is fully open to fill the pot. Once it reaches 4.2K, this tube is completely closed by heating up the gas inside to make a bubble that blocks the flow (this is the subject mathematicians have been working a lot on - slow viscous flows). Finally, as the capillary tube is always open, the flow rate is the optimised value that balances the evaporation rate of helium to the pump. Ideally, if there is no blockage, the system should be able to stay at the base temperature as long as one desires.

The strongest point of PPMS is the ability to do very fine temperature control. It can do a temperature sweep with the rate between 10 mK/min to 20 K/min. The ability to cool down and warm up with such a slow rate as 10 mK/min is crucial to study phase transition in many systems (such as a shoulder in resistivity that arises from ferromagnetic transition or a kink in resistivity that arises from antiferromagnetic transition). Moreover, the ability to have a very reliable PID controller is very crucial to study the system in fine detail (such as power-law study, or fitting data to known equations).

Finally, the PPMS we are using is also capable of producing a magnetic field of up to 9 T. The field is produced by a superconducting magnet, which is submerged in liquid helium-4. The superconducting magnet is a solenoid made by superconducting wire (usually made of filaments of niobium-titanium or niobium-tin embedded in copper). Because of a persistent

current in a superconductor, we can produce a constant magnetic field without needing much energy consumption and cooling power. A superconducting heat switch in the magnet is used to change the current in a superconducting magnet.

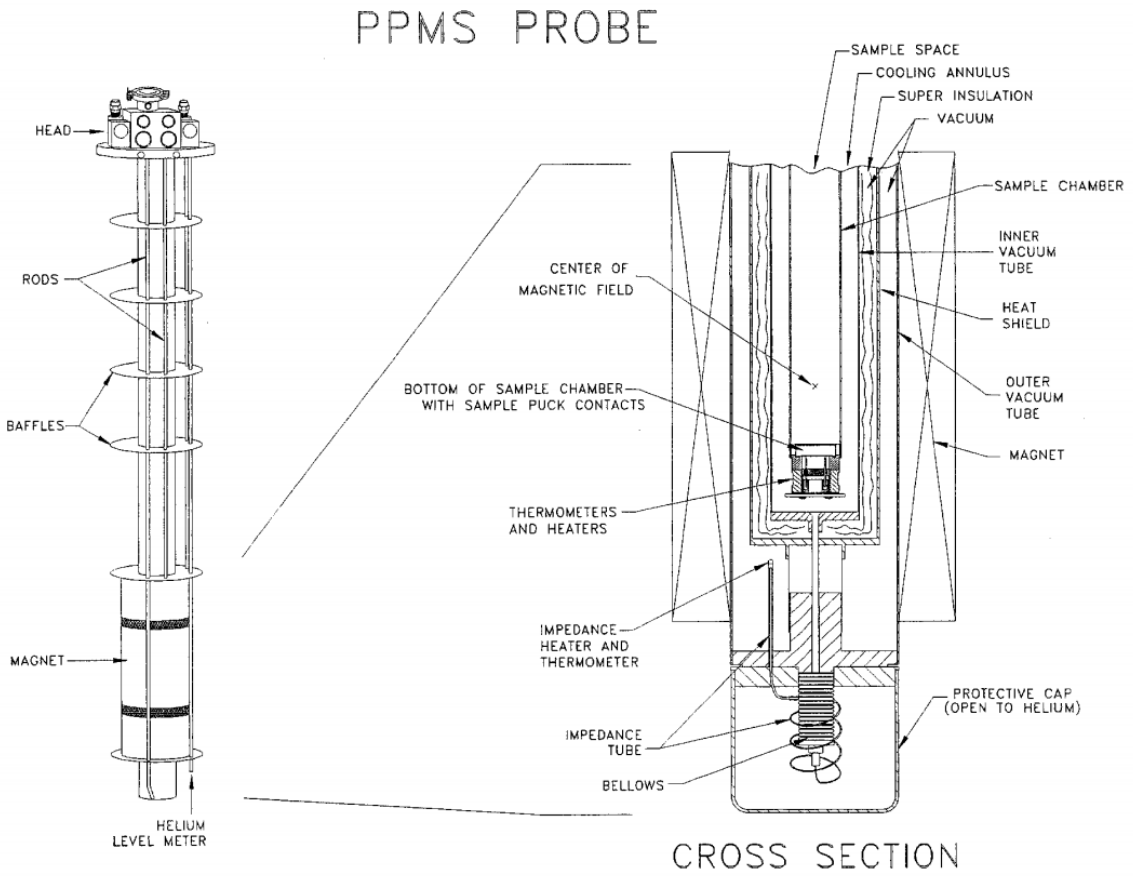

Fig. 3.4 The diagram showing PPMS probe and its cross section. The figure was taken from [48].

3.2.2 SQUID Magnetometry

The measurements of magnetisation (or SC susceptibility) in this work have been carried out in the commercial Quantum Design Magnetic Property Measurement System (MPMS), which is based on a DC SQUID magnetometry (Superconducting Quantum Interference Device). The DC SQUID is made of a superconducting loop with two Josephson's junctions and is really sensitive to the magnetic field passing through the loop. The sensitivity of this MPMS is as good as 10^{-9} emu or 10^{-12} A $\cdot$ m^2 (this number tells us how small a magnetic dipole

this device can detect). The SQUID is composed of two Josephson junctions connecting together to form a ring.

A Josephson junction is composed of a normal metal sandwiched between two superconductors. By doing so, there are many interesting phenomena. We start by noting that, even if a thin layer of normal metal is inserted at the middle, a supercurrent still exists. This is because of the tunnelling of Cooper pairs across the junction. However, the current can flow in the absence of voltage across the junction only if it is smaller than the 'Josephson critical current' - I_J (This value is different from the critical current I_c in superconductor and depends on properties of the junction). The current across the junction can be written by

$$I = I_J \cos(\Theta) \tag{3.3}$$

where Θ is the phase difference between Cooper pair's wavefunction in those two superconductors (to the left and to the right of the junction). Once the current exceeds this critical current, normal electrons (non-superconducting) will contribute to the total current. Hence, a voltage is developed across the junction as $I > I_J$ (and SQUID is now operating in a 'resistive mode').

In SQUID ring, the total current is the sum of the contribution from each junction

$$I = I_{J1} \cos(\Theta_1) + I_{J2} \cos(\Theta_2) \tag{3.4}$$

with $I_{J1} = I_{J2}$ and $\Theta_1 = \Theta_2$. Once we apply an external magnetic field, these conditions do not hold anymore. Firstly, currents in each junction are not equal, so the flux quantisation requirement is satisfied. Secondly, phases across each junction also change. By using the fact that flux passing through the ring is equal to the line integral of vector potential along the circumference, and $\mathbf{A} = (\hbar/2e)\nabla\theta$, one can calculate the critical current of the whole system to be

$$I_{C-SQUID} = I_{C-Jospehson} \cos\left(\frac{\pi\Phi}{\Phi_0}\right) \tag{3.5}$$

where $\Phi_0 = h/2e$. Therefore, once SQUID works in the resistive mode, the measured voltage will be a periodic function of Φ_0. That way, we can measure the magnetic field's change very accurately by counting the number of periods.

In real SQUID magnetometry, it is impractical to count the number of the period since the frequency is too large. It is operated by using a flux transformer that transfers the flux from a sample to SQUID. Then, the SQUID (which has a bias current $I_b > I_{C-SQUID}$) is

connected to the feedback coil, which produces a magnetic field into the SQUID loop and keeps the voltage across it constant. Then the signal one gets come from this feedback coil. The sample is sandwiched between two pickup coils for the input, and the sample position can be varied. If we can measure the magnetic field accurately at a different sample position, the sample's magnetisation can be calculated by modelling it to be a perfect dipole.

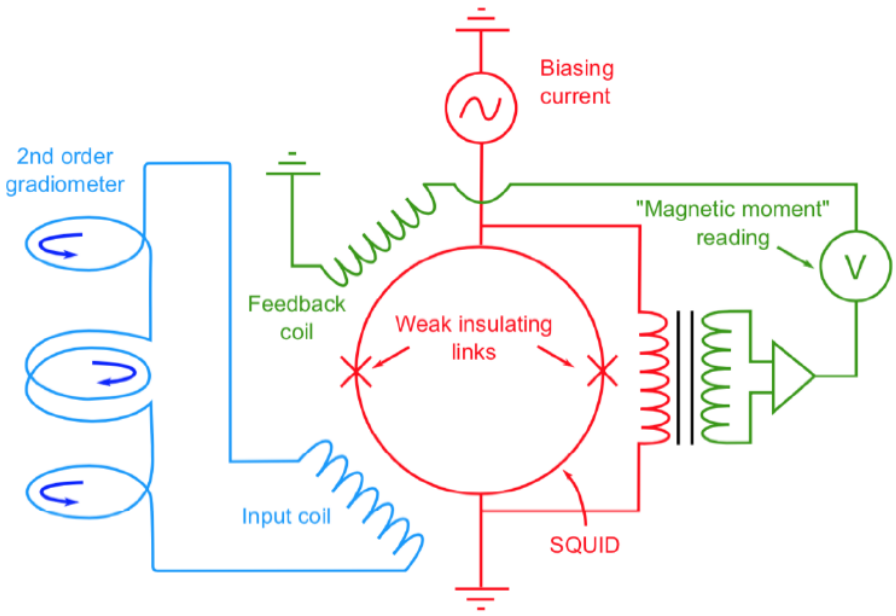

Fig. 3.5 The schematic diagram for a SQUID circuit. Figure credit: [34].

Chapter 4

Incommensurate Host-Guest Antimony, and Possible Aubry's Transition

We dedicate this chapter to the study of high-pressure antimony. This work was inspired by the previous studies of bismuth, especially the high-pressure one in Cavendish Laboratory [29]. Antimony has many similarities to bismuth. Firstly, they are both semi-metals at ambient pressure and undergo phase transitions to an incommensurate phase at high pressure. Both of them show superconducting transition at low temperatures in this incommensurate phase. High-pressure bismuth is already quite well studied compared to high-pressure antimony since it requires significantly lower pressure to access those high-pressure phases. For instance, it requires 28 kbar to enter the Bi-III (incommensurate) but 86 kbar to enter Sb-II (incommensurate).

For the sake of completeness, we will include the high-pressure study in Sb-I, although it does not have an incommensurate host-guest structure (and hence not the main focus of our research).

This project results from collaborations between Puthipong Worasaran, Stephen Hodgson (3rd year PhD student at the time of preparing this dissertation), Dr Patricia Alireza, and Dr Jiasheng Chen. The resistivity pressure cells setup was done by PW and were measured in PPMS by SH. The SQUID pressure cell setup was done by PLA (and she helped with most

of the measurements in the MPMS system). JC measured the upper critical field carefully in the DMS.

4.1 Sb-I

4.1.1 Introduction and Literature Review

Antimony is an element in the pnictogen group with the valence electron configuration $5s^2\ 5p^3$. In contrast to bismuth, which is soft, antimony is somewhat brittle. The crystal structure of antimony is the rhombohedral A7, similar to both arsenic and bismuth. The rhombohedral A7 can be thought of as the distorted version of a primitive simple cubic structure. Since the distortion doubles the unit cell, it opens a gap at the Fermi energy and lowers the electronic energy. Hence, the distortion in antimony is like a Peierls transition [95], doubling the total number of atoms per unit cell (from half-filled band to filled band) and accounting for the poor metallic behaviour. Crystallographically, the rhombohedral structure with an angle of $\alpha = 60^\circ$ is isomorphic to a simple cubic. When the distortion comes in, it produces two effects. Firstly, the angle α is reduced slightly below 60 degrees. Secondly, the sublattice (atom at the middle of the unit cell) gets displaced slightly toward point $(0,0,0)$. The distorted angle α ranges from 54.11° to 57.23° in bismuth, antimony, and arsenic [8].

The Peierls distortion in antimony decreases when external pressure is applied [70]. As a result, the crystal structure tends to go toward cubic at high pressure, with many debates about whether it ever reaches a complete simple cubic structure [70, 149]. Later on, it was found that there is an intermediate phase at a pressure between 70-85 kbar, which is not a simple cubic phase but a monoclinic incommensurate phase Sb-IV [45]. Antimony undergoes another structural transition to a tetragonal incommensurate phase Sb-II above 86 kbar [127]. We will not discuss these incommensurate phases in this section but will be thoroughly investigated later in this chapter. The crucial point here is that the antimony structure tends to revert back to simple cubic under pressure but never reaches it.

A similar change in the crystal structure under pressure also happens in bismuth and arsenic. It is of great interest to briefly overview both bismuth and antimony (we do not discuss arsenic as there are only a few studies available). Bismuth is a compensated semimetallic at ambient pressure with extremely tiny Fermi surfaces. The carrier density is as tiny as one per ten thousand atoms, giving rise to a very light electron effective band mass due to a high curvature at band minimum. The effective mass in bismuth is as small as 0.001 of the bare electron mass [28], giving bismuth to host various intriguing phenomena. For

example, it is straightforward to measure the quantum oscillatory effect in bismuth due to the small effective mass, making it the first to observe quantum oscillation [114]. Another example is an exotic fractionalisation in the quantum limit of bismuth (which can be achieved even in a moderate field due to a small Fermi surface) [18]. The Fermi surface of bismuth is shown in figure 4.1a. Under hydrostatic pressure, the electron band is pushed up, while the hole band is pushed down, resulting in becoming more insulating [28]. The mechanism behind this is still unclear [27]. One evidence of the reduction in the band-overlap was clearly seen in the resistivity measurement, which shows a low-temperature upturn at a pressure above $\sim$ 17 kbar [15]. Hall measurement and quantum oscillation measurement also agree with this interpretation well [23, 69, 68, 71]. At the pressure between 25-28 kbar, bismuth undergoes a structural phase transition from Bi-I to Bi-II [27]. This structural transition masks the Lifshitz transition[1], which is supposed to happen in this vicinity (by extrapolating from the quantum oscillation measurement), making the physics unclear if the insulating nature arises because the Fermi surface shrinks to zero continuously or if it is because of the change in the crystal structure.

Surprisingly, the effect of pressure on antimony is completely opposite to bismuth and arsenic, despite having isostructure and isoelectronic to both of them. Under pressure, antimony becomes more metallic [93]. The metalisation in antimony is caused by the enlargement of the Fermi surface, which was comfirmed by the quantum oscillation measurement up to 14 kbar in [96]. To this date, it is still unclear why antimony behaves so differently from bismuth. Quantum oscillation in antimony is more difficult to observe than in bismuth due to the larger Fermi surface and heavier effective mass. Figure 4.1b shows the antimony Fermi surfaces, consisting of three electron pockets and six distorted elliptical hole pockets, which translate into each other by a 120° rotation. In this literature, only one frequency was observed, which turns out to be the one from the holes. Since antimony has small Fermi pockets as in bismuth, it is expected to show very strong and non-saturated magnetoresistance [44, 53].

[1] Lifshitz transition is a continuous transition between two topologically distinct Fermi surface state.

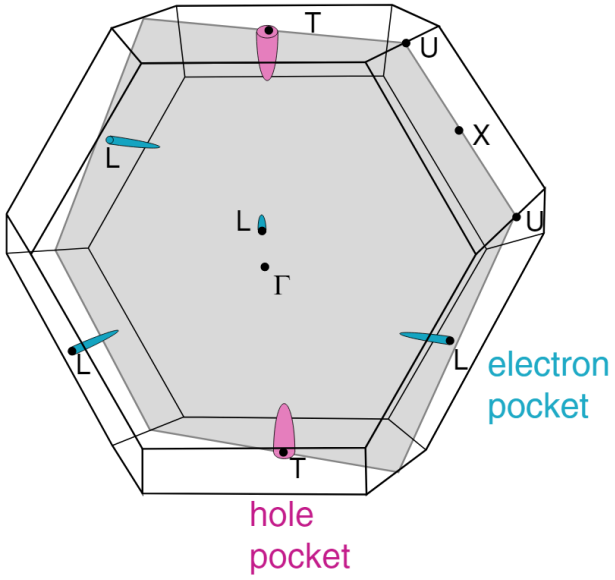

(a) Fermi surface of bismuth. The figure is from [66].

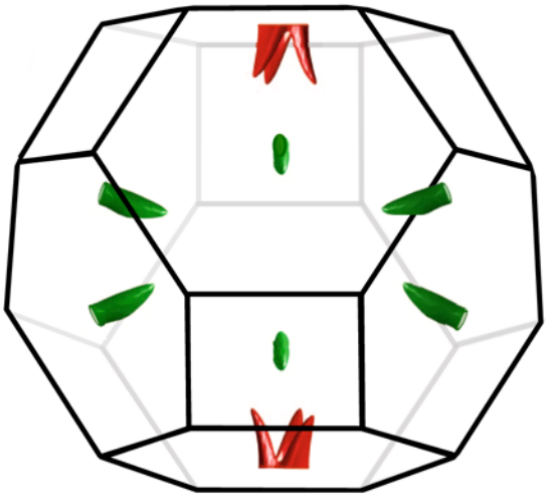

(b) Fermi surface of antimony. The figure is from [72].

Fig. 4.1 Fermi sufaces of bismuth and antimony

4.1.2 Results and Discussions

Resistivity Measurement in Sb-I

We performed resistivity measurement in Sb-I using the standard 4-terminal technique. The contacts geometry is such that all of them are connected to the sample's corners. The medium used to transmit pressure is a 4:1 mixture between methanol and ethanol, which gives an excellent hydrostatic condition. Due to the high failure rate in the anvil cell, we had to set up seven different pressure cells dedicated to the study of Sb-I only. The range of pressure we measured in Sb-I is between 7 kbar and 62 kbar. Since the contact geometry is not simply a straight line, it is not easy to obtain the electrical resistivity from the geometrical factors. We adopt a different way of getting the resistivity values by comparing them with the resistivity at ambient pressure, known in the literature to be $41.7\mu\Omega\cdot$cm(however, we do not have the ambient pressure data for the one at 46 kbar and 62 kbar - we extrapolate the resistivity of 46 kbar from the lower pressure data and use the same geometrical factor here for 62 kbar since it is the same sample). The measurement was performed using the AC transport option in the PPMS with 2 mA excitation current and 23 Hz excitation frequency.

Figure 4.2 shows the resistivity of Sb at different pressure. The RRR of Sb in every sample is above 100, indicating good quality samples. The resistivity as a function of pressure agrees well with the literature where the sample becomes more metalised. On studying low-temperature power-law behaviour (figure 4.3), resistivity follows the power-law $\rho = \rho_0 + AT^2$ between 0 K to 10 K in the whole range of pressure we have, suggesting the Fermi liquid behaviour in the entire Sb-I phase.

The A-coefficient in $\rho = \rho_0 + AT^2$ decreases from $\sim 7.8\times10^{-4}\mu\Omega\cdot\text{cm}\cdot K^{-2}$ at ambient pressure to $\sim 1.6\times10^{-4}\mu\Omega\cdot\text{cm}\cdot K^{-2}$ at 62 kbar. According to the Kadowaki-Woods relation $A/\gamma^2 \sim$ constant, where $\gamma \propto m^* \propto \varepsilon_F^{-1}$ is the linear coefficient of the specific heat at zero temperature, one can infer that the A-coefficient is inversely proportional to the square of the Fermi energy, i.e. $A \sim \varepsilon_F^{-2}$. Comparing this to the experimental result, we can obtain the Fermi surface's dimension indirectly. It turns out that the Fermi surface is enlarged by more than a factor of two from ambient pressure to 62 kbar.

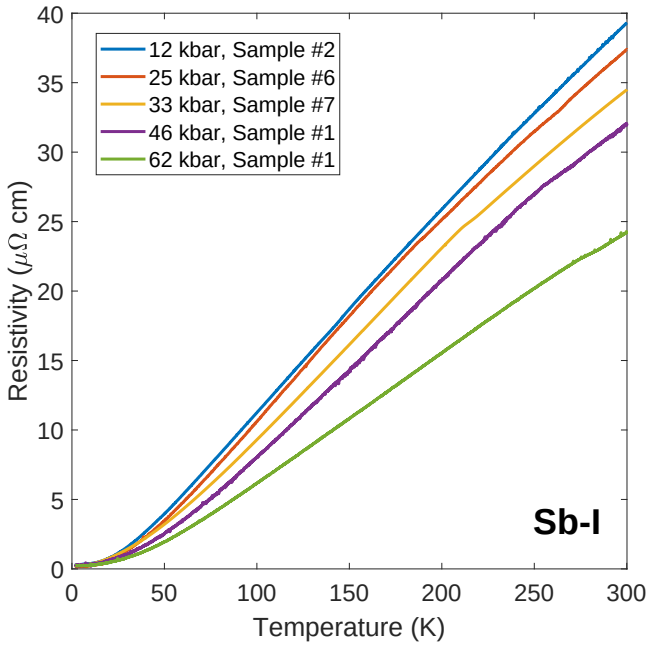

Fig. 4.2 The resistivity profile of Sb-I at different pressures.

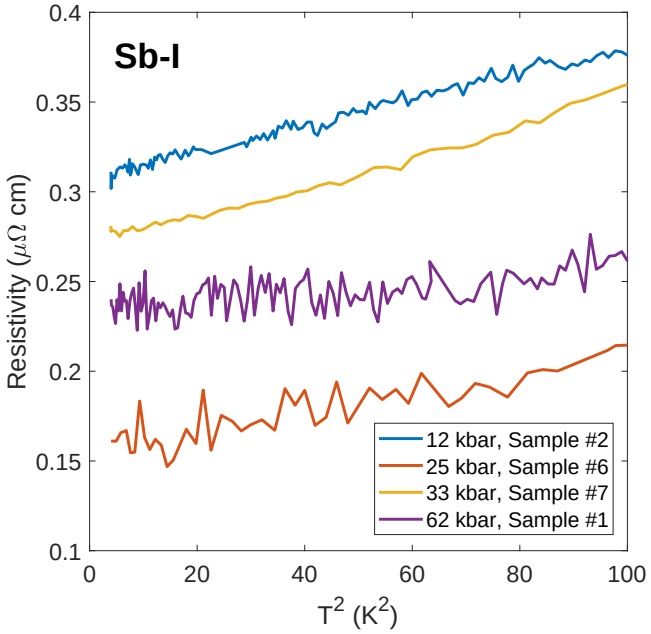

Fig. 4.3 Low temperature resistivity of Sb-I, plotting against T^2.

Magnetoresistance in Sb-I

In this section, we present the magnetoresistivity up to 9 T in high-pressure Sb-I (figure 4.4). Remarkably, Sb-I shows an extremely large non-saturated magnetoresistance, over 3000 times at 9 T at ambient pressure, and gets suppressed significantly at high pressure. The two-band model can be used to explain the non-saturated nature of magnetoresistance in a compensated semi-metal. The resistance as a function of field, calculated from the two-band model, reads [113, 167],

$$\rho_{xx}(B) = \frac{1}{e}\frac{(n_e\mu_e + n_h\mu_h) + (n_e\mu_h + n_h\mu_e)\mu_e\mu_h B^2}{(n_e\mu_e + n_h\mu_h)^2 + (n_e - n_h)^2\mu_e^2\mu_h^2 B^2} \tag{4.1}$$

where μ_e and μ_h are electron mobility and hole mobility, repectively. In a compensated metal where $n_e = n_h \equiv n$, magnetoresistance is quadratic in the applied magnetic field

$$\rho_{xx}(B) = \frac{1}{ne(\mu_e + \mu_h)}\left(1 + \mu_e\mu_h B^2\right) \tag{4.2}$$

Figure 4.5 shows the plot between resistivity and B^2 at various pressure. The plots at low pressures follow a linear trend only in the high field regime, whereas the plot at 62 kbar shows the linearity in the whole magnetic field range. The slight discrepancy in our data from this equation may arise from the anisotropy of the Fermi surface since the simplified two-band model assumes an isotropic Fermi surface [73].

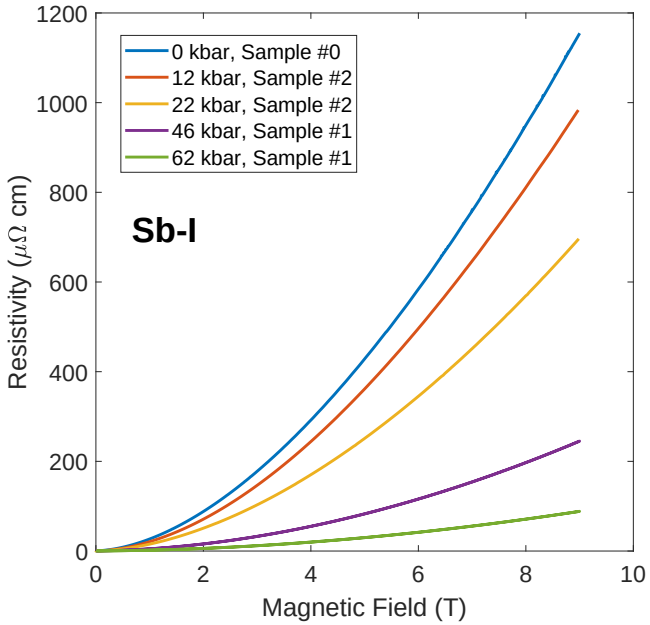

Fig. 4.4 Magnetoresistivity of Sb-I at 2K, at various pressures.

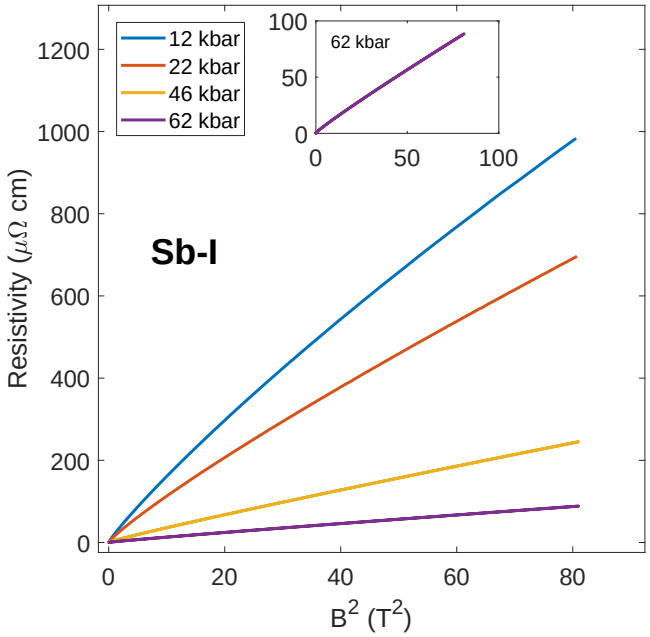

Fig. 4.5 Resistivity versus magnetic field squared of Sb-I at 2K, at various pressures. The inset figure shows the plot specifically of 62 kbar data for clarity. The axis of the inset is the same as the main plot.

There are two interesting features in the plots 4.4 and 4.5: (i) magnetoresistance decreases as a function of pressure, (ii) prefactor of the B^2-term reduced under pressure. According to equation 4.2, it is likely that the carrier density is enhanced by pressure. To determine this effect conclusively, we have to perform the quantum oscillation study.

We conclude this magnetoresistance section by investigating Kohler's plot. Kohler's rule states that a ratio $\rho(T,B)/\rho(T,0)$ is a universal function of $B/\rho(T,0)$ [1]:

$$\frac{\rho(T,B)}{\rho(T,0)} = f\left(\frac{B}{\rho(T,0)}\right) \tag{4.3}$$

The only assumption of Kohler's rule is that the mean free path is momentum-independent, making this rule quite general. Figure 4.6 show Kohler's plot at various pressures, showing excellent agreement with Kohler's rule.

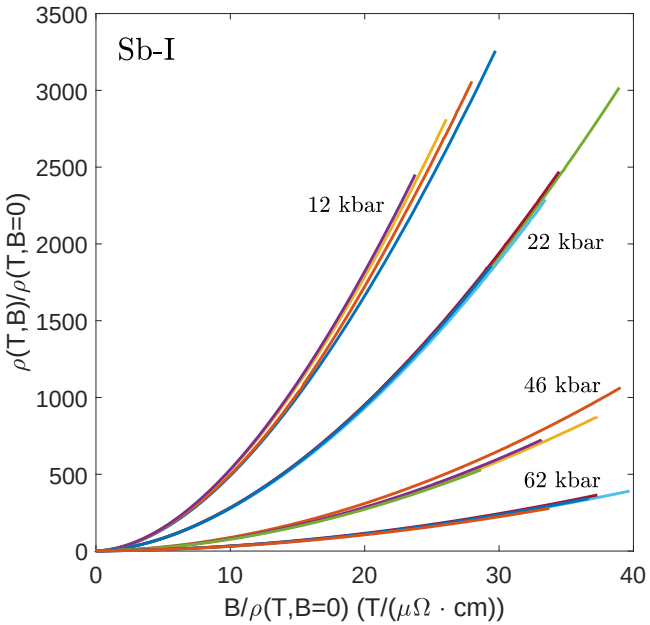

Fig. 4.6 Kohler plot in Sb-I at 2K, 4K, 7K, and 10K. The pressure range is from 12 kbar to 62 kbar.

Quantum Oscillation in Sb-I

We study the effects of pressure on the quantum oscillation frequency in this section. Due to the small Fermi surfaces in antimony, corresponding to a small frequency in quantum

oscillation, the fitting using the QFFT[2] programme may not be reliable. So instead, we use QFFT only as a guide and do a fitting carefully directly to the Lifshitz-Kosevich formula [128, 130]:

$$\rho \propto \left(\frac{8\pi}{e\hbar^7}\right)^{1/2} \frac{m^{*2}k_BT}{\left|A_k''\right|^{1/2}B^{1/2}} \sum_{p=1}^{\infty} \frac{\exp\left(-2\pi^2 pk_BT_Dm^*/e\hbar B\right)\cos\left(p\pi gm^*/2m_e\right)}{p^{-1/2}\sinh\left(2\pi^2 pk_BTm^*/e\hbar B\right)} \times \cos\left(2\pi p\left(\frac{F}{B}-\frac{1}{2}\right)\pm\frac{\pi}{4}\right) \quad (4.4)$$

where A_k'' is the Fermi surface curvature at the extremum cross-section, T_D is the Dingle temperature, m^* is the the electron effective mass, $g \approx 2$ is the electron g-factor, and F is the quantum oscillation frequency. Keeping in mind that we observed only one frequency and only the fundamental mode dominates, this equation is simplified greatly into

$$\rho \sim \frac{C_1}{\sqrt{B}} \times \frac{\exp\left(-C_2/B\right)}{\sinh\left(C_3/B\right)} \cos\left(\frac{2\pi F}{B}+C_4\right) \quad (4.5)$$

Figures 4.7 and 4.8 show the quantum oscillation in antimony from 0-33 kbar and the fit to the LK formula. We were unable to observe any quantum oscillation in the data at 46 kbar and 62 kbar, probably due to the Fermi surface enlargement (it is easier to observe the quantum oscillatory effect in a small Fermi surface). We note that the 12 kbar data does not fit well to the LK fitting because the oscillation contains more than one frequency, which can be seen clearly in the FFT spectrum in figure 4.11. The spurious frequency may come from the twinning effect in antimony, reported in some literature [59, 109]. Since antimony is not very soft as in bismuth, twinning is less likely to happen in antimony.

[2]QFFT is a Matlab code to perform fast fourier transform to the data. The output is the amplitude in frequency domain

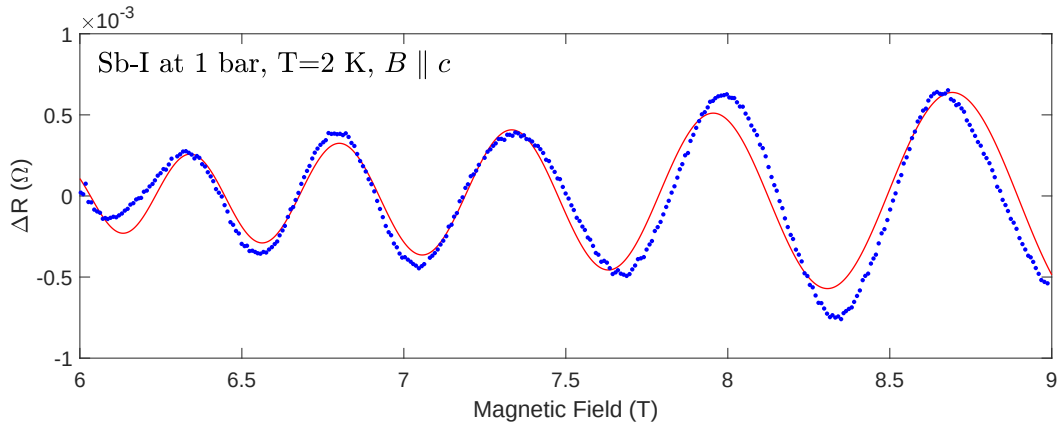

(a) 1 bar

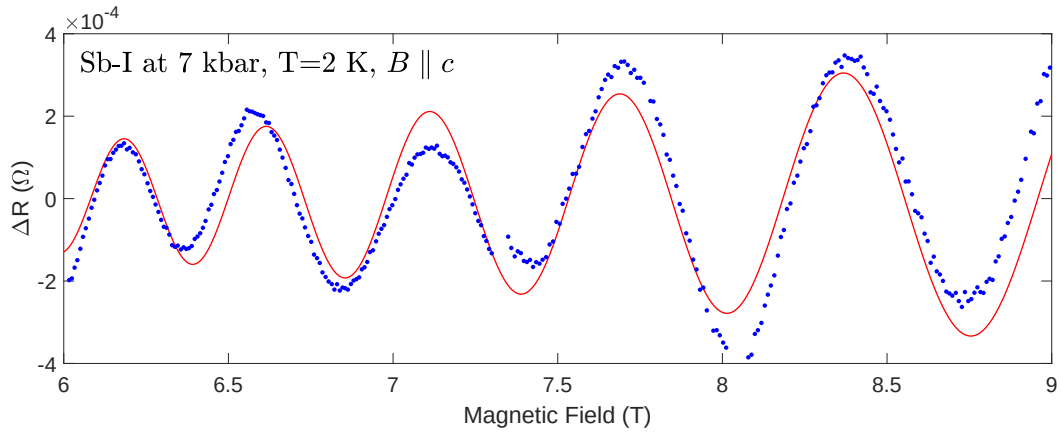

(b) 7 kbar

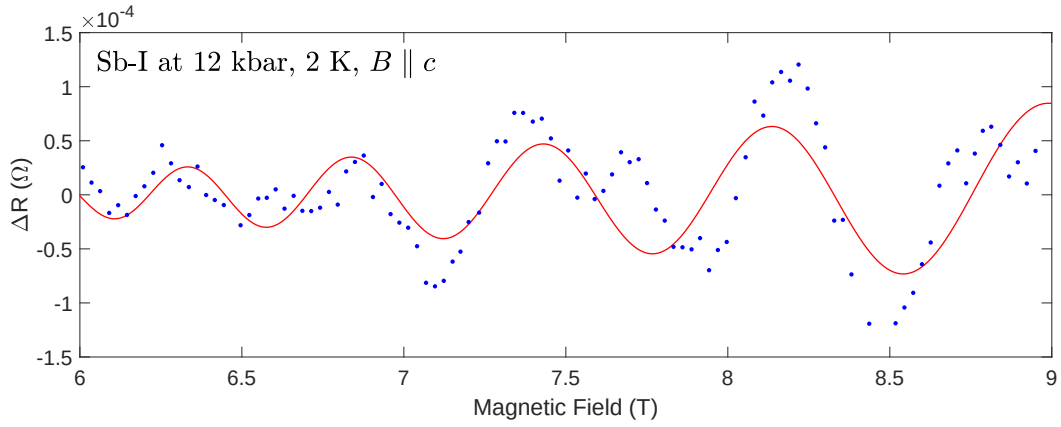

(c) 12 kbar

Fig. 4.7 Shubnikov - de Haas quantum oscillation in the moissanite anvil cell. The field $B \parallel c$ is parallel to the c-axis. The red curves show the fit to the LK formula. This figures contain data with pressure of 1 bar, 7 kbar, and 12 kbar

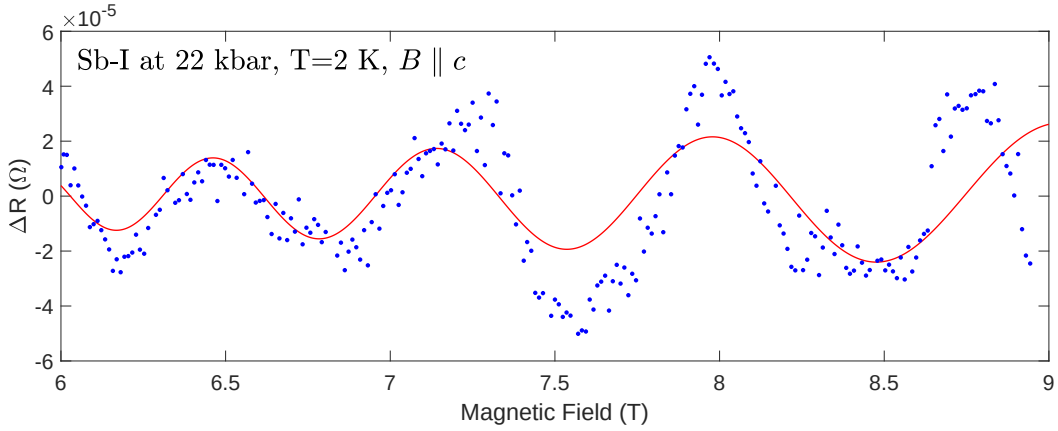

(a) 22 kbar

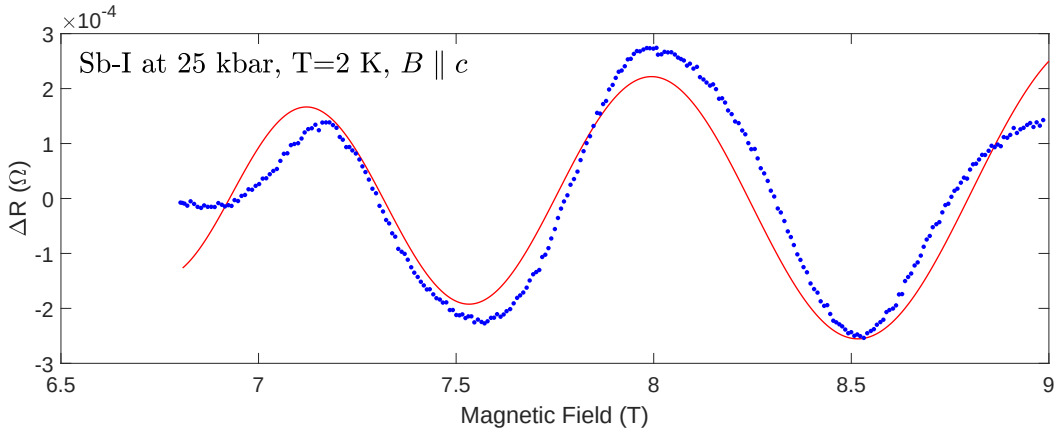

(b) 25 kbar

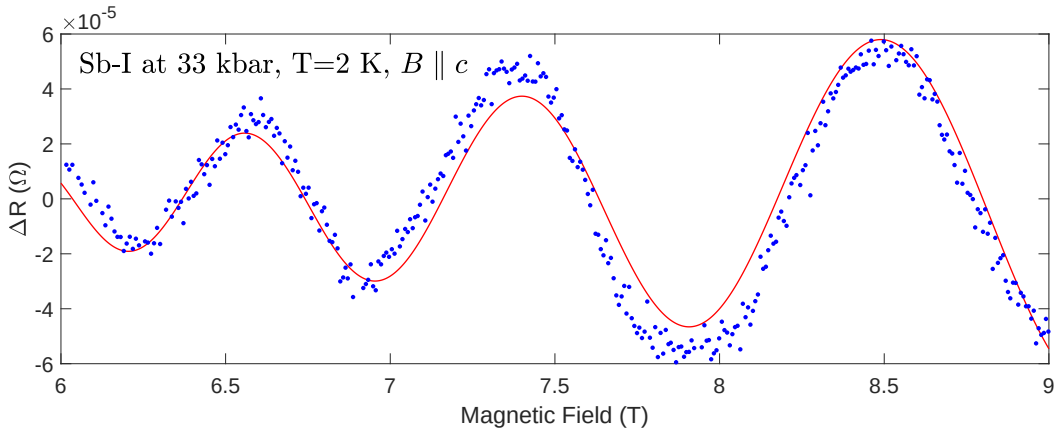

(c) 33 kbar

Fig. 4.8 Shubnikov - de Haas quantum oscillation in the moissanite anvil cell. The field $B \parallel c$ is parallel to the c-axis. The red curves show the fit to the LK formula. This figures contain data with pressure of 22 kbar, 25 kbar, and 33 kbar

The extracted frequencies from the data are summarised in the table 4.1. The quantum oscillation frequency decreases with increasing pressure. This result seems to contradict what has been found in previous literature. However, if the Fermi surface does not change isotropically, it could be possible that the Fermi surface in one direction gets squeezed, but overall volume still increases. The best methodology to investigate is to do a careful rotation study to map out the extremal cross-section of the Fermi surface at different angles, which can take up a long time. We solved this discrepancy by comparing our result to the data from a piston-cylinder pressure cell, in which the sample aligns in magnetic field differently from the anvil cell.

Quantum Oscillation Frequency in Sb-I for $B \parallel c$	
Pressure (kbar)	Quantum Oscillation Frequency (T)
0	92.6 ± 1.3
7	93.3 ± 1.5
12	83.1 ± 2.6
22	67.8 ± 0.2
25	64.1 ± 1.2
33	56.1 ± 1.7

Table 4.1 Quantum oscillation frequency as a function of pressure in moissanite anvil cell. The applied magnetic field is parallel to the c-direction.

Comparison to Results from Low-Pressure Piston-Cylinder Cell

We dedicate this subsection to compare our results in the anvil cells with the measurements from the piston-cylinder cell, which was set up and measured by Stephen Hodgson. What we are looking for is the quantum oscillation data at a different field orientation. Figures 4.9 and 4.10 show the quantum oscillation in antimony from 0-21 kbar and the fit to the LK formula. The extracted frequencies from the data are summarised in the table below

Quantum Oscillation Frequency in Sb-I for $B \perp c$	
Pressure (kbar)	Quantum Oscillation Frequency (T)
0	65.3 ± 0.3
5	65.3 ± 2.0
9	68.6 ± 0.1
12	67.5 ± 1.4
18	76.4 ± 4.6
21	84.9 ± 0.4

Table 4.2 Quantum oscillation frequency as a function of pressure in piston-cylinder cell. The applied magnetic field is perpendicular to the c-direction.

This result shows an opposite tendency to what has been observed in the moissanite anvil cell, with $B \parallel c$, suggesting that Fermi surface does not change isotropically and involves a deformation. Figure 4.12 summarises how the frequency varies under pressure in two cases - $B \parallel c$ and $B \perp c$.

The observation of anisotropic evolution of Fermi surface under pressure agrees well with the paper by EI-Rahman [51]. Our work expands the pressure range greatly to over 30 kbar, and it shows how strong the anisotropy is at high pressure. In this paper, the minimum value and the maximum value of hole's cross section is 61.86 T and 196.0 T, respectively. The quantum oscillation frequency when the magnetic field is parallel to the trigonal axis (which is equivalent to c-axis in our case) is approximately 90 T. This value agrees very well with our observed values. From our result (field parallel to c-axis), we can see that the hole pocket is elongated as pressure is applied. However, we cannot quantify the dimension in the other axis as we do not know at what angle the field is oriented on the ab-plane. The observation that the hole pocket is getting thinner at higher pressure may give us a hint to the question of why antimony becomes more metallic under pressure (i.e. higher carrier concentration), which is in contrast to bismuth and arsenic.

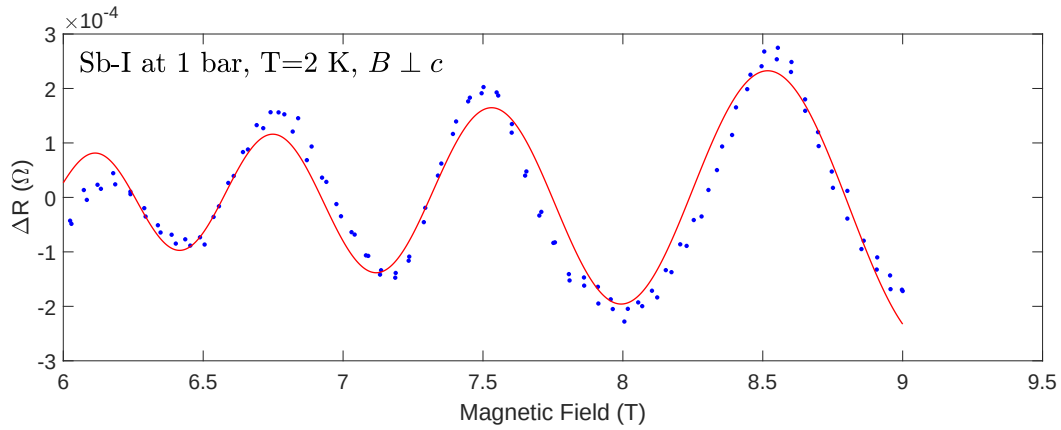

(a) 1 bar

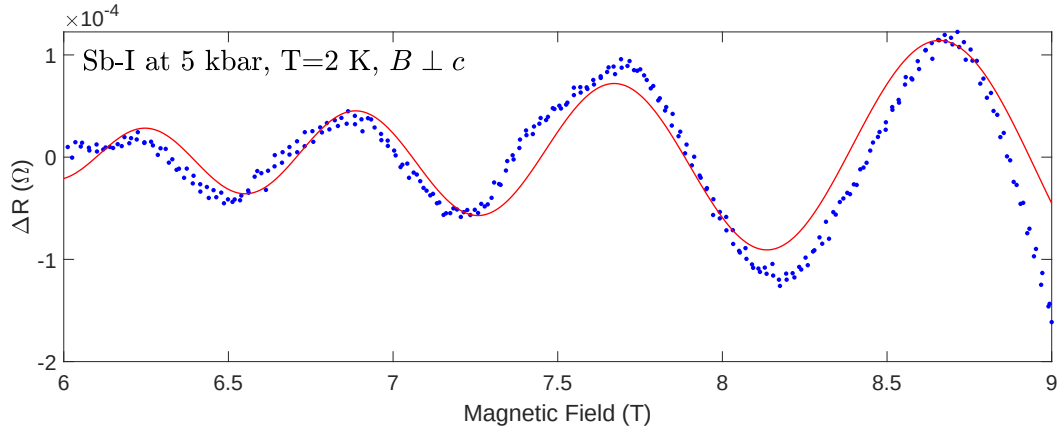

(b) 5 kbar

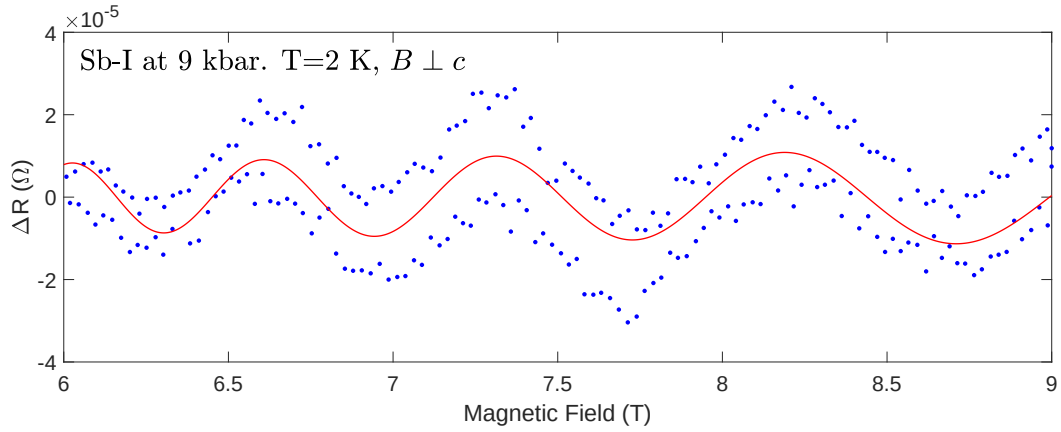

(c) 9 kbar

Fig. 4.9 Shubnikov - de Haas quantum oscillation in the clamp cell. The field $B \perp c$ is perpendicular to the c-axis. The red curves show the fit to the LK formula. This figures contain data with pressure of 1 bar, 5 kbar, and 9 kbar

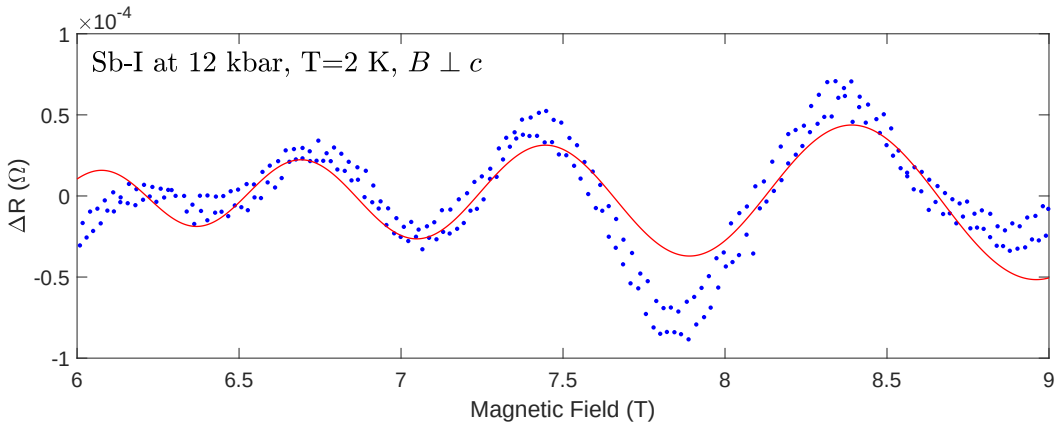

(a) 12 kbar

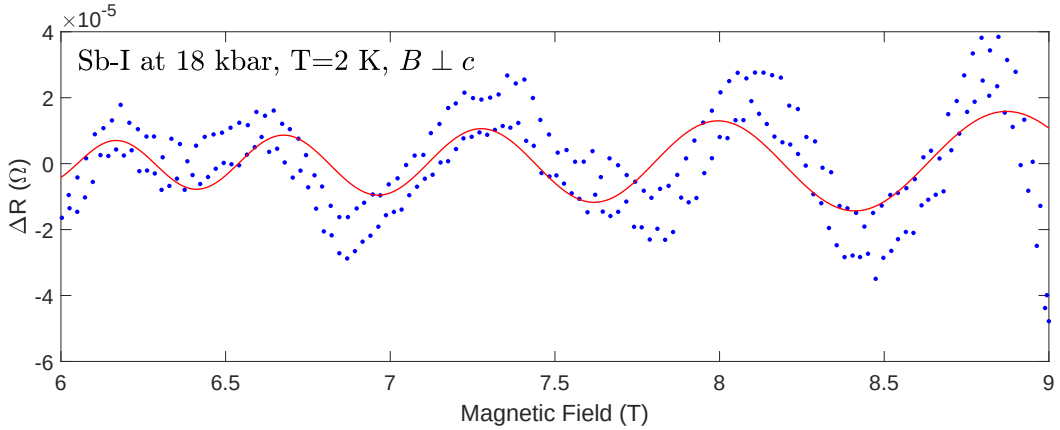

(b) 18 kbar

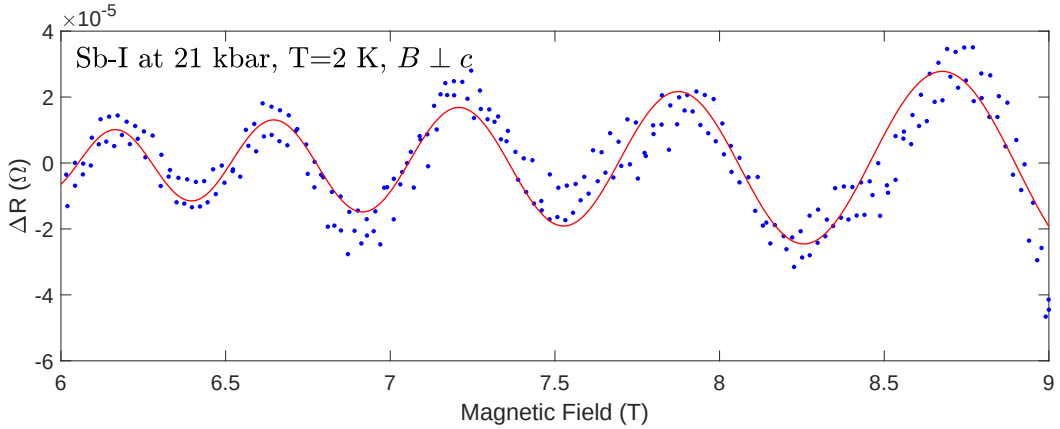

(c) 21 kbar

Fig. 4.10 Shubnikov - de Haas quantum oscillation in the clamp cell. The field $B \perp c$ is perpendicular to the c-axis. The red curves show the fit to the LK formula. This figures contain data with pressure of 12 kbar, 18 kbar, and 21 kbar

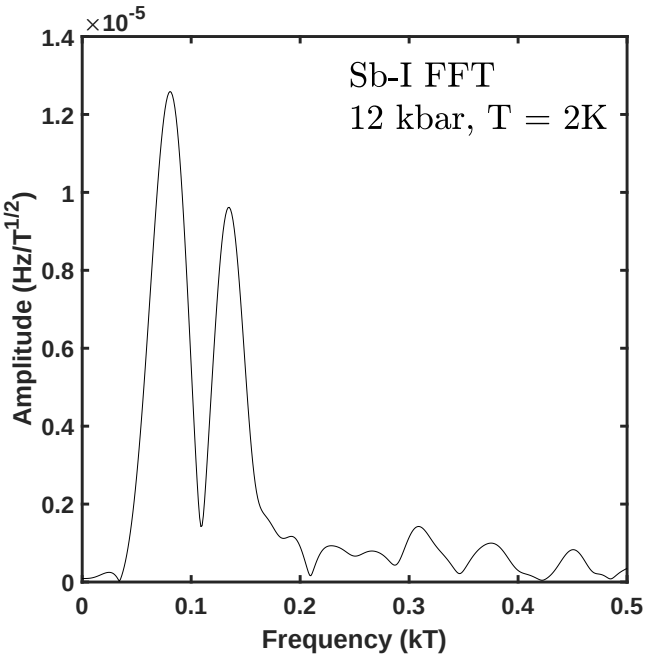

Fig. 4.11 FFT spectrum in the 12 kbar data of Sb-I.

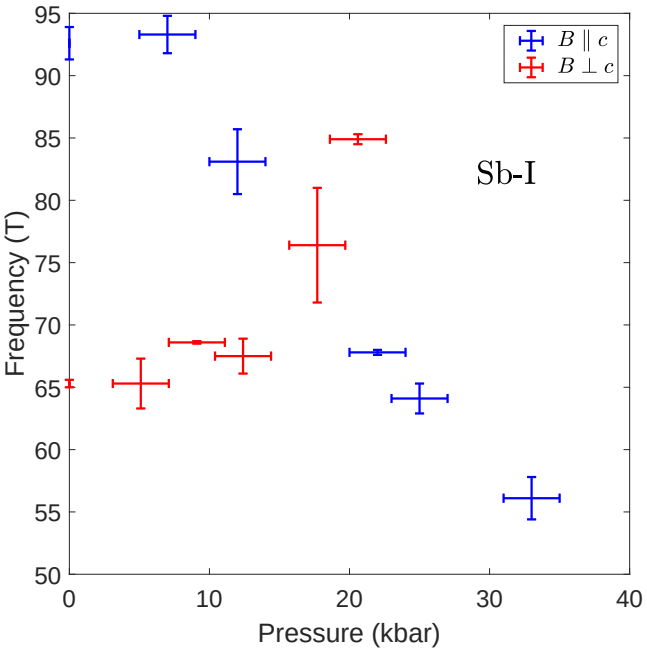

Fig. 4.12 A summary of the quantum oscillation frequency in Sb as a function of external pressure.

4.2 Sb-II

4.2.1 Introduction and Literature Review

The periodic nature of crystalline solids has been the most fundamental assumption in solid-state physics [12]. The observation of 10-fold symmetry in the x-ray diffraction pattern of aluminium-manganese, belonging to the icosahedral point group, was completely unexpected [129]. Perhaps, the most surprising thing is that this structure is fully ordered but does not repeat in any way in space (unlike amorphous, where they are disordered).

In this work, we focus on another kind of aperiodic structure - the incommensurate host-guest (H-G) structure. This H-G structure comprises host atoms and guest chains. The ratio between the lattice constant of host atoms and the guest chain is irrational, meaning that we cannot have the actual unit cell. The lack of unit cells poses many difficulties in understanding the system. For example, we do not have Brillouin's zone, making it very difficult to visualise the Fermi surface. Figures 4.13 show an incommensurate host-guest structure in Bi-III and Sb-II.

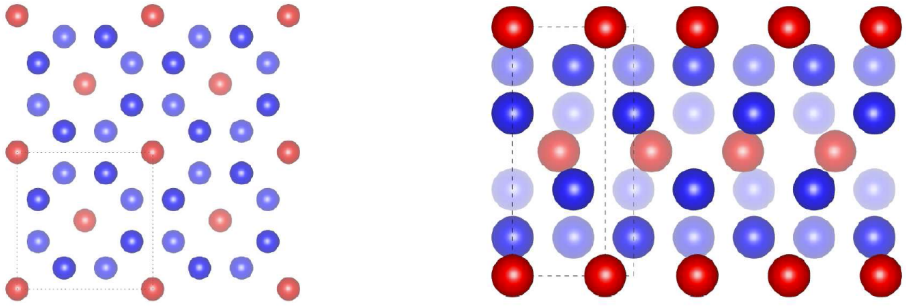

Fig. 4.13 Structure of the tetragonal host-guest incommensurate in both Bi-III and Sb-II. The left figure is the view from the c-direction whereas the right picture is the view from the a-direction. The red atoms represent guest and the blue atoms represent hosts. Figure credit: [27].

One of the most prominent features of the incommensurate host-guest structure is the emergence of a new low-frequency phonon mode. In a d-dimensional periodic lattice, it is not hard to see that there is one acoustic mode corresponding to each direction, making up d acoustic modes in total. Hence, there are $3N-d$ modes left to be optical modes, where N is the number of atoms in the unit cell. The H-G structure introduces another low-lying phonon in addition to the acoustic modes, resulting in the total $d+1$ low-lying phonon modes. The origin of this additional phonon mode comes from the fact that host atoms and guest chains

can slide through each other without changing the potential energy. Since the additional mode has a different origin and is specific to the H-G structure, we give it a particular name, 'sliding mode' or 'phason mode'. The dispersion in phonon perpendicular to the c-direction comes from coupling between chains. If the couple is weak enough, the phonon dispersion is essentially one-dimensional. The distortion can modulate the atomic position and lift the frequency. The flat dispersion relation of the sliding mode is a crucial ingredient for getting a strong electron-phonon coupling parameter, which can be understood by looking at the equation

$$\lambda = 2\int_0^{\omega_D} d\omega \frac{\alpha^2(\omega)F(\omega)}{\omega} \tag{4.6}$$

where λ is the electron-phonon coupling parameter (or the McMillan parameter). If $\omega \to 0$ in an extended region, the McMillan's parameter gets enhanced significantly. However, although there is also a region where $\omega \to 0$ in the acoustic phonons, it does not enhance the coupling parameter. This is because the mode $\omega \to 0$ in the acoustic modes is Goldstone's mode. This means that it associates with the whole lattice translation and gives a zero matrix element. By contrast, the sliding mode involves relative motion of host and guest sublattice and can therefore cause large matrix elements. This aspect makes the incommensurate host-guest structure to be a good candidate for studying strong coupling superconductivity.

Generally, the incommensurate host-guest structure is stable at high pressure in many element materials except for $Hg_{3-\delta}AsF_6$, which possesses the host-guest structure even at ambient pressure [62]. Some remarkable examples of high-pressure incommensurate elements are from groups 1, 2, 15, and 16 [91]. The table below gives information on some materials that possess an incommensurate structure.

A list of element materials that exhibit incommensurate host-guest structure					
Group	Material	Pressure Range (kbar)	c_H/c_G	Superconductivity T_c (K)	Reference
2	Ba-IV	126 - 450	1.390	5.0	[158]
2	Sr-V	>460	n/a	3-4	[49, 90]
2	Ca-VI†	>1220	n/a	$\sim$25	[9, 162]
15	Bi-III	28 - 77	1.310	7.1	[29]
15	Sb-II	86 - 280	1.310	3.6	[157]
15	As-III	410 - 970	1.305	$\sim$1.8	[33]

Table 4.3 Properties of some incommensurate host-guest material. †Based on computational calculation.

One exciting thing in the table above is that the ratio c_H/c_G is close to 4/3, consistent in every material, making it possible to construct an approximated commensurate supercell with $c_H/c_G = 4/3$ containing 42 atoms in a unit cell of Bi-III and Sb-II. Amongst elements, bismuth draws the most attention to study the incommensurate phase since the pressure requirement is relatively low compared to others, hence achievable in piston-cylinder pressure cells. Before Dr Philip Brown did the work in Bi-III, the only thing we knew in Bi-III was that it has an incommensurate structure and undergoes the superconducting transition at 7.1 K. His thorough investigations of high-pressure resistivity and magnetisation, combined with numerical calculations, have shed light on physics and excitations of the underlying system [27]. The key results from the study of Bi-III are

1. Bi-III is a type-II superconductor with a very large electron-phonon coupling constant $\lambda \simeq 2.75$ [29]. Both properties are very unusual in an element material

2. Resistivity in the normal state right above superconducting shows a strong linear relationship with temperature (figure 4.14), which is evidence of strong electron-phonon coupling.

3. A huge upper critical field $B_{c2} = 2.5$ T is the highest value recorded amongst element metals.

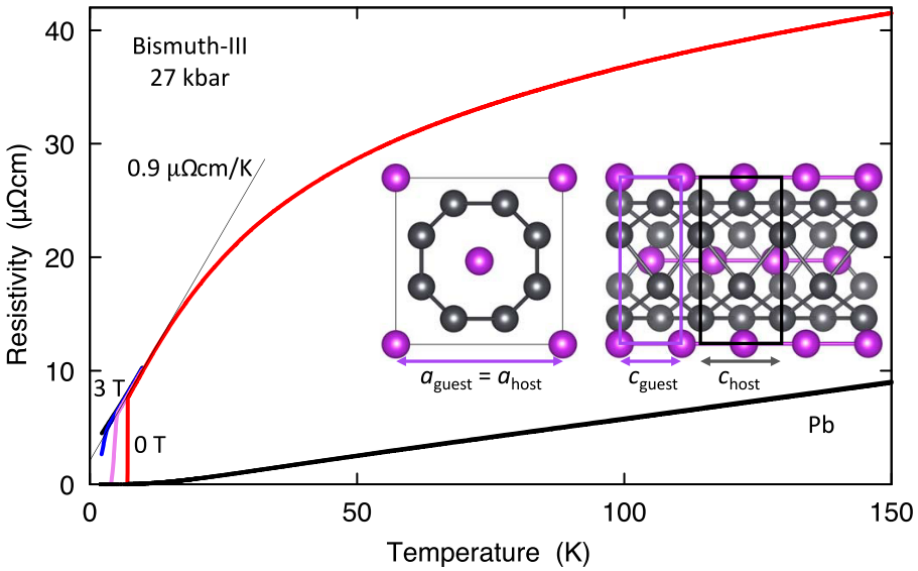

Fig. 4.14 Resistivity in Bi-III [29].

As well as in the bismuth case, there are still not yet many detailed studies in the other incommensurate host-guest materials, especially the effects of the phason mode on the superconductivity. There is a set of data that shows how resistivity looks like in Ba-IV [99]. Unsurprisingly, low-temperature resistivity in Ba-IV also exhibits a linear trend (figure 4.15) as in Bi-III, which is possibly evidence of strong electron-phason coupling.

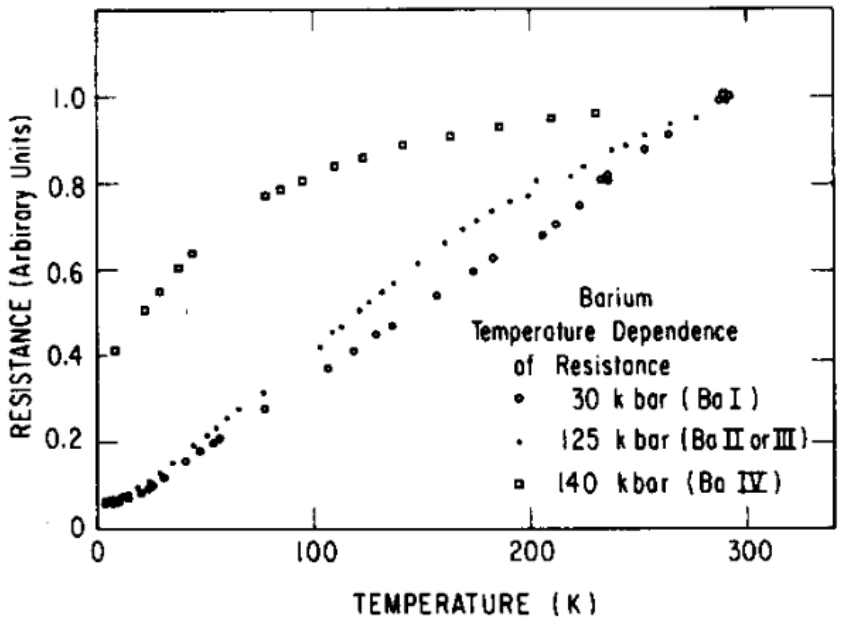

Fig. 4.15 Resistivity in Ba-IV [99].

Having learned all of these, we seek more systems to investigate with one objective in our mind: to compare a well-known system with other similar systems and analyse any robust features they shared or any differences. It is possible in this way also to validate any limitation of the theory for systems of this kind. The suitable material that we can work on would be antimony because (i) it is the most similar to bismuth, sharing the same crystal structure and the same electronic structure (ii) the required pressure of 86 kbar is somewhat accessible, second to only bismuth.

There are literature on Sb-II available, mainly focus on optical measurements. The phase diagram of antimony (figure 4.16) was studied in [42] using the high-pressure X-ray diffraction technique. Some publications also support the existence of a monoclinic incommensurate Sb-IV phase between Sb-I and Sb-II phases [45, 95, 151]. The superconductivity in Sb-II has been confirmed in resistivity measurement, showing a drop in resistance at about 3.5 K [157]. However, there is no transport study beyond this.

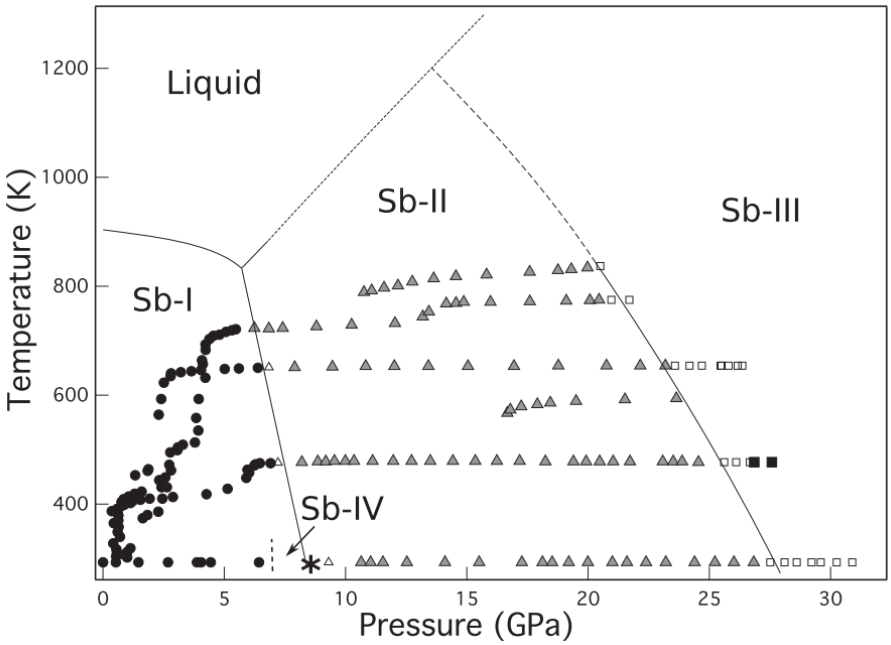

Fig. 4.16 Phase diagram of element antimony. The figure is from [42]

Finally, many intriguing effects happen when tuning the interaction between hosts and guests. Some examples are (i) Chain melting - it was observed in K-III abd Rb-IV that the guest chains 'melt away', losing their long-range order and turn into 1D liquid state [92, 121]. The origin of the chain melting was speculated to come from the reduction in the interaction between chains. (ii) Aubry's transition - it was theoretically predicted that when the interaction between hosts and guests is strong enough, the system undergoes an incommensurate-to-commensurate transition [13]. The interaction between chains can be observed via x-ray diffraction. The large modulation gives rise to strong satellite peaks. In Bi-III, the modulation can be seen in the diffraction pattern (figure 4.17). However, this modulation is much stronger in Sb-II, suggesting a strong coupling between host atoms and guest chains (figure 4.18).

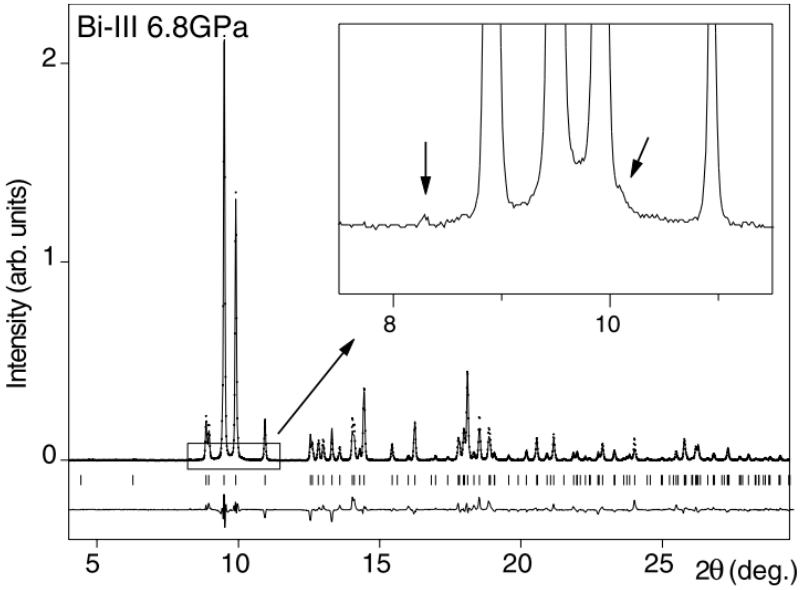

Fig. 4.17 Diffraction Pattern in Bi-III. The arrows indicate the peaks from the modulation reflection [91].

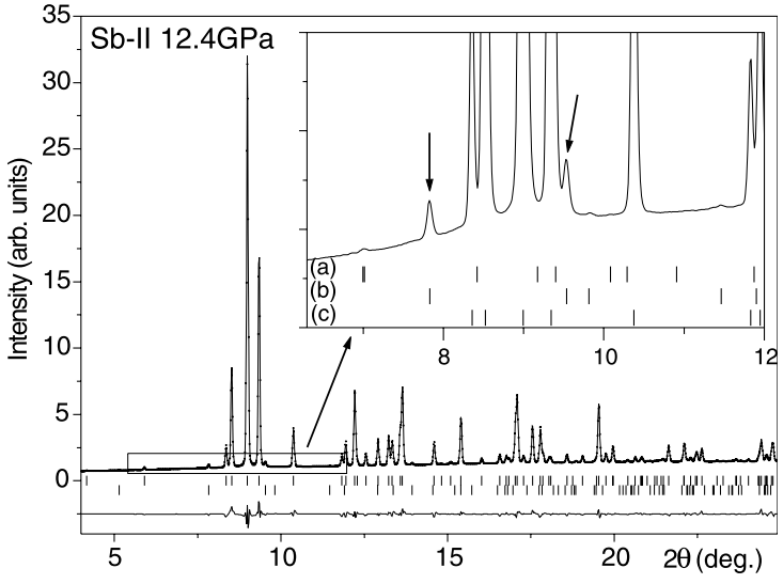

Fig. 4.18 Diffraction Pattern in Sb-II. The arrows indicate the peaks from the modulation reflection [91].

4.2.2 Results and Discussions

Resistivity Measurement in Sb-II

Antimony samples were obtained from Alfar Aesar company with 99.999% purity. It is purified further in a 'distil' process where samples of antimony were put in a long sealed quartz ampoule with high vacuum. One end of the tube is heated above the melting point of antimony, whereas the other end is below it. Resistivity measurements of Sb-II have been done using the standard 4-point measurement. The measurements were carried out in a diamond anvil cell with 0.7 mm culet size. The insulating gasket was used in these measurements to avoid a possibility of shorting to the pressure cell. The way we extract the resistivity value is by measuring the same sample at zero pressure. Then, the geometrical factor can be obtained by comparing this value with the literature (41.7 $\mu\Omega$·cm at room temperature, zero pressure). Glycerol was used as a pressure medium. We have measured two different samples of Sb in this phase, up to 110 kbar. Figure 4.19 shows a sample with a gasket used in the experiment.

Fig. 4.19 A sample of antimony in the pressure cell with insulating gasket. The size of the sample is approximately 80μm $\times$ 80μm $\times$ 20μm and the size of the hole is $300\mu m$

Figure 4.20 shows the resistivity profile of Sb-II from room temperature down to 2 K. In sample #8, we managed to measure at only one pressure point and the pressure cell failed afterward. In sample #9, we measured from 95 kbar to 110 kbar, subsequently reduced pressure back to 60 kbar, and finally repressurised back up to 96 kbar. There are a few

features to be noted here. Firstly, the wiggle in resistivity which appears at high temperature. Secondly, the observed superconductivity at 3.4 K - 3.6 K. Thirdly, the flattening of the resistivity before the material goes superconducting. Fourthly, the large residual resistivity. And finally, the negative curvature of the resistivity at high temperatures.

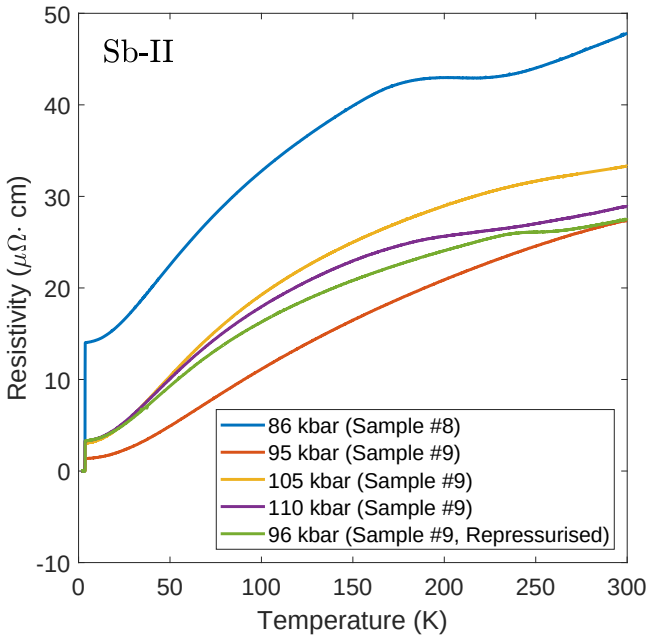

Fig. 4.20 The resistivity of Sb-II at various pressures.

We are starting with the high-temperature wiggle, which is very robust in our measurements of Sb-II. These wiggles come with a strong hysteresis in temperature, suggesting some first-order phase transition. There are a few situations where the first-order transition can occur. In our case, it is likely to be a structural transition since antimony is non-magnetic. The hysteresis is shown in figure 4.21. As there are literature suggesting the existence of Sb-IV between Sb-I and Sb-II, in which the transition between them is first-order nature [42, 45], one may interpret this to be the transition between Sb-IV and Sb-II. However, the pressure range for Sb-IV to be stable is less than 90 kbar, whereas the hysteresis in resistivity persists even at above 100 kbar in our data. Therefore, the Sb-II to Sb-IV interpretation is not conducing.

Another possibility of this high-temperature transition is the Aubry transition. According to the diffraction pattern in Sb-II, it has very strong satellite peaks, suggesting strong modulations. Once the interaction between host atoms and guest chain is strong enough, the system can undergo a structural transition from incommensurate to commensurate with

defects. The constant large residual resistivity at 96 kbar, 105 kbar and, 110 kbar (with the RRR of less than 10 whereas the RRR was above 100 in the Sb-I phase) also supports this interpretation - the constant density induced defects contribute to a large constant ρ_0. The discrepancy of ρ_0 in the 86 kbar and 95 kbar data may come from the mixture between two phases (more evidence on this when investigating superconductivity in the magnetic field). Because some publications suggest the mixture of two phases around this pressure range [42, 45], this situation is not entirely impossible. Although the large residual resistivity in Bi-III (even with very pure samples) was interpreted to be disorder induced by the transition, the large ρ_0 in Sb-II seems to be an intrinsic property of this phase as ρ_0 in Bi-III varied by over 10% between measurements [27] (ρ_0 in Sb-II shows similar value even after the repressurisation from 60 kbar to 96 kbar).

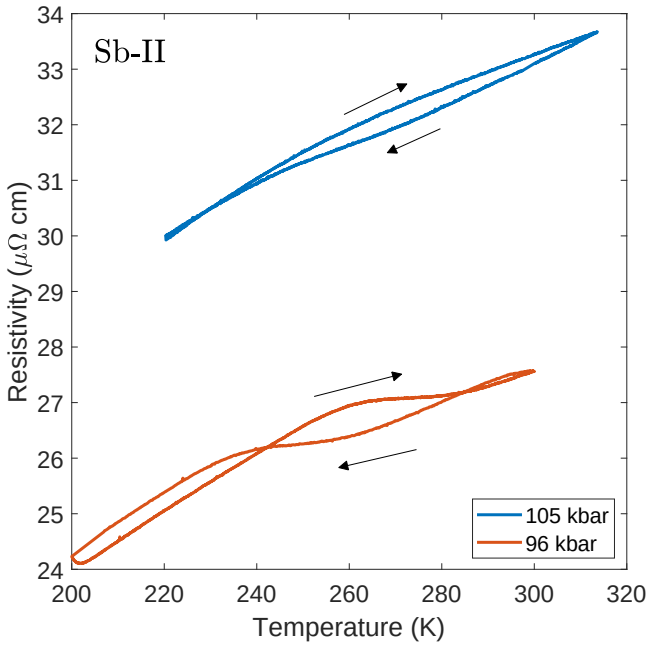

Fig. 4.21 Hysteresis in Sb-II at high temperature. The arrows indicate direction of the change in temperature.

With the interpretation of the phason's pinning, we can also explain the flattening of the resistivity curve above the superconducting phase. This flattening feature is very different from what has been observed in Bi-III, in which the resistivity above the superconducting state is very linear. Figure 4.22 shows the low-temperature resistivity, plotting against both temperature and temperature-squared. The plot with temperature-squared is mostly linear, suggesting Fermi-Liquid behaviour in this Sb-II phase. The linear resistivity in bismuth-III

arises from the scattering between electrons and phasons, which are contributed by the flat dispersion relation. When Aubry's transition happens, phasons get pinned, and we thus expect a weak electron-phason coupling, which gives rise to the quadratic resistivity instead of linear. By extracting the A-coefficient from the graph, we obtain $A = 3.06 \times 10^{-3}\ \mu\Omega \cdot \mathrm{cm} \cdot K^{-2}$. Comparing this value with other heavy-fermion materials in the Kadowaki-Wood diagram (figure 4.23), the A-coefficient in Sb-II resistivity is anomalously large despite being an element. We are still unable to explain the large A-coefficient in Sb-II. To understand the origin of this anomaly, we wish to study a few things: (i) Heat capacity in Sb-II - Such a study will provide us the location of Sb-II in the Kadowaki-Wood diagram and will give us the coefficient $\alpha = A/\gamma^2$. It is vital to obtain this value since it $\alpha \sim n_e^{-2}$, meaning that we can relate it to the carrier density [43]. (ii) Quantum oscillation - we can extract effective mass from this study. Moreover, it is fundamentally interesting if one could observe quantum oscillation in an aperiodic material. However, this study may not be suitable for Sb-II since it shows a large residual resistivity.

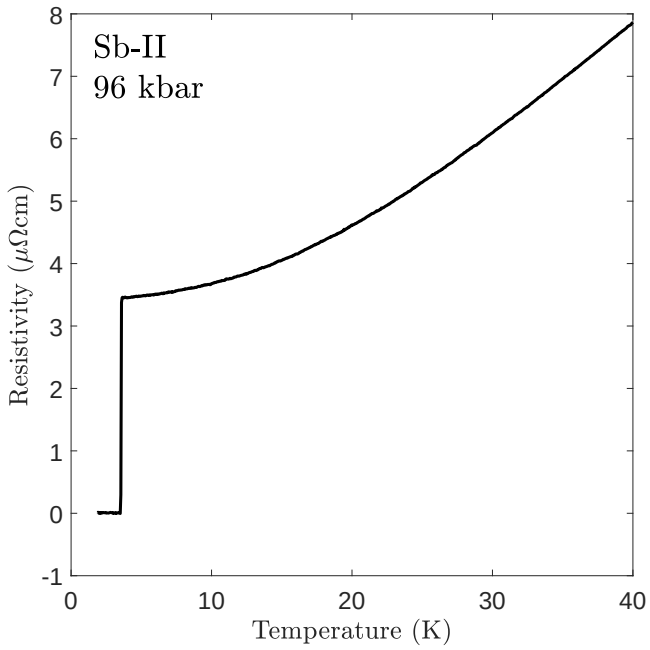

(a)

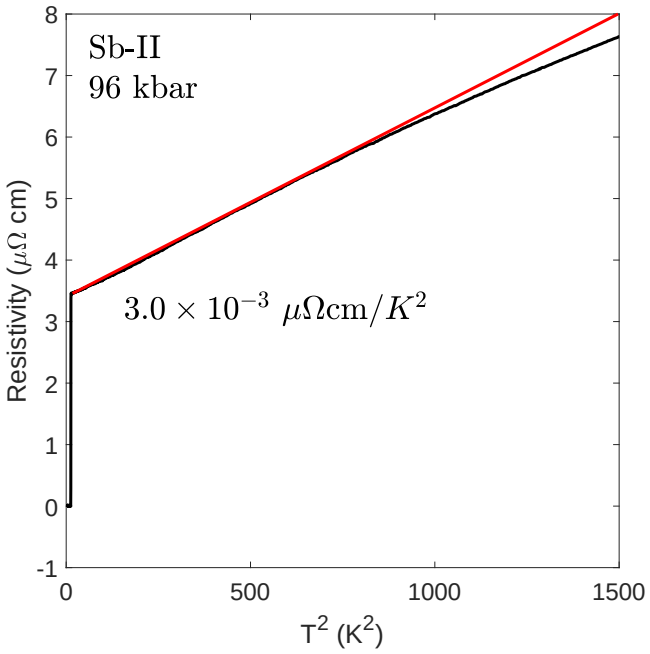

(b)

Fig. 4.22 Low temperature resistivity of Sb-II at 96 kbar from 2 K to 40 K. The figure (a) shows the plot with temperature whereas the figure (b) shows the plot with the temperature-squared.

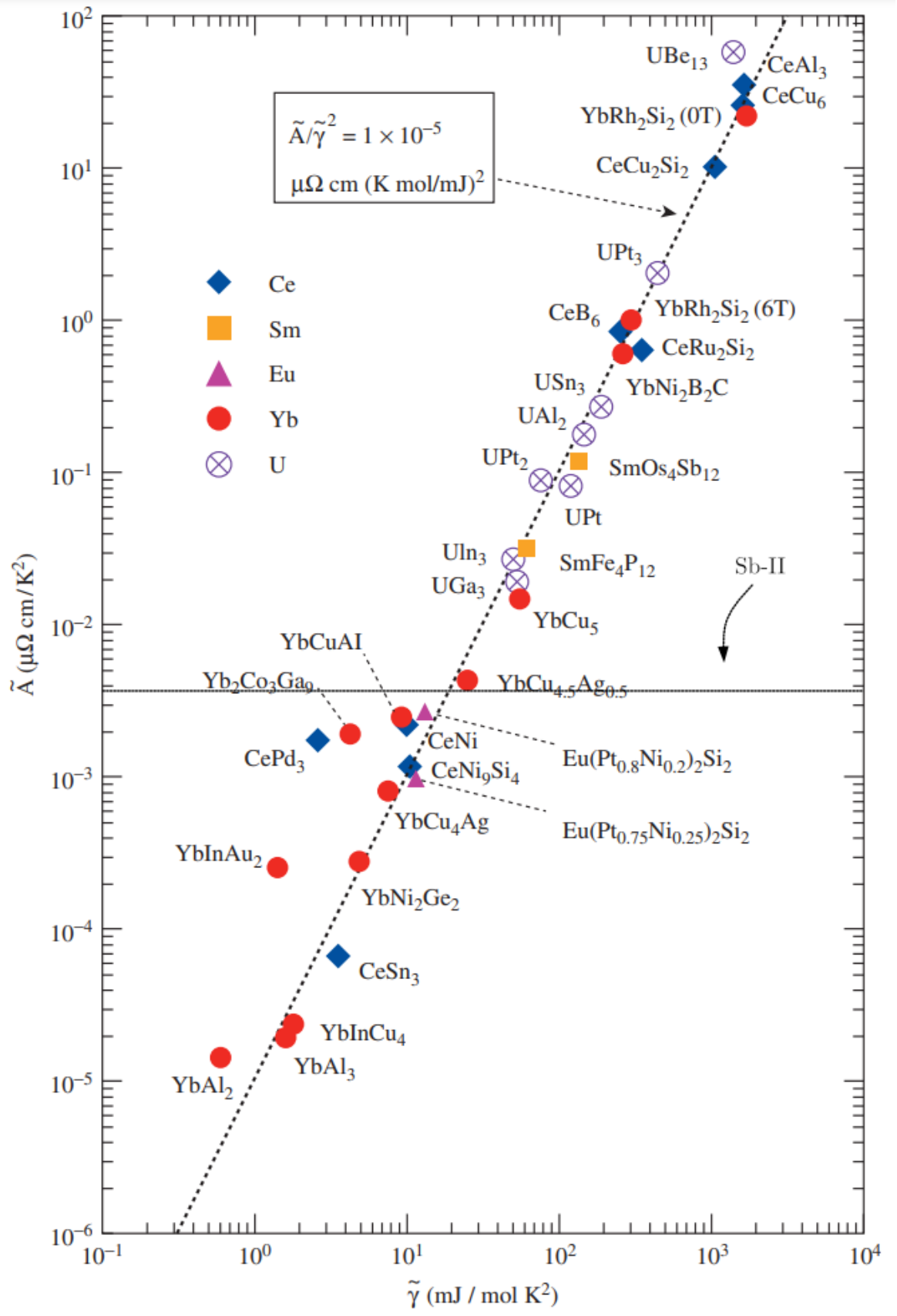

Fig. 4.23 Kadowaki-Wood diagram taken from [43]. The horizontal dash line is added to indicate the A-coefficient of Sb-II.

Superconductivity in Sb-II

Although the superconductivity in Sb-II has been discovered for a few decades [157], there is no detailed study of this superconductivity available. Therefore, it is crucial to study the system thoroughly and compare our results with the previous study in Bi-III. We study the superconductivity Sb-II using both resistivity and DC magnetisation measurements in this section (for the Meissner effect study), which are necessary to obtain the complete picture of this superconductivity state.

We start with the superconducting transition in resistivity measurement in figure 4.24. The transition temperature is approximately $T_c = 3.5 \pm 0.1$ K, varying slightly in the pressure range between 96-110 kbar. Next, we investigate the effect of the magnetic field on the transition temperature in the resistivity measurement, shown in figure 4.25. As the magnetic field of less than 0.3 T completely suppresses the transition, it confirms that this is indeed the superconducting transition. Before going further, let us also discuss the low-temperature resistivity in the field at other pressure points. As we interpreted in the previous section that the discrepancies of ρ_0 in the 86 kbar and 95 kbar data come from the mixture between Sb-I and Sb-II, our interpretation is supported by the magnetoresistivity measurement. The 86 kbar and 95 kbar data in figure 4.26 show upturns before going fully SC, indicating a sign of non-homogeneity in the sample (as it causes a redistribution of the current paths).

To analyse the superconducting parameters, we plot the superconducting transitions as a function of the magnetic field and extrapolate to get the value of the critical fields. Figure 4.27 shows the plot of superconductivity transition temperature against the magnetic field. The red line in the plot is fitted to equation [74]

$$B_{c2}(T) = B_{c2}(0)\left(\frac{1-\left(\frac{T}{T_c}\right)^2}{1+\left(\frac{T}{T_c}\right)^2}\right) \tag{4.7}$$

The parameters obtained from the fit are $B_{c2}(0) = 0.212$ T and $T_c = 3.57$ K.

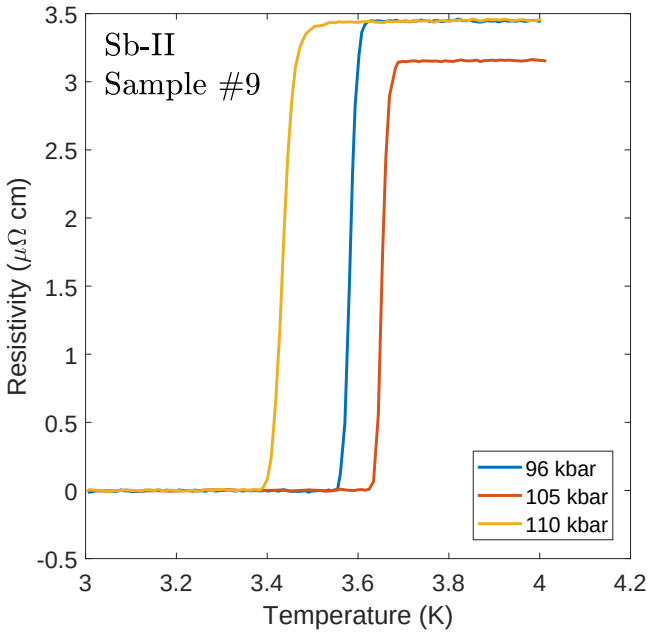

Fig. 4.24 Resistivity of Sb-II in low temperature, showing a sharp superconducting transition.

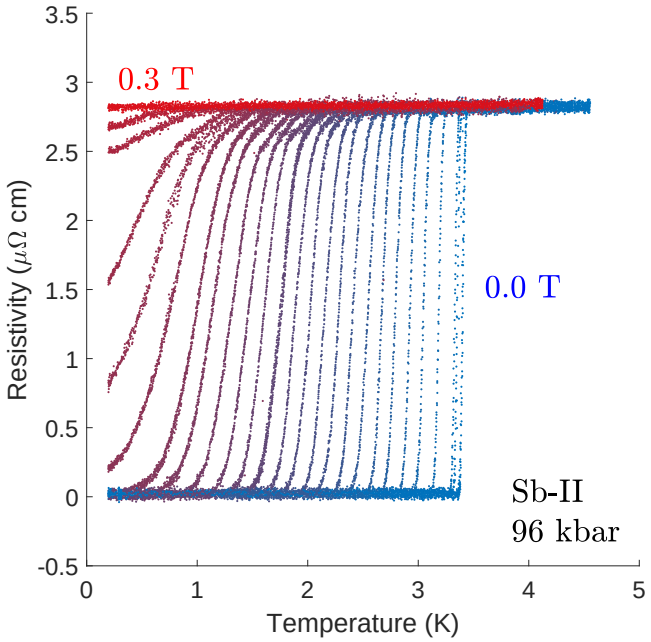

Fig. 4.25 Resistivity of Sb-II in low temperature with magnetic field. The field ranges from 0 T to 0.3 T.

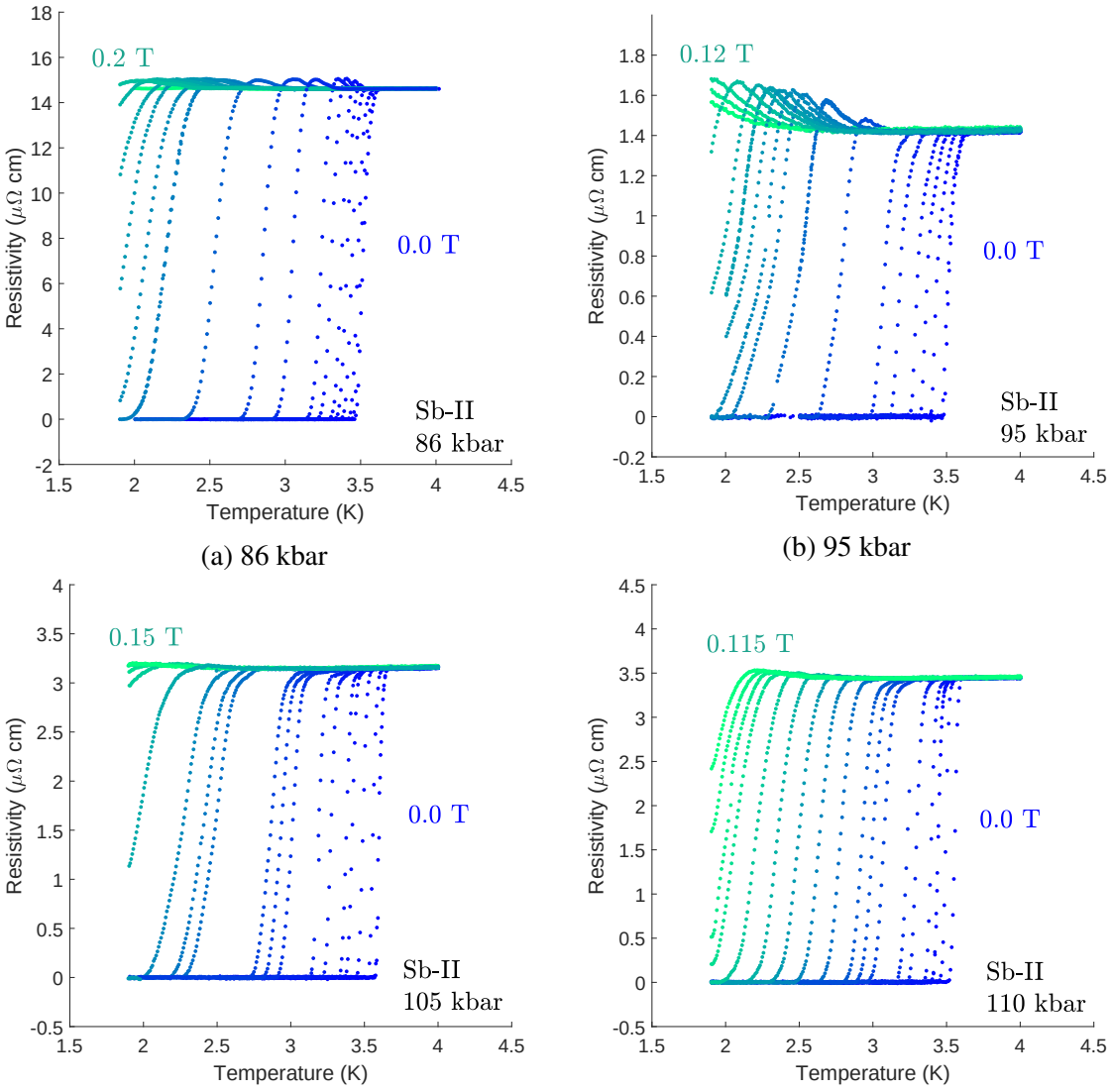

(a) 86 kbar

(b) 95 kbar

(c) 105 kbar

(d) 110 kbar

Fig. 4.26 Resistivity of Sb-II in low temperature with magnetic field.

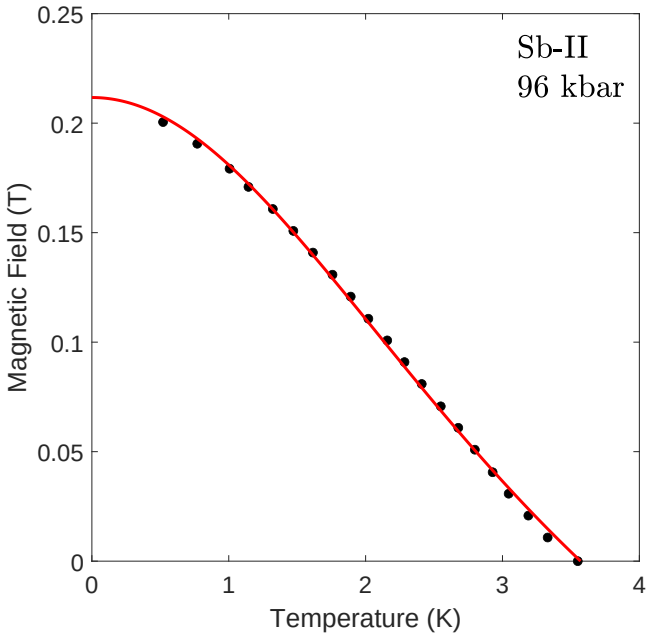

Fig. 4.27 The plot of the critical temperature versus magnetic field to estimate the upper critical field B_{c2} of Sb-II at 96 kbar. The red line is the fit to equation 4.7.

DC magnetisation of the Sb-II has been measured in the SQUID cell[3], and the measurement was done in the MPMS measurement system. However, as the sample size is about a million times smaller than the pressure cell, the background from the cell is overwhelmingly large. For this reason, the cell was made of copper-titanium alloy to minimise the background while keeping a good strength. Thanks to how sensitive SQUID magnetometry is, we can measure the sample DC magnetisation by measuring both the empty cell and the cell with a sample inside, then subtract these two signals to get the sample signal. The subtraction of between two signals was analysed using SquidLab [40]. Figure 4.28 shows the DC magnetisation versus temperature for the different input magnetic fields. Due to the limitation in the cooling power of MPMS, we could only obtain a few superconducting data in a very small range, from 2 K to 3.5 K, which is the range between the transition temperature at zero field and the base temperature of measurement system. The problem of blockage and temperature control in the MPMS also make the data becomes less accurate. Thus, we only obtained a crude estimated value for the lower critical field B_{c1}.

[3]The SQUID cell was designed by Dr Patricia Lebre Alireza - so another name of this cell is LA cell!

Figure 4.29 shows the relationship between critical temperature measured in the DC magnetisation and the applied magnetic field. The data is fitted to the equation [27]

$$B_{c1}(T) = B_{c1}(0)\left(1 - \left(\frac{T}{T_c}\right)^2\right) \tag{4.8}$$

The parameters obtained from the fit are $B_{c1}(0) = 12.8$ mT and $T_c = 3.50$ K.

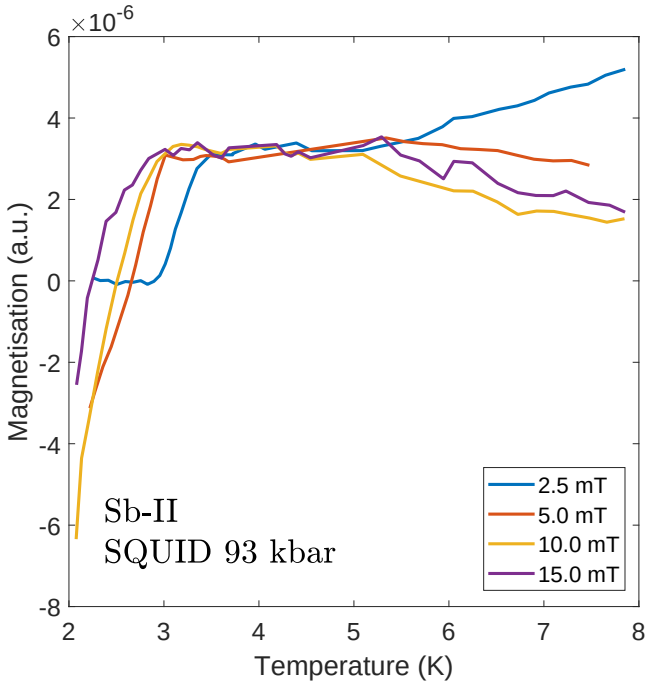

Fig. 4.28 The plot of the DC magnetisation in Sb-II at 93 kbar as a function of temperature at difference input field.

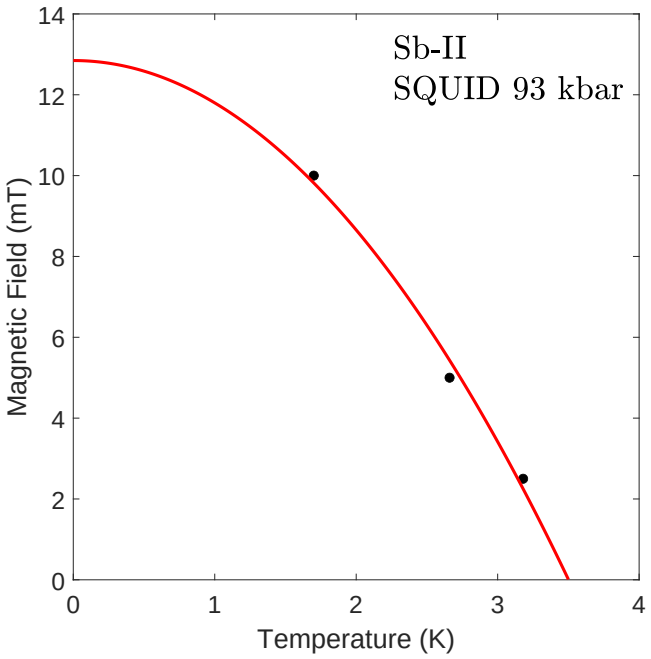

Fig. 4.29 The plot of the critical temperature versus magnetic field to estimate the lower critical field B_{c1} of Sb-II at 96 kbar. The red line is the fitting to the Ginzberg-Landau theory, and is the guide to the eyes.

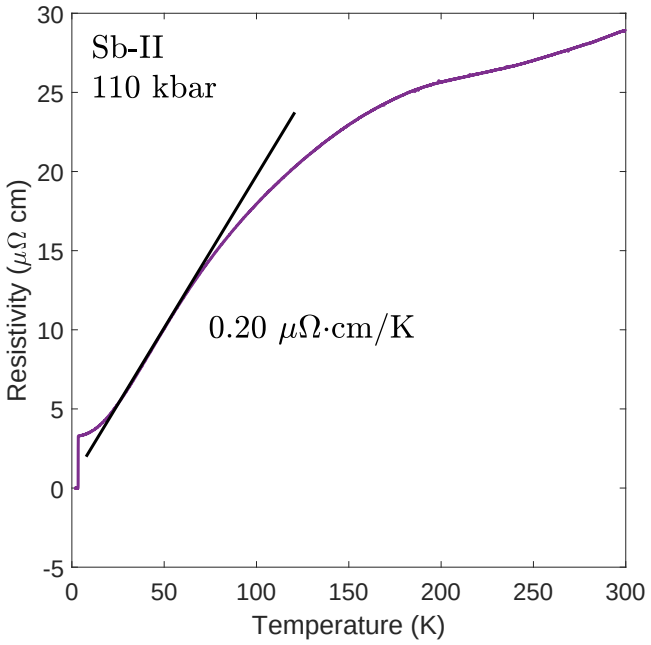

Fig. 4.30 Figure showing the fit of Sb-II resistivity in the linear regime.

These values of the upper critical field and the lower critical field can be translated into coherence length and penetration depth, respectively. The Ginzberg-Landau theory gives us $l_\xi = 39.6 \pm 2.8$ nm and $l_\lambda = 113 \pm 13$ nm, where l_ξ is the coherence length and l_λ is the penetration depth. To get the idea of how strong the electron-phason coupling parameter is, we look at the equation [29]

$$\lambda = \frac{\varepsilon_0 \hbar \Omega_p^2}{2\pi k_B} \frac{d\rho}{dT} + \Delta\lambda \tag{4.9}$$

where $\Delta\lambda$ is the contributions from high-frequency phonons $\hbar\omega \gg k_B T$, and Ω_p is the plasma frequency. The derivation of this equation is provided in [29], which uses the Bloch-Grüneisen formula [60]

$$\rho(T) = \rho_0 + \frac{4\pi}{\varepsilon_0 \Omega_p^2} \sum_{\boldsymbol{q}} \alpha_{\boldsymbol{q}}^2 T (\partial n_{\boldsymbol{q}} / \partial T)_{\omega_{\boldsymbol{q}}} \tag{4.10}$$

where $\alpha_{\boldsymbol{q}}$ is the effective electron-phonon matrix element averaging over Fermi surface, and $n_{\boldsymbol{q}} = \left(\exp\left(\hbar\omega_{\boldsymbol{q}}/k_B T\right) - 1\right)^{-1}$ is the Bose occupation number. For low-frequency phonon $\hbar\omega_{\boldsymbol{q}} \ll k_B T$, the exponential term in the denominator can be approximated to be $\exp\left(\hbar\omega_{\boldsymbol{q}}/k_B T\right) \approx 1 + \hbar\omega_{\boldsymbol{q}}/k_B T$ and hence

$$\rho = \rho_0 + \frac{4\pi k_B T}{\varepsilon_0 \hbar \Omega_p^2} \sum_{\boldsymbol{q}} \frac{\alpha_{\boldsymbol{q}}^2}{\omega_{\boldsymbol{q}}} \tag{4.11}$$

The summation in the equation above basically represents the McMillan parameter (or electron-phonon coupling parameter) as in equation 2.44: $\lambda = 2\sum_{\boldsymbol{q}} \alpha_{\boldsymbol{q}}^2 / \omega_{\boldsymbol{q}}$. Finally, we arrived at

$$\frac{d\rho}{dT} = \frac{2\pi k_B}{\varepsilon_0 \hbar \Omega_p^2} \lambda \tag{4.12}$$

Hence, in the limit where the phason contribution is much larger than the high frequency phonons contribution, we have

$$\lambda \approx \frac{\varepsilon_0 \hbar \Omega_p^2}{2\pi k_B} \frac{d\rho}{dT} \tag{4.13}$$

Furthermore, the London penetration depth, McMillan's parameter, and plasma frequency can be related together via the equation [27, 29]

$$l_\lambda = \frac{(1+\lambda)^{1/2} c}{\Omega_p} \tag{4.14}$$

where c is the speed of light. Combining equation 4.13 and 4.14, we arrived at the final equation

$$\lambda = \left(\frac{2\pi k_B l_\lambda^2}{\varepsilon_0 \hbar c^2 \rho'} - 1 \right)^{-1} \tag{4.15}$$

The problem here is the quadratic behaviour in resistivity at low temperature, which does not let us to extract the ρ' at low temperature. Instead, we extracted ρ' in the linear regime, which is between 30-50 K in our case. By plugging in our measured parameters, $l_\lambda = 113 \pm 13$ nm and $\partial\rho/\partial T = 0.20 \pm 0.5$ $\mu\Omega$·cm/K (fitted in figure 4.30), we obtained $\lambda = 0.18 \pm 0.06$. This coupling constant between electrons and the sliding modes is surprisingly small compared to the value of $\lambda = 2.75$ in Bi-III. Obviously, the assumption that we can neglect the contribution from high-frequency phonon must break down at this point, but it does not change the fact that the coupling constant of electron-phason is really small. The table below compares these parameters between Bi-III and Sb-II.

Physical Parameter	Symbol	Bi-III	Sb-II
Transition Temperature	T_c	7.05 ± 0.05 K	3.5 ± 0.1 K
Lower Critical Field	B_{c1}	15 ± 5 mT	13 ± 3 mT
Upper Critical Field	B_{c2}	2.5 ± 0.2 T	0.21 ± 0.03 T
Superconducting Coherence Length	l_ξ	11.4 ± 0.4 nm	39.6 ± 2.8 nm
Superconducting Penetration Depth	l_λ	108 ± 17 nm	113 ± 13 nm
Resistivity Gradient	ρ'	0.9 ± 0.15 $\mu\Omega$·cm/K	0.20 ± 0.05 $\mu\Omega$·cm/K
Plasma Frequency from DFT	Ω_p	3.5 ± 0.2 eV	n/a
Electron-Phason Coupling Constant from Calculated Plasma Frequency	λ_{DFT}	2.75 ± 0.7	n/a
Electron-Phason Coupling Constant from equation 4.15	λ_{exp}	2.70 ± 1.0	0.18 ± 0.06

Table 4.4 Comparison of physical properties between Bi-III and Sb-II. Data for Bi-III is taken from [27].

Finally, it is vital to calculate the electron-phonon coupling (the whole phonon spectrum range) using a different method. To do this, we know that the coherence length can be written as (refer to section 2.2.2)

$$\xi = \frac{\hbar v_F}{\pi \Delta} \tag{4.16}$$

Density functional theory predicts that Fermi velocity is renormalised by a factor of $(1+\lambda)$ in the presence of electron-phonon interaction [29]. We can compare our value to those in Bi-III to estimate the electron-phonon coupling constant. If we make an assumption that the original Fermi velocity in Bi-III and Sb-II are not much different (or in the same order of magnitude), we obtain

$$\frac{1+\lambda_{Sb}}{1+\lambda_{Bi}} = \frac{(T_c\xi)_{Bi}}{(T_c\xi)_{Sb}} \tag{4.17}$$

This equation gives $\lambda_{Sb} = 1.17$, which is totally reasonable. Note that this result does not disagree with the previous estimation of λ. We considered electrons scatter with phonon

at every frequency here, while we take into account for only low frequency phonon in our previous calculations.

4.3 Summary

We have studied two phases in antimony in this chapter - the low-pressure phase Sb-I and the incommensurate phase Sb-II. Although many studies in Sb-I are already available, we have extended the high-pressure work to the highest pressure achievable in the Sb-I phase before transforming into the Sb-II phase. The effect of pressure on the Sb-I is to enlarge the Fermi surface. The magnetoresistance measurement also confirmed this picture as it is suppressed strongly under pressure. The magnetoresistance shows strong quadratic dependence on an external magnetic field, especially at high pressure, confirming the validity of the two-band model. Quantum oscillation has been measured by the mean of resistivity measurement (Shubnikov - de Haas) with the field both parallel and perpendicular to the c-axis. The developments of quantum oscillation frequencies under pressure in both cases disagree with each other, meaning that the Fermi surface does not change in an isotropic manner.

In the Sb-II phase, we have done both resistivity and DC magnetisation measurements. The key results can be summarised as follows: (i) Sb-II exhibits type-II superconductivity (similar to Bi-III) at 3.5 ± 0.1 K. (ii) The low-temperature normal state power-law resistivity is $\rho \sim T^2$ (Fermi liquid-like) rather than linear resistivity (in contrast to Bi-III) (iii) The gradient $d\rho/dT$ in the linear regime of Sb-II (0.20 ± 0.05 $\mu\Omega$·cm/K) is much smaller than that in Bi-III (0.9 ± 0.15 $\mu\Omega$·cm/K). These results were translated into the electron-phason coupling constant, which turns out to be very small in Sb-II ($\sim$0.18), compared to Bi-III ($\sim$2.5). (iv) Anomalous first-order transition were observed at $\sim$250 K. All of the results above point toward the situation where the sliding mode (or phason mode) gets heavily pinned. It is not yet conclusive what causes the phason pinning. However, the first-order transition at high temperature suggests a structural phase transition. This has led us to speculation about the possibility of having Aubry's transition in this material. With this interpretation, we could explain all features observed in our experiment - quadratic resistivity at low temperature, the small gradient of resistivity in the linear regime, anomalous first-order transition at high temperature, and large residual resistivity. The more direct experiment such as low-temperature XRD is desirable to perform in the future, as it will confirm whether there is Aubry's transition happening in Sb-II or not.

Chapter 5

Studies of High-Pressure Phases of Ca_2RuO_4

5.1 Introduction and Literature Review

5.1.1 What is Perovskite, and why are they so interesting?

Prototypically, a material in the perovskite family is one with structure ABX_3, where A and B are cations, and X is an anion [154]. The perovskite family can be made more complex by inserting layers. The simplest layer structure is called the Ruddlesden-Popper phase (or RP phase), possessing structure $A_{n+1}B_nX_{3n+1}$ where $n > 1$. The non-layered perovskite can be recovered in the limit of $n \to \infty$. Perovskite materials give many exotic phenomena, including:

- High-temperature superconductor: many cuprate superconductors have a structure in the perovskite family. Some examples are $La_{2-x}Sr_xCuO_{4-\delta}$ [108] and $YBa_2Cu_3O_7$ [122, 160].
- Potential p-wave superconductor: There is speculation that superconductivity in strontium ruthenate Sr_2RuO_4 may be analogous to the He-3 A phase, and the pairing mechanism may be the chiral p-wave type [76].
- Ferroelectricity: many titanate materials exhibit ferroelectricity. Some example are $SrTiO_3$ [39] and $BaTiO_3$ [115].

- Colossal magnetoresistance: a very strong negative magnetoresistance (sometimes can be an order of magnitude), primarily found in manganate. Some examples are $La_{1-x}(Sr/Ca)_xMnO_3$ [146].

Although there are many different structures in the perovskites family, many of them have octahedra of oxygens with transition metal at the centre. Many features in the layer perovskites enrich their physics, giving rise to the phenomena mentioned above. The features worth mentioning are (i) quasi-two-dimensional nature, enhancing pairing energy and favour superconductivity [98]. (ii) Strong crystal field leads to lattice distortions, changing the electronic structure. (iii) A plane of alternating transition metals and oxygens leads to many possible exchange mechanisms, such as superexchange and double-exchange, resulting in various magnetic phases.

5.1.2 Introduction to Sr_2RuO_4

Since the discovery of the high-T_c cuprate superconductor in 1986 [17], numerous efforts have been made to understand the pairing mechanism and order parameters in these unconventional superconductors. Physicists continuously seek to find and study other systems that share similarities to cuprates to gain more hints on cuprate superconductors. In 1994, Y. Maeno discovered the new material Sr_2RuO_4, sharing the same crystal structure (figure 5.1) to cuprate, but without copper [166]. This discovery attracts so much attention to the condensed matter community, as it is very significant for fundamental studies related to cuprate. Sr_2RuO_4 has a superconducting ground state at 1.5 K, in contrast to its sister cuprates, where T_c is significantly higher by more than an order of magnitude.

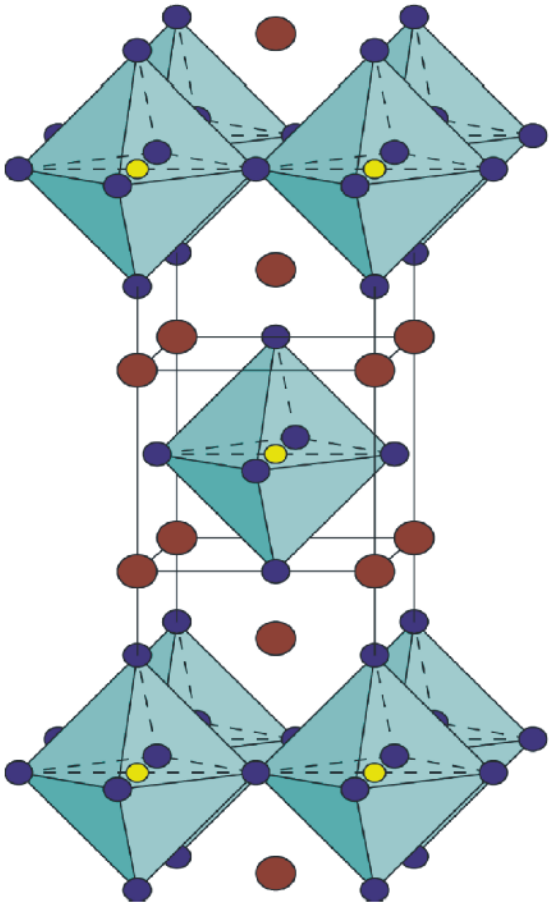

Fig. 5.1 The undistorted structure of strontium ruthenate Sr_2RuO_4 belongs to the I4/mmm space group with tetragonal structure. The brown, yellow and blue atoms are Sr, Ru and O, respectively. The figure was taken from [3].

The pairing mechanism in Sr_2RuO_4 can be elusive since we do not know its parent phase. On the other hand, the ground state of cuprates in the parent phase is usually antiferromagnetism, favouring the d-wave pairing. To access the parent phase of Sr_2RuO_4, we need to apply a negative pressure, which is not practical. However, it is certain that Sr_2RuO_4 is an unconventional superconductor [83] due to how sensitive T_c is toward the non-magnetic impurity level. Strontium ruthenate is one of the most important unconventional superconductors for the fundamental study because: (i) As the high-T_c nature in cuprates arises from the 2D nature of the copper-oxide plane, Sr_2RuO_4 was the first material that has the same structure as the lanthanum cuprate, but without copper. Thus, Sr_2RuO_4 can be used as a system to verify our understanding. (ii) It superconducts without doping, making Sr_2RuO_4 a very clean unconventional superconductor and suitable for definitive studies (such

as quantum oscillation to map out Fermi surfaces of this material). (iii) low T_c makes it possible to study normal state without any interference from phonon. Initially, Sr_2RuO_4 was believed to be a p-wave superconductor [120]. This thought stems from a few facts: (i) Its sister compounds $SrRuO_3$ has a ferromagnetic ground state [81]. (ii) Fermi liquid-like behaviour in the normal state with the mass enhancement, susceptibility enhancement, and Wilson ratio similar to He-3, leading to speculation that Sr_2RuO_4 is analogous to He-3 [10, 84]. However, there is not yet a conclusive result on the pairing symmetry. For instance, the observation of the shear elastic modulus suggests the order parameter to be of two-component [57]. Some literature also points out that there is a comparable tendency for both odd and even parity [85].

Strontium ruthenate Sr_2RuO_4 has $4d^4$ electronic configuration. The effect of the octahedral crystal field is to split the five-fold degenerate d-bands into three t_{2g} and two e_g levels[1]. All four d-electrons occupy t_{2g} bands, leaving e_g empty. The occupancy of each band is then $2/3$. Fermi surfaces of Sr_2RuO_4 comprises three sheets - α, β, and γ. The γ sheet, which derives from the d_{xy} orbit, is almost cylindrical. The cylindrical nature is evidence of being two-dimensional material. It is speculated that the γ sheet plays the dominant role [2, 76]. Ferromagnetic tendency comes from van Hove singularity on the γ sheet, whereas antiferromagnetic tendency comes from nesting between α and β with $Q = (2\pi/3, 2\pi/3, 0)$ [84].

The tendencies in both ferromagnetic and antiferromagnetic interactions can also be seen in the calculated Lindhard function. The peaks in this generalised susceptibility locate at $Q = (2\pi/3, 2\pi/3, 0)$ [52]. The existence of this peak and the van-Hove singularity at $(\pm\pi, 0), (0, \pm\pi)$ is an evidence of the competition between these two interactions.

[1] e_g states consist of d_{z^2} and $d_{x^2-y^2}$ whereas t_{2g} states consist of d_{xy}, d_{xz} and d_{yz}.

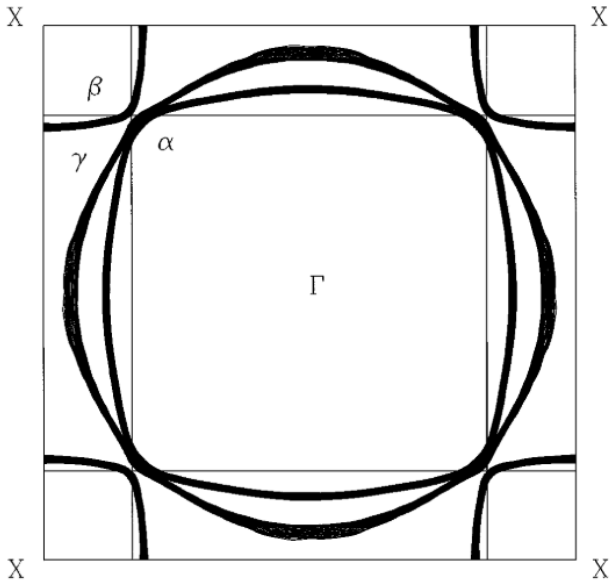

Fig. 5.2 Fermi surfaces of Sr_2RuO_4. Figure credit: [88]

More recent developments have suggested that the pairing mechanism in Sr_2RuO_4 should not be of the chiral p-wave, and many of them point towards even parity order parameter. Although it was found earlier that there is no change in the spin susceptibility by Knight shift measurement (from nuclear magnetic resonance of oxygen-17) in Sr_2RuO_4 (which is the main evidence for being a p-wave superconductor) [67], several experiments do not agree with this pairing mechanism. For instance, in a strained Sr_2RuO_4, the transition temperature is proportional to quadratic in strain, but no linear term is observed (which is expected in a chiral p-wave superconductor) [153]. Moreover, there is no edge current (which is supposed to be another signature of the $p_x + ip_y$ wave) observed in Sr_2RuO_4 [64]. The latest measurements of Knight shift (using nuclear magnetic resonance of oxygen-17) in strained Sr_2RuO_4 show a drop in spin susceptibility at all values of strain, contradicting with the previous NMR measurements [116].

5.1.3 Introduction to Ca_2RuO_4

Calcium, being an element above strontium in the periodic table and having the same electronic configuration, can replace strontium atoms in Sr_2RuO_4 and obtain Ca_2RuO_4 instead. In the case of this material, it introduces flattening, rotation, and tilt in the RuO_6 octahedra. We can therefore regard Ca_2RuO_4 to be a distorted version of Sr_2RuO_4. The roles of these distortions are: (i) Flattening - remove the degeneracy further. (ii) Tilt and rotation -

change the angle of the Ru-O bonds, reducing the bandwidth. The structure of Ca_2RuO_4 is orthorhombic with the S-Pbca[2] space group at ambient pressure and room temperature. The calcium ruthenate structure is susceptible to external pressure and temperature. It undergoes a series of structural phase transitions once pressure is applied. Firstly, in the S-Pbca structure, the Ru-O octahedra are tilted and rotated (as shown in figure 5.3). In this phase, the calcium ruthenate is canted antiferromagnetic insulator. Once an external pressure of 5 kbar is applied, it undergoes first-order structural transition towards the L-Pbca[3] structure and starts to lose the tilt. In contrast to the S-Pbca phase, the L-Pbca phase is associated with itinerant ferromagnetism. At the pressure of 70 kbar, the tilt completely disappears, whereas the rotation remains. This phase is described by the space group Bbcm [135]. The phase diagram of Ca_2RuO_4 is shown in figure 5.5.

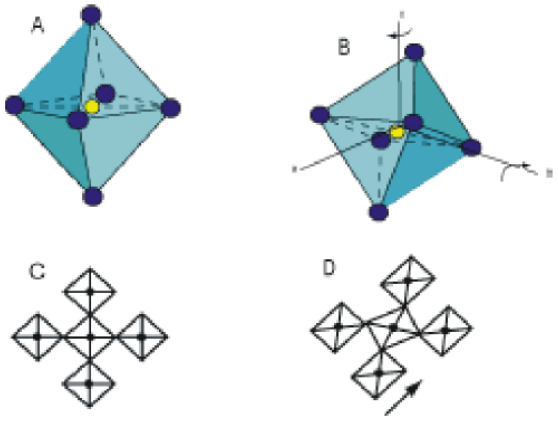

Fig. 5.3 The tilt and rotation in Ru-O octrahedra that happens in the S-Pbca phase of Ca_2RuO_4. (A) shows the undistorted strucutre of the Ru-O octrahedron. (B) shows distorted structure of the Ru-O octrahedron. (C) shows the top view of the undistorted structure. (D) shows the top view of the distorted structure. The figure was taken from [3].

[2]S stands for short, as the c-axis is shorter than that in the undistorted tetragonal structure.
[3]L stands for long, as the c-axis is longer than that in the undistorted tetragonal structure.

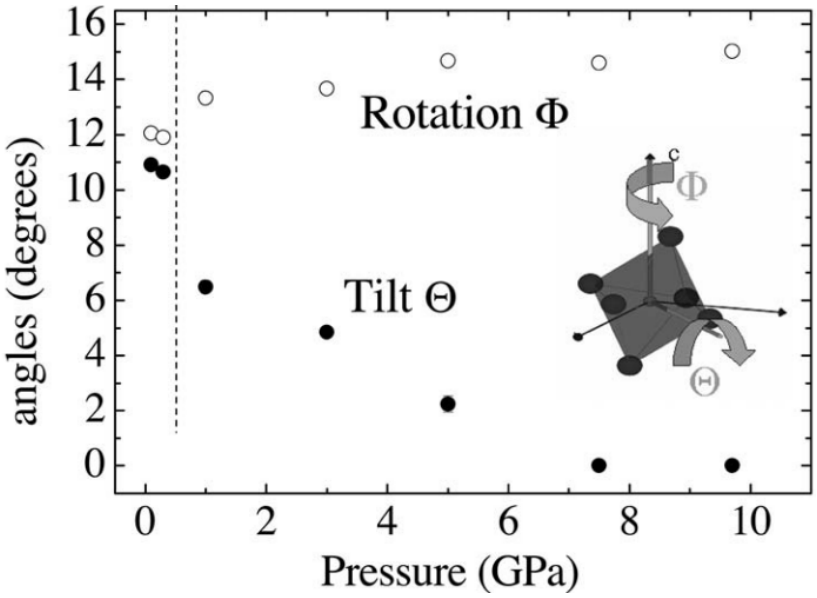

Fig. 5.4 The rotation and tilt as a function of pressure. The figure was taken from [135].

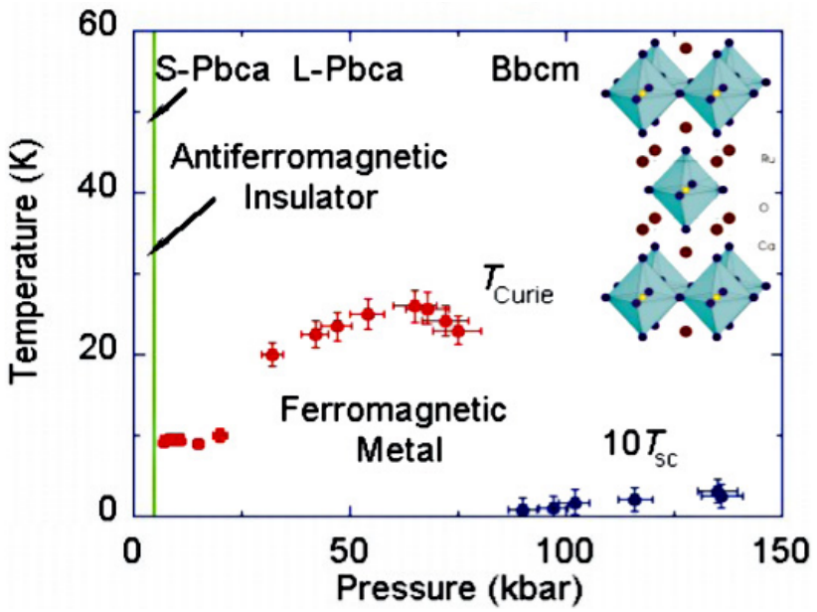

Fig. 5.5 The phase diagram of Ca_2RuO_4. The figure was taken from [4].

We begin with some brief reviews of the S-Pbca phase. Since the electronic structure of calcium ruthenate comes from the $4d^4$ electrons from the ruthenate atoms, which live in octahedral cages of oxygen, the crystal field is important. As in Sr_2RuO_4, the d-orbital splits into two-fold degenerate e_g states and three-fold degenerate t_{2g} states with the octahedral

environment. However, the octahedral gets flatten in the S-Pbca phase, resulting in further splitting and pushing the d_{xy} orbital down while pushing the d_{xz} and d_{yz} orbitals up. The distortion of the octahedral is preferred since it lowers the electronic energy. This effect is known as the Jahn-Teller effect. As there are four conduction electrons, this filled the d_{xy} bands while half-filled the d_{xz} and d_{yz} bands [138]. The existence of the unfilled bands in the calcium rutherate (despite the insulating behaviour) suggests that this is a Mott insulator. The measured Mott gap from the transport measurement is approximately 0.4 eV [103]. The insulating behaviour was also confirmed in the low-temperature heat capacity measurement [**?**]. The neutron scattering measurement confirms the antiferromagnetic ordering with Neel temperature $T_N = 110$ K, with the easy axis on a or b direction [22]. A few ways to induce the metal-insulator transition in this phase are temperature, pressure, and electric field. For temperature and pressure, it induced the MI transition once the material is heated above 357 K at ambient pressure or five kbar at room temperature [105]. This transition accommodates the structural transition from S-Pbca to L-Pbca. For the electric field-induced MI transition, the threshold field is 40 V/cm, much smaller than the Mott gap [102]. Moreover, it has been observed that a magnetic field of 9 T at 5 K can also cause a jump in magnetic susceptibility, making it similar to metamagnetic transition [79].

In the L-Pbca phase, the material becomes itinerant ferromagnetic. The evidence for the metallic phase is the drastic drop in resistivity by orders of magnitude (figure 5.6) [101]. In this paper, the hysteresis in the DC magnetisation of the sample was also observed, which is the signature of ferromagnetic phase. At 50 kbar, the remnant magnetisation gives the maximum value in the a-direction (hence suggesting a-axis to be an easy direction), approximately $0.4\mu_B$ per Ru ion. This value is smaller than the saturated moment of $2\mu_B$ in the localised Ru ion, suggesting the itinerant nature. The antiferromagnetic phase persists at pressure well above 5 kbar, and the sample is in a mixture state between antiferromagnetic and ferromagnetic. The evidence of this is the Raman scattering measurement from [133], showing the two-magnon peak persists even at the pressure above Mott transition.

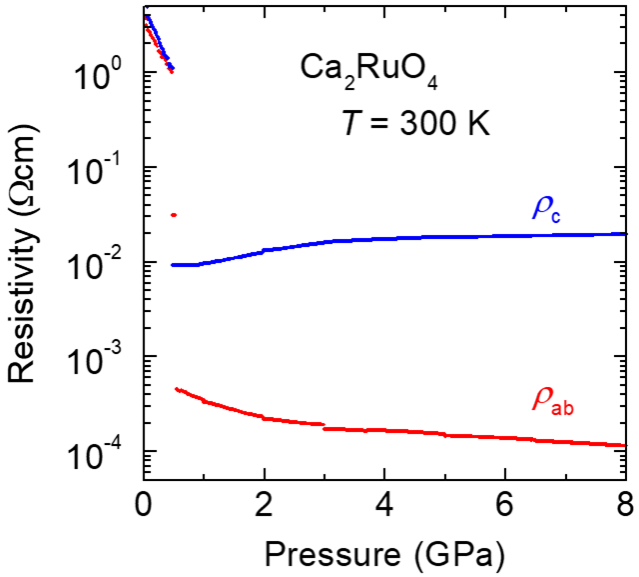

Fig. 5.6 Resistivity of Ca_2RuO_4 as a function of pressure. The figure was taken from [101].

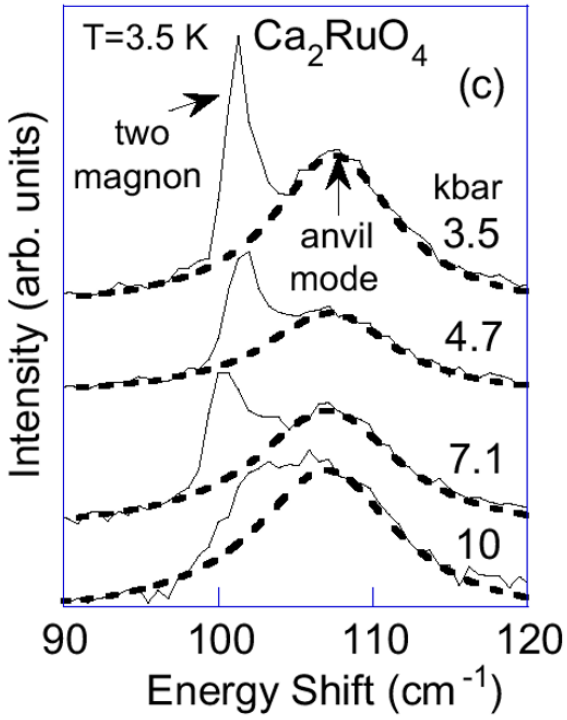

Fig. 5.7 The raman scattering in Ca_2RuO_4 showing the two-magnon mode. The figure was taken from [133].

Finally, ferromagnetic transition suddenly disappeared at a pressure above 80 kbar[4] and superconductivity was observed by quasi four-point measurement above 90 kbar [4]. The superconducting transition temperature is 100 mK at 90 kbar, and it rises to 400 mK at 140 kbar.

Doped $Ca_{2-x}Sr_xRuO_4$

One important tuning parameter of this is the isoelectronic doping in Ca_2RuO_4 by strontium. The study was performed in the range of $x \in [0, 0.7]$ [105]. Figure 5.8 shows the phase diagram of the Sr-doped in Ca_2RuO_4. The effect of the isovalence doping is to tune the bandwidth and the band filling factor (since it changes the relative energy of each band).

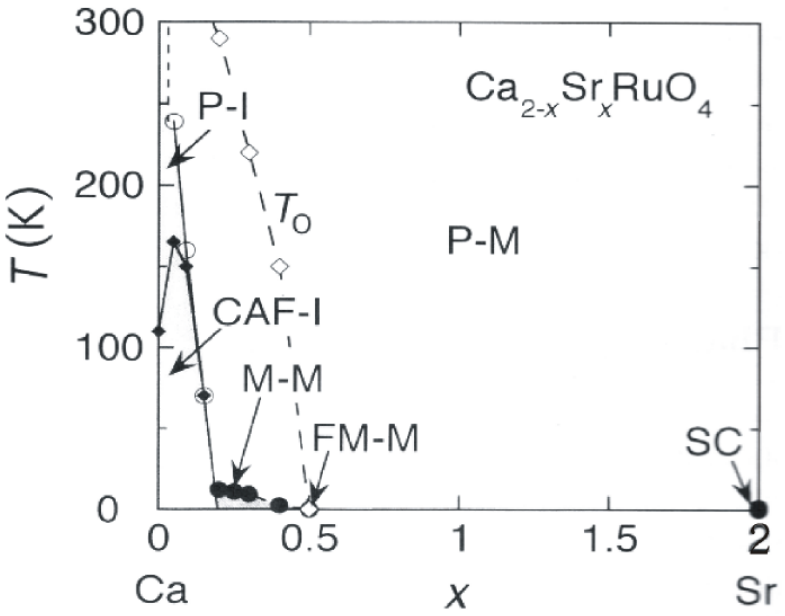

Fig. 5.8 Phase diagram of Sr-doped in Ca_2RuO_4. Figure credit [105]

At $x < 0.2$, the system is antiferromagnetic insulating, as is expected for Ca_2RuO_4. Beyond this point where $0.2 < x < 0.5$, the system undergoes insulator-metal transition. At the low-concentration side ($x = 0.2$), the system shows antiferromagnetic correlation, and crossed over to ferromagnetic correlation at the high-concentration end ($x = 0.5$). Power-law studies have been carried out, and non-Fermi liquid was observed [105]. The low-temperature resistivity follows the form $\rho = \rho_0 + AT^{1.4}$, which is a signature of two-dimensional ferromagnetic

[4]Private communication with Dr Patricia Alireza.

spin fluctuation (where the power-law exponent is 4/3), according to the self-consistence one-loop theory [100]. Above $x > 0.5$, the system becomes paramagnetic metallic. In this region, the tilt of the RuO_6 octahedra is removed completely, but the rotation remains.

5.2 Results and Discussions

This project results from collaborations between Puthipong Worasaran, Dr Patricia Alireza, Dr Jiasheng Chen, and Prof Gil Lonzarich. PW and PLA set up two resistivity pressure cells for Ca_2RuO_4 (PLA helps with the sample preparation, and PW helps with the pressure cell preparation). The measurements were done by PW in PPMS, and by JC in the DMS system. GL helps to provide many valuable discussions.

5.2.1 Experimental Detail

The resistivity measurement was performed using the standard 4-point measurement technique. Making contacts on this material proved to be extremely difficult. Firstly, we have to be very careful on the position of the contact placement due to the huge anisotropy in the sample (the resistivity in the c-axis is three orders of magnitude larger than in the ab-plane). We must place current wires at the sides of the sample while voltage wires on top (ab-plane). As a result, this type of contact geometry makes it a lot more difficult than placing contacts at the corners due to the limitation in working space. Secondly, the silver epoxy we use must be the kind that cures at low temperatures because Ca_2RuO_4 has the structural transition at above 357 K (or 84 C) that is likely to introduce a crack in a sample - Dupont silver paste 6838 is not an option here. The silver epoxy we used to make contacts is the two-part silver epoxy for circuits that cures at 60 C for one hour. This epoxy is extremely runny (compare to 6838, where it is rather sticky), hence makes it hard to place four 10 microns gold wires on 180 microns samples. We have set up two pressure cells for this project for the reason we will explain later. Both pressure cells are set up in the same way. Moissanites were used for the anvils. The culet size is 0.8 mm, and an insulating gasket was used. The first sample dimension is $180 \times 100 \times 40\ \mu m^3$, the second sample dimension is $200 \times 100 \times 40\ \mu m^3$, and the third sample dimension is $100 \times 80 \times 40\ \mu m^3$. The resistivity was calculated directly from the formula $R = \rho l/A$.

5.2.2 Ferromagnetic Ground State Phase

Resistivity Measurement

We start by investigating the itinerant ferromagnetic phase. Figure 5.9 shows the resistivity measurement of Ca_2RuO_4 at 48 kbar. The measurement gives RRR to be approximately 100, indicating a very high-quality sample. The residual resistivity is less than 1 $\mu\Omega$·cm, very promising to observe two interesting aspects (i) quantum oscillatory effect, and (ii) the possibility of a first-order transition. However, we will see later that it is impossible to observe the Shubnikov - de Haas quantum oscillation due to the strong negative magnetoresistance (as the oscillation signal would be smaller than noise). A possible way to measure the quantum oscillation of this FM phase is to do via the de Haas - van Alphen. There was already a study measuring AC susceptibility using a micro coil in pressure cells [58]. However, the study is not yet conclusive - the study using the tunnel diode oscillator technique is desirable due to its great sensitivity.

There are a few exciting features in this graph. Firstly, there is a shoulder at roughly 20 K. Secondly, the flattening resistivity curve at low temperature. Thirdly, the superlinear power law above the transition. We will go through these features in more detail.

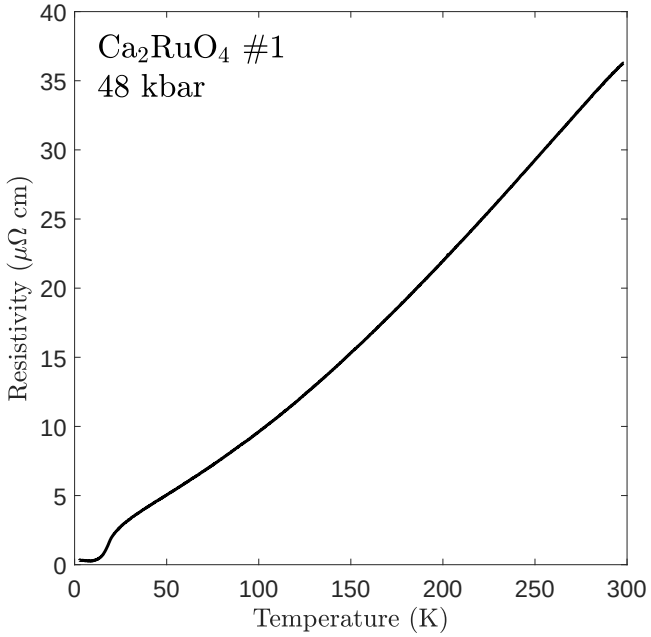

Fig. 5.9 Resistivity profile in Ca_2RuO_4 at 48 kbar in sample 1. The temperature range is between 2 K and room temperature. The measurement was done in the PPMS. The cooling rate for the whole temperature sweep is 0.3 K/min.

Starting with the shoulder at around 20 K, this is a sign of a phase transition. According to previous works in AC susceptibility and SQUID measurements, we can infer that the shoulder arises from paramagnetic-ferromagnetic transition. Figure 5.10 shows resistivity at low temperature for a clear picture of this shoulder. We perform derivative in the resistivity to see how sharp the transition is, showing in Figure 5.11. The width of the peak in the differential resistivity is remarkably broad. There are a few possible explanations for the broad transition: (i) inhomogeneity in a liquid medium; however, it should not be the case in our system as glycerol has an excellent hydrostatic condition up to $\sim$50 kbar. (ii) the cooling/warming rate is too fast; to test this possibility, we perform a very slow sweep rate of 0.02 K/min in a different pressure cell (Figures 5.12 and 5.13). The nature of the observed transition did not change with a slow temperature sweep rate. (iii) the transition is first-order (as it is observed in many clean system at low temperature - The first-order transition is due to the interaction between magnetic fluctuation and electronic soft mode [19]); we have checked very carefully by comparing warmup data and cooldown data at 0.02 K/min (figure 5.14). However, there is no visible hysteresis. It is unlikely that the broad transition is connected to first-order transition (also see later section in AC susceptibility measurement). Although we have ruled out some possibilities, we still cannon explain this mysterious broad transition nature.

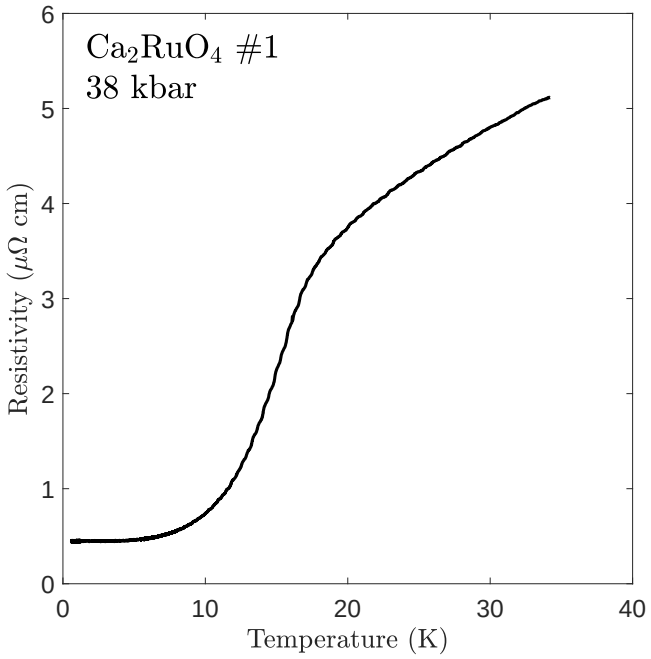

Fig. 5.10 Low temperature resistivity in Ca_2RuO_4 at 38 kbar in sample 1, showing shoulder at the ferromagnetic transition. The measurement was done in the commercial DMS. The cooling rate is 0.3 K/min

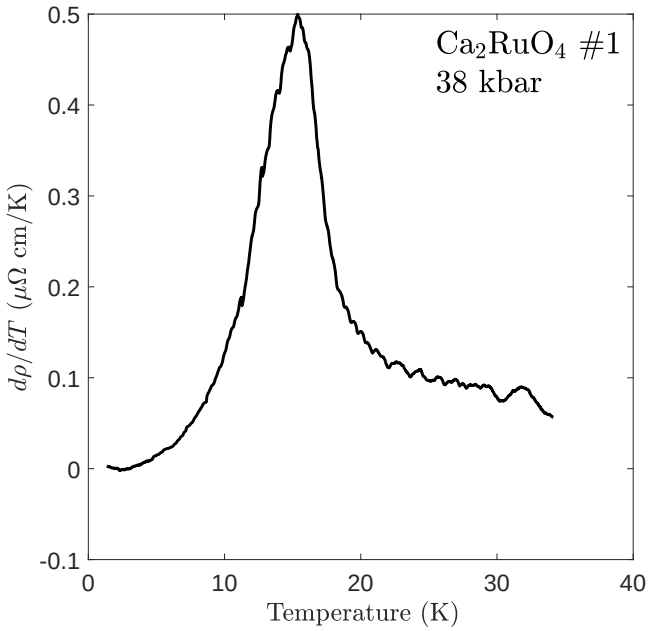

Fig. 5.11 Differential resistivity of Ca_2RuO_4 at 38 kbar in sample 1. The measurement was done in the commercial DMS. The cooling rate is 0.3 K/min

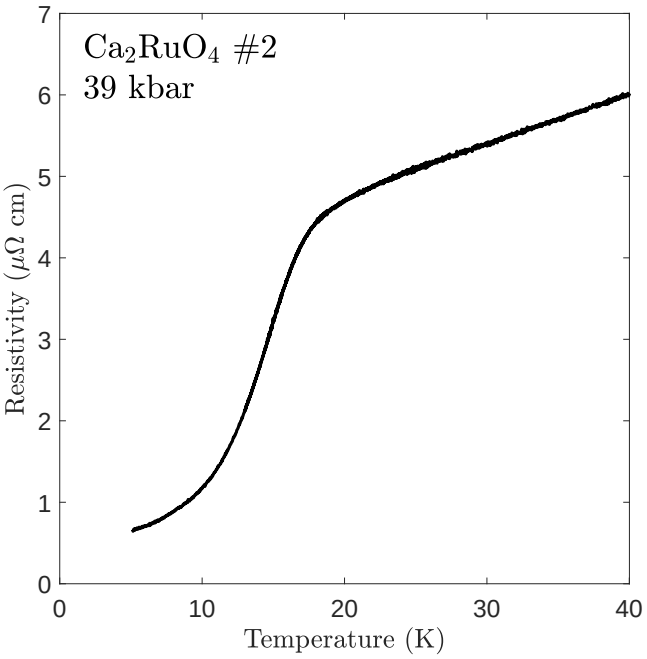

Fig. 5.12 Low temperature resistivity in Ca_2RuO_4 at 39 kbar in sample 2, showing shoulder at the ferromagnetic transition. The measurement was done in the PPMS. The cooling rate is 0.02 K/min

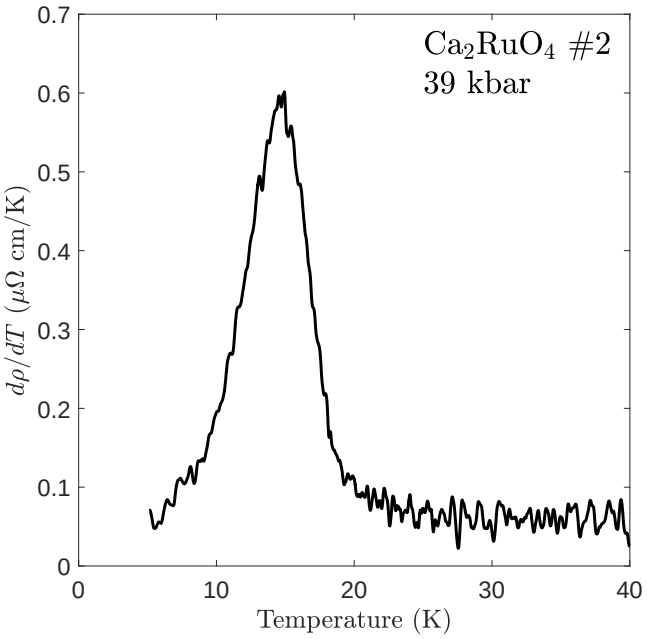

Fig. 5.13 Differential resistivity of Ca_2RuO_4 at 39 kbar in sample 2. The measurement was done in the PPMS. The cooling rate is 0.02 K/min

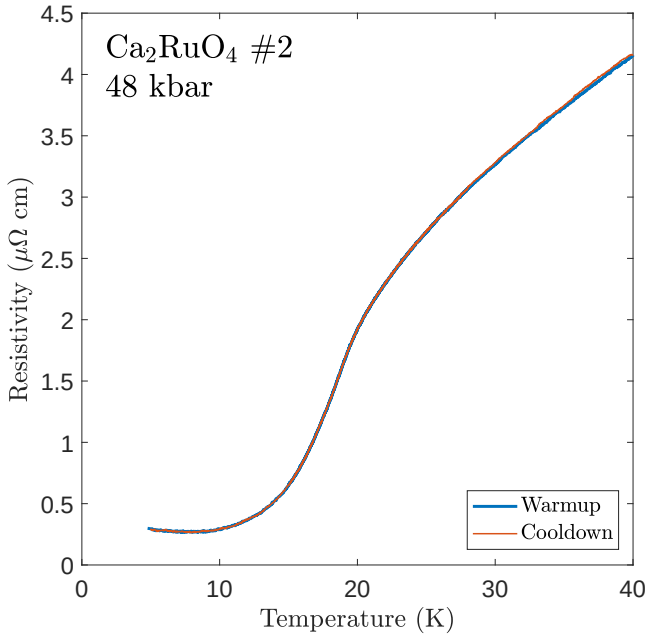

Fig. 5.14 Comparing slow warmup and cooldown through the transition of Ca_2RuO_4 at 48 kbar in sample 1. The measurement was done in the PPMS with the rate of 0.02 K/min.

Next, we study the form of resistivity at the base temperature. It is clear in figure 5.10 that the resistivity is very flat at low temperatures. By fitting the curve to the simplest power law equation $\rho = \rho_0 + AT^n$, one finds $n \sim 4.3$. It may be tempting to view this as the usual low-temperature electron-phonon scattering $\rho \sim T^5$. However, the existence of a shoulder at below 20 K suggests that the resistivity flattening may come from the electron-spin wave scattering instead. Any anisotropy introduces an energy gap in the magnetic spectrum. Hence, the low-temperature resistivity should follow exponential function instead of power-law. The form of resistivity with the strong uniaxial anisotropy reads [6, 55]

$$\rho = \rho_0 + AT^2 + BT\Delta\left[1 + \frac{2T}{\Delta}\right]e^{-(\Delta/T)} \tag{5.1}$$

In this equation, the first term represents the residual resistivity, the second term represents the usual Fermi liquid term, and the third term represents scattering between electron and gapped magnetic fluctuation. The energy gap in magnetic fluctuation comes from anisotropies, which destroys the gapless Goldstone mode. Anisotropy can arise from many things, such as crystal structure and spin-orbit coupling. The form of resistivity above is correct for the ferromagnetic magnon in strong uniaxial anisotropy. The exponential of the energy gap can be understood roughly from the Boltzmann factor. Since magnetic fluctuations get frozen out

at a low enough temperature, the exponential term does not contribute to the resistivity at this temperature. However, at high temperatures, the scattering with magnetic fluctuation overcomes electron-electron interaction, giving rise to the rapid increase in resistivity. We fit the resistivity graph to this function, as shown in figure 5.15. The fitting parameter are the following: $\rho_0 = 0.436$ $\mu\Omega$·cm, $A = 0.0113$ $\mu\Omega$·cm/K^2, $B = 0.0308$ $\mu\Omega$·cm/K^2, and $\Delta = 47.1$ K. From the fit, we see that the resistivity follows equation 5.1 very well, suggesting gapped ferromagnetic ground state.

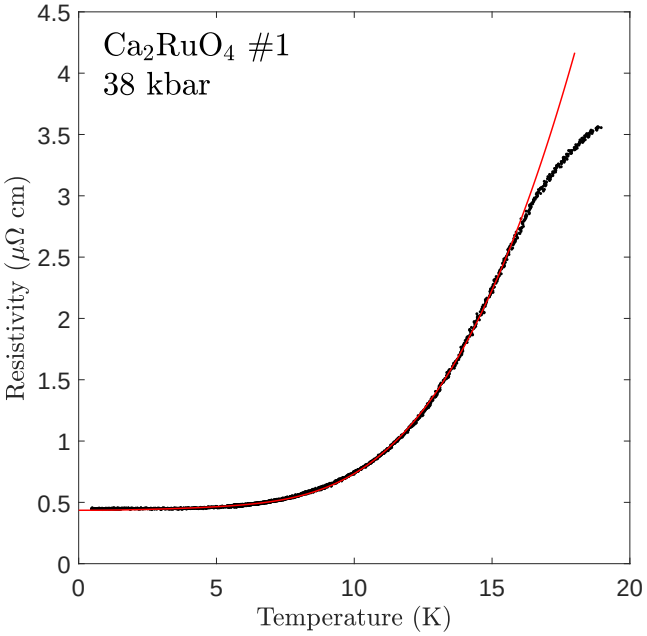

Fig. 5.15 Resistivity in Ca_2RuO_4 at 48 kbar in sample 1. The fit to the equation 5.1. The fitting parameters are $\rho_0 = 0.436$ $\mu\Omega$·cm, $A = 0.0113$ $\mu\Omega$·cm/K^2, $B = 0.0308$ $\mu\Omega$·cm/K^2, and $\Delta = 47.1$ K. The red line is a guide to the eye.

Next, we discuss the high-temperature power law. By plotting resistivity versus $T^{4/3}$, the curve is highly linear, suggesting that resistivity is proportional to $T^{4/3}$, or at least close to this function. The plot of resistivity versus $T^{4/3}$ is shown in figure 5.16. We investigate power-law more carefully by the direct fitting. The candidate function for this high-temperature regime resistivity is

$$\rho = \rho_0 + BT^n \tag{5.2}$$

However, as we know that there should be a contribution from electron-phonon scattering at high temperature, we can add that term by hand, and the resistivity becomes

$$\rho = \rho_0 + AT + BT^n \tag{5.3}$$

We have fitted the curve using the two equations above. Both equations fit well to the resistivity data, with slight differences in the power law. Figure 5.17 shows the fit without the electron-phonon contribution, and figure 5.18 shows the fit with the electron-phonon contribution. The values of the power-law obtained from these fits are $n = 1.41$ and $n = 1.43$ for the one without and with phonon, respectively. There is only a small change when excluding the phonon scattering from our power-law fitting. The power law of 1.43 may be explained by the self-consistent renormalisation theory in 2D itinerant ferromagnetic (the description is given in chapter 2). Since Ca_2RuO_4 is expected to be quasi-2D itinerant ferromagnetic (the fact that the material is quasi-2D is also suggested by the fact that resistivity in c-direction is ~ 1000 times larger than resistivity in ab-plane at room temperature), it is reasonable to see that the exponent in resistivity, $n \sim 1.4$, is close to the value predicted by SCR theory, $n = 1.33$. The deviation may be because it is not perfectly two-dimensional.

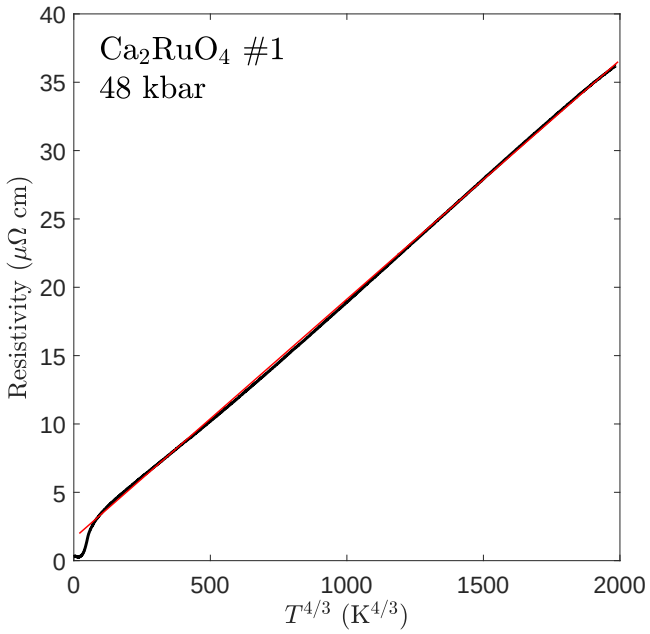

Fig. 5.16 Resistivity versus $T^{4/3}$ in Ca_2RuO_4 at 48 kbar in sample 1. The red line is the linear fit and is the guide to the eye.

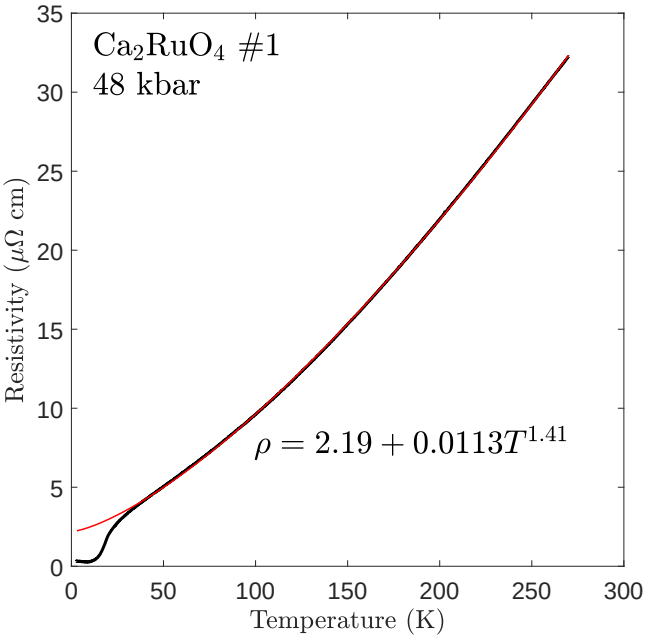

Fig. 5.17 Resistivity in Ca_2RuO_4 at 48 kbar in sample 1. The fit to the equation 5.2, which excludes the phonon contribution. The power law is $n = 1.41$. The full equation reads $\rho = 2.19 + 0.0113 \times T^{1.41}$ $\mu\Omega$·cm. The red line is a guide to the eye.

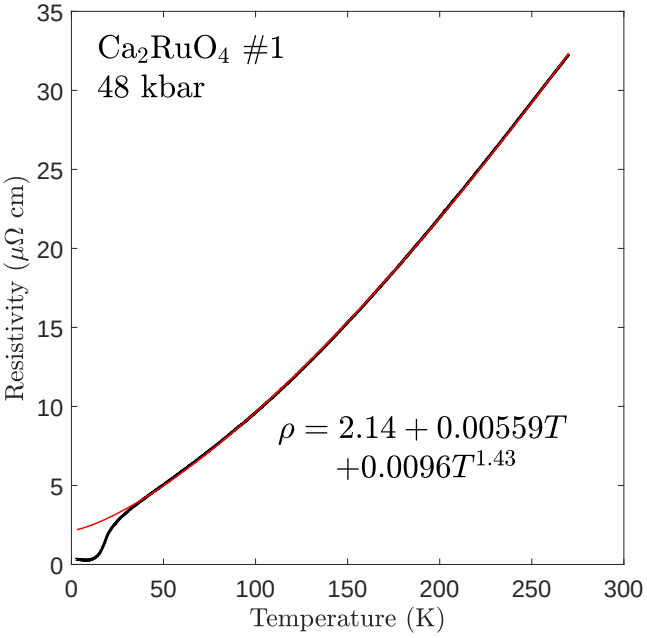

Fig. 5.18 Resistivity in Ca_2RuO_4 at 48 kbar in sample 1. The fit to the equation 5.2, which includes the phonon contribution. The power law is $n = 1.43$. The full equation reads $\rho = 2.14 + 0.00559 \times T + 0.00960 \times T^{1.43}$ $\mu\Omega$·cm. The red line is a guide to the eye.

Problem with Contacts Placement in Magnetoresistivity Measurement

Before we move to magnetoresistance measurement in ferromagnetic Ca_2RuO_4, we start by discussing a problem we have encountered in measuring magnetoresistivity. When we measured the magnetoresistance in sample 1 at 48 kbar, we observed a negative resistance. The data is shown in figure 5.19.

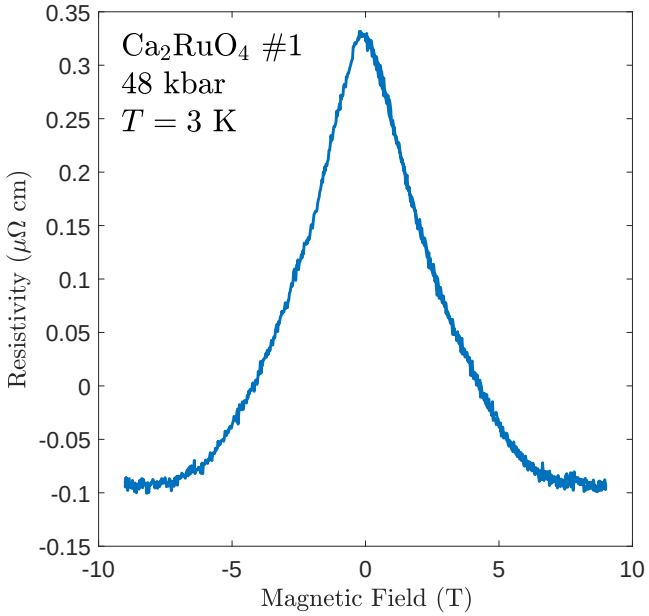

Fig. 5.19 Negative absolute resistivity of Ca_2RuO_4 sample 1 at 48 kbar in field. The temperature is 3 K.

Since this problem is significant and may relate to the reliability of all the previous measurements so far, it must be explained how it happens. We attempt to explain this negative resistance: this negative resistance may arise when two things happen simultaneously.

1. The contact geometry is not a perfectly straight line, but they are in the zigzag geometry.
2. The material exhibits very strong negative magnetoresistance when the field is in the c-axis.

When this happens, there are a few ways to observe negative resistance. Simple examples are: (i) resistivity in *a* and *b* directions respond to magnetic field differently. (ii) the sample orientation is slightly tilted and it has some magnetic field component in the *ab*-plane. If we measure voltage not exactly parallel to the current, these anisotropies can change the polarity of the signal.

Note that since the magnetoresistivity is symmetric in switching the field polarity, the Hall effect can be ruled out.

Magnetoresistivity

We have set up another pressure cell to study magnetoresistivity properly to ensure that: (i) All four contacts are as colinear as possible. (ii) Two voltage terminals are on the plane only and not touching the side (as this will cause picking up signal arising from c-direction, which is particularly bad for material with large anisotropy like this one - further discussion in [155]). (iii) Two currents terminals cover the side of the sample very well to make sure uniform current flow.

Remeasuring magnetoresistivity in the new pressure cell, we obtained a much more reasonable result. The magnetoresistivity at 2.5 K in sample 2 at 39 kbar is shown in figure 5.20.

The magnetoresistivity at different temperatures is shown in figure 5.21. The strong negative magnetoresistance is observed in the ferromagnetic phase (below $\sim$20 K) and the paramagnetic phase (above $\sim$20 K). At the lowest temperature of 2.5 K, the resistance drops by a factor of 4 in the magnetic field of 9 T. Usually, the origin of the negative magnetoresistance in ferromagnetic relates to the scattering of electrons with magnetic fluctuations [163]. However, with this very strong negative magnetoresistance, we may classify it as colossal magnetoresistance, similar to the case of manganite. The origin of the colossal magnetoresistance can be very complicated and vary from system to system [145]. We do not yet understand what causes the colossal magnetoresistance in this ferromagnetic phase. Next, we present the fractional change in magnetoresistance, defined by

$$\%\Delta\rho = \frac{\rho(T,B) - \rho(T,0)}{\rho(T,0)} \tag{5.4}$$

For the sake of clarity, we plot the graphs separately; one in the ferromagnetic phase and one in the paramagnetic phase. Figure 5.22 shows the percentage magnetoresistance in the ferromagnetic phase, while figure 5.23 shows the percentage magnetoresistance in the paramagnetic phase. It is surprising to see that $\%\Delta\rho$ in the ferromagnetic phase is very much temperature-independent.

Finally, we measure the temperature-dependent of resistivity in the field (figure 5.24). This suppression of the shoulder is similar to the colossal magnetoresistance. By subtracting resistivity with field to resistivity without field, we observe a dip in data which can be

interpreted as the Curie temperature. By extracting the transition temperature this way, we obtain $T_c = 17.5$ K.

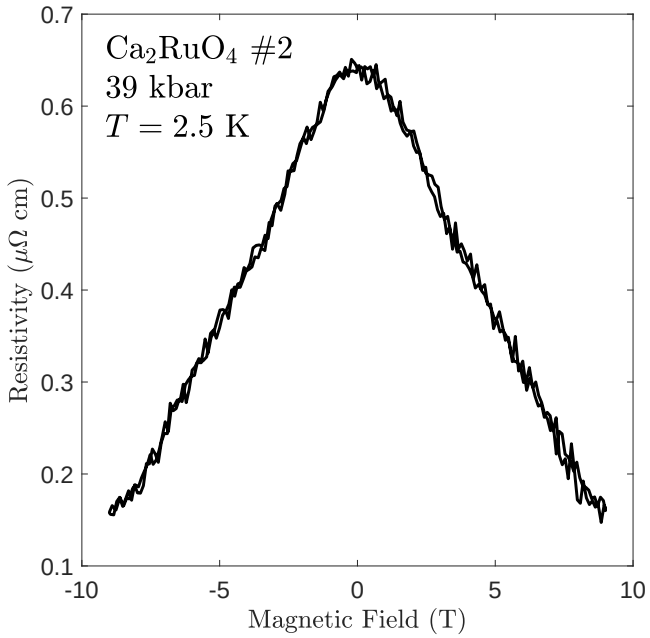

Fig. 5.20 Magnetoresistivity of Ca_2RuO_4 sample 2 at 39 kbar. The temperature is 2.5 K.

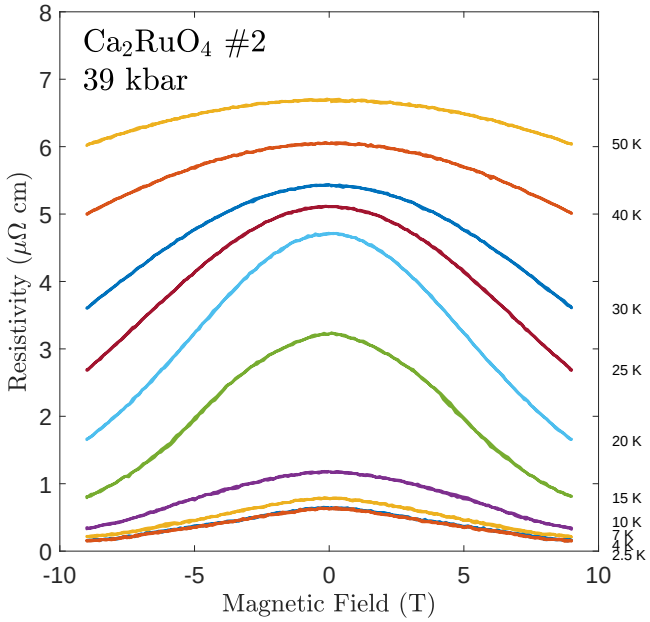

Fig. 5.21 Magnetoresistivity of Ca_2RuO_4 sample 2 at 39 kbar. The temperature range is between 2.5 K to 50 K.

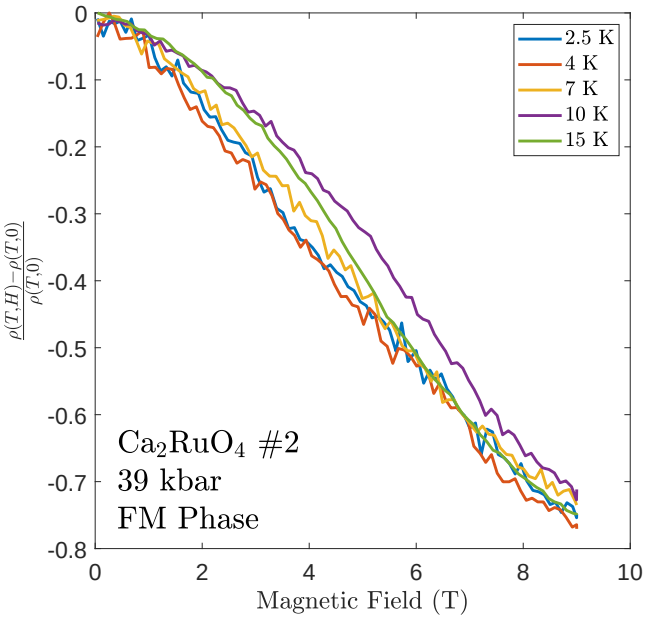

Fig. 5.22 Magnetoresistivity (percentage) in ferromagnetic phase of Ca_2RuO_4 sample 2 at 39 kbar.

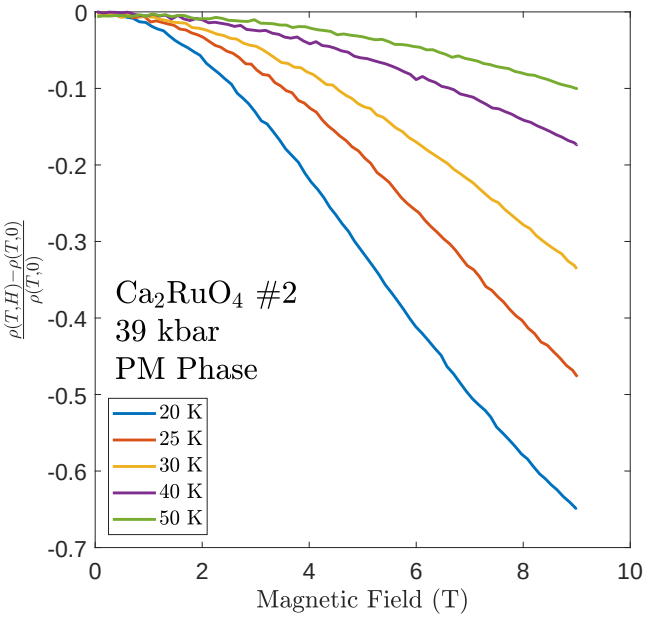

Fig. 5.23 Magnetoresistivity (percentage) in paramagnetic phase of Ca_2RuO_4 sample 2 at 39 kbar.

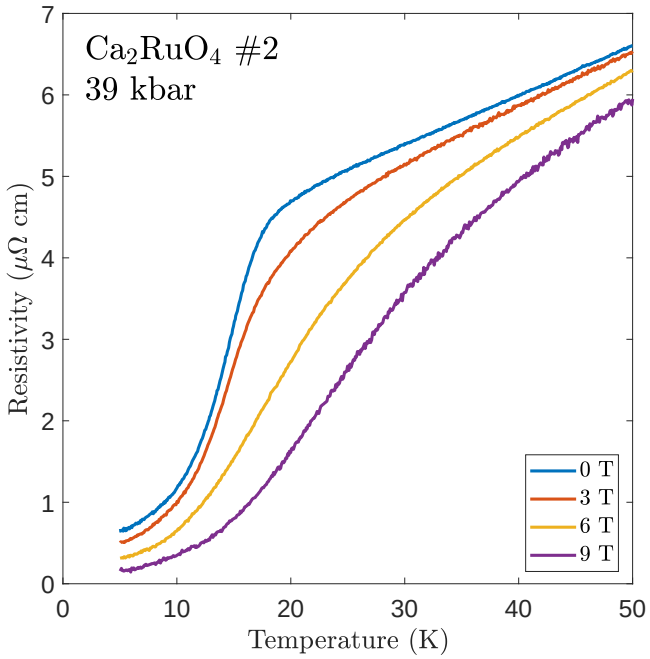

Fig. 5.24 Resistivity versus temperature of Ca_2RuO_4 sample 2 at 39 kbar with the applied magnetic field of 0 T, 3 T, 6 T and 9 T.

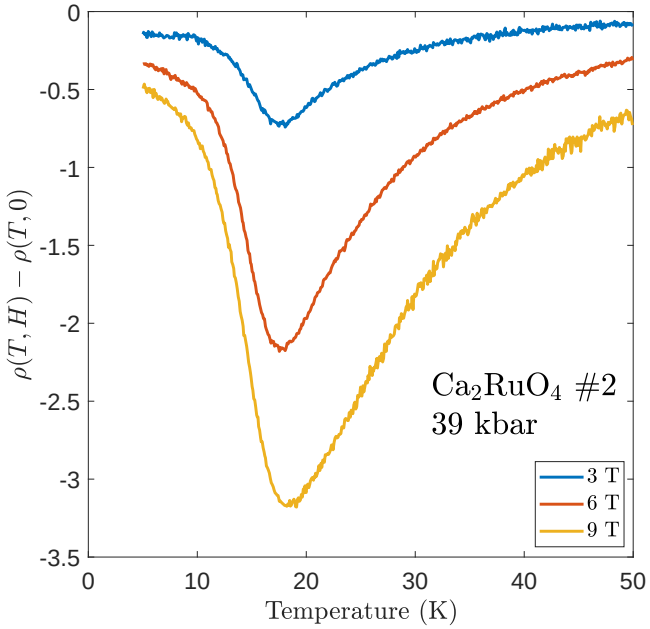

Fig. 5.25 The difference between resistivity with and without field versus temperature of Ca_2RuO_4 sample 2 at 39 kbar.

Magnetic Susceptibility

Apart from the resistivity measurements, we have also performed the susceptibility measurement in the ferromagnetic phase to explore the possibility of having a first-order phase transition. Dr Patricia Alireza kindly set up the pressure cell used in this section.

The measurements were done in the Coldhead (4K measurement system). Pre-amplifier and transformer (10X) were used to get a better signal-to-noise ratio. The frequency used is 777 Hz, and the phase of the lock-in amplifier is set to 90 degrees. The current for the drive coil is 8 mA.

Figures 5.26 and 5.27 show AC susceptibility data in Ca_2RuO_4 at 38 kbar and 79^{+5}_{-4} kbar, respectively. Before the measurement, pressure read 84 kbar while it dropped to 75 kbar after the measurement. The peak in the susceptibility of the 79 kbar measurements is at a higher temperature than that of 38 kbar. However, the peak does not represent the Curie temperature directly. To find the Curie temperature T_c, one needs to fit the data in the paramagnetic phase to the equation $\chi \propto (T - T_c)^{-1}$. Since our signal from the sample is combined with the enormous background (we need to use an extremely small sample), we cannot simply do this fit well. The divergence in magnetic susceptibility is concrete evidence for the second-order transition nature, meaning that the FM-PM transition is second-order up to at least 79 kbar.

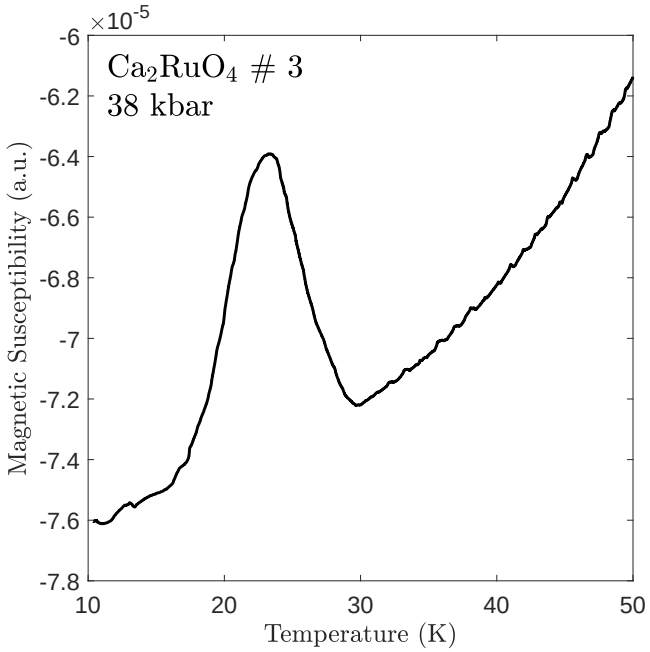

Fig. 5.26 The X-component of AC susceptibility of Ca_2RuO_4 at 38 kbar.

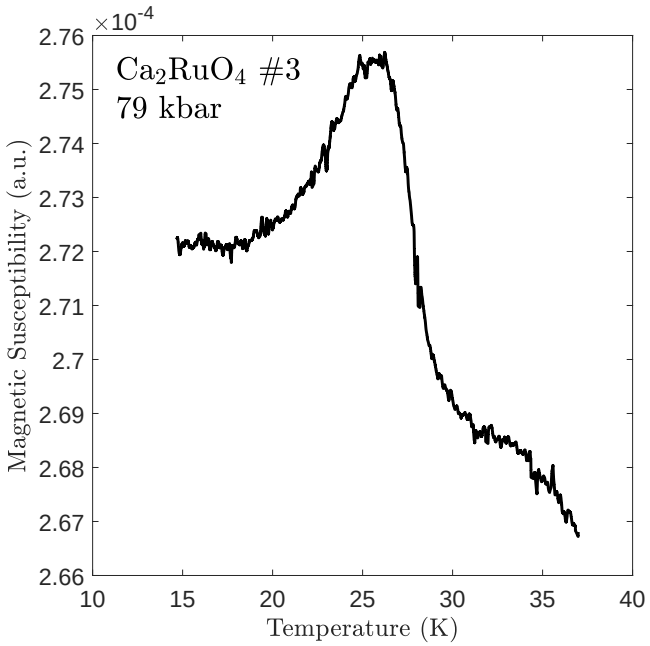

Fig. 5.27 The X-component of AC susceptibility of Ca_2RuO_4 at 79^{+5}_{-4} kbar.

There are two possibilities that we did not observe the FM-PM transition to be first-order: (i) the disorder strength is too high, suppressing tricritical temperature to zero Kelvin [19]. (ii) transition temperature is too high, suppressing electronic soft mode that induced the first-order transition. To pursue this, we have to suppress the curie temperature by applying more pressure.

5.2.3 Superconducting Ground State Phase

To have a hint of what phase diagram looks like, we decided to investigate in the region far from ferromagnetism. Transport measurement at 108 kbar was conducted in this study. Figure 5.28 shows the resistivity measurement from room temperature down to 3 K. The most interesting feature in this plot is the linear resistivity at high temperature. The linear resistivity $\rho \sim T$ differs drastically from the one above the FM phase, $\rho \sim T^{4/3}$. There are two ways to interpret this result: (i) electron-phonon scattering - however, it is unlikely to be the case because of the existence of the shoulder at less than 50 K. For a pure electron-phonon scattering, the resistivity usually goes smoothly from $\rho \sim T^5$ to $\rho \sim T^2$ and $\rho \sim T$ as temperature increases. (ii) electrons scatter with magnetic fluctuation. This could be 2D antiferromagnetic fluctuation or a spin-texture state. The scattering with magnetic

fluctuation is a more plausible scenario because of the shoulder in the resistivity curve. We will investigate the ground state carefully next.

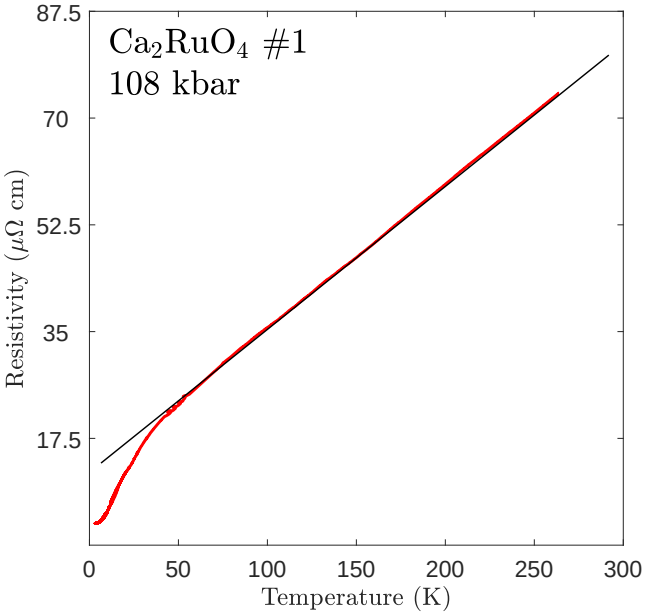

Fig. 5.28 Resistivity measurement of Ca_2RuO_4 up to room temperature. The measurement was done in the coldhead. The black line is the linear fitting of the high-temperature phase, and is a guide to the eye.

A careful low-temperature study was performed in the DMS. Figure 5.29 shows the resistivity profile at low temperatures. The observed flattening in resistivity at low temperatures is a sign of a gapped magnetic ground state. We fitted the data to the equation [55]

$$\rho = \rho_0 + AT^2 + B\Delta^2\sqrt{\frac{T}{\Delta}}\left[1+\frac{2}{3}\left(\frac{T}{\Delta}\right)+\frac{2}{15}\left(\frac{T}{\Delta}\right)^2\right]e^{-(\Delta/T)} \tag{5.5}$$

The third term comes from electron scattering with antiferromagnetic magnons in a large uniaxial anisotropy. The fitting paramter are $\rho = 3.5$ $\mu\Omega$·cm, $A = 4.0\times10^{-4}$ $\mu\Omega$·cm/K^2, $B = 3.9\times10^{-2}$ $\mu\Omega$·cm/K^2, and $\Delta = 21.1$ K. Unfortunately, this is not really the evidence of having AFM ground state. The data also fits well with the FM ground state. We can only conclude that the system has some kind of gapped magnetic ordering.

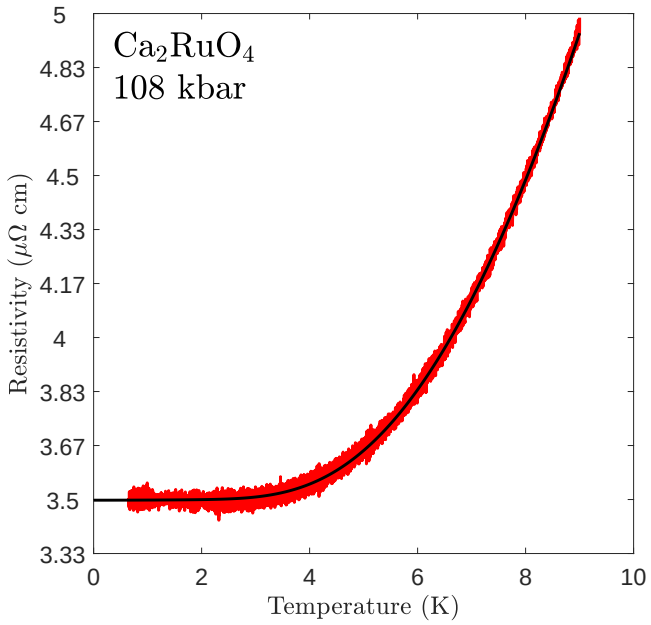

Fig. 5.29 Resistivity measurement of Ca_2RuO_4 at low temperature. The measurement was done in the DMS. The black line is the fitting to equation 5.5, and is a guide to the eye.

These two features of having linear resistivity at high temperature and the resistivity flattening at low temperature is being suggestive of having an antiferromagnetic metallic ground state. According to the previous work at this pressure (however, with two-point measurement), the ground state has an instability towards the superconducting phase at about a few hundred milli-Kelvins [4]. Figure 5.30 shows the resistivity in the sub-Kelvin regime. Without a magnetic field, we observed an initial drop in resistivity at about 400 mK, followed by a clear peak at about 200 mK. The origin of the peak is unclear. As we apply a magnetic field, the peak disappears. The drop in the resistivity is likely to be from the superconductivity. However, the resistivity drops by only a factor of less than 10% at a hundred milli-Kelvin. This suggests that only some part of the sample undergoes superconducting transition (in this case, it may only be filamentary). This result of the critical field, however, contradicts to what has been observed before. The critical field that was observed previously was in the order of 10 mT [4]. There may be some effects from strain, which is expected to occur at this pressure. To investigate this phase more concisely, we need a smaller sample and a better pressure medium such as argon.

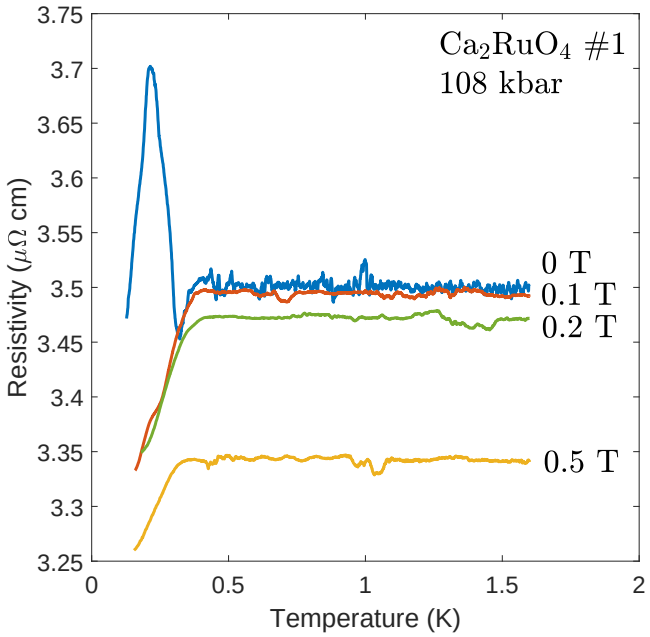

Fig. 5.30 Possible superconducting transition in Ca_2RuO_4.

We propose a possible phase diagram of the calcium ruthenate. What we have added to what has been known is a possible antiferromagnetic phase at a pressure beyond the itinerant ferromagnetic phase. This also implies that superconductivity in high-pressure Ca_2RuO_4 should be even-parity. In fact, antiferromagnetic fluctuation is not the only route to obtain linear resistivity in two-dimensional systems. For example, we have seen in Chapter 4 that linear resistivity in Bi-III arises from scatterings between electrons and soft-phonon (i.e. phason). MnSi also shows this type of non-Fermi liquid $\rho \sim T^{3/2}$ [111] (3D system) but does not have any antiferromagnetic ground state. In the case of MnSi, it was believed that this anomalous power-law arises from the Skyrmion spin-texture state [20, 112].

The non-Fermi liquid behaviour (linear resistivity) in high-pressure Ca_2RuO_4 does not seem to arise from the vicinity of quantum critical point as we do not observe any suppression magnetic ordering transition temperature. A possible scenario is that there is a competition between ferromagnetic and antiferromagnetic interactions, which can be tuned by external pressure.

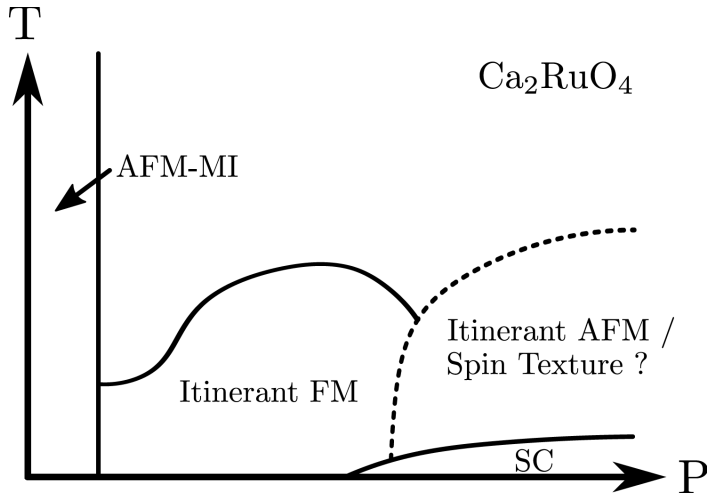

Fig. 5.31 A possible phase diagram of Ca_2RuO_4.

To test the antiferromagnetic phase, one can conduct other experiments that are more direct. For example, neutron scattering or MRI can give the magnetic structure of the system.

5.3 Comparison/Relation to other materials

5.3.1 $La_{1-x}Sr_xMnO_3$

Lanthanum Manganite $LaMnO_3$ has a prototypical perovskite structure (with $n = \infty$ in the RP-formula). The lanthanum valence configuration is $5d^1\ 6s^2$, giving three valence electrons. Oxygen has $2s^2\ 2p^4$, taking two electrons per oxygen. Therefore, manganese (which is $3d^5\ 4s^2$) must give three electrons to form a complete bond, becoming Mn^{3+} and leaving $3d^4$ electrons to the system. The $3d^4$ states get split due to the crystal field, resulting in electrons occupying t_{2g} and e_g states. The energy of this electronic configuration can be lowered by having a Jahn-Teller distortion (it is not hard to see that Mn^{3+} is a Jahn-Teller atom - one can see that the electronic energy is lowered by the further energy splitting by a distortion).

Remarkably, the phase diagram of Sr-doped $LaMnO_3$ is almost identical to the proposed phase diagram of Ca_2RuO_4. This similarity may not be coincidental. Firstly, both lanthanum manganite and calcium ruthenate have four d-electrons. However, the spin configurations are different in these systems. In $LaMnO_3$, $3d$ electrons are very much localised and the crystal field splitting is not so large. All four electrons prefer to align in the same direction (due to Hund's rule). This makes three electrons occupy t_{2g} states and one electron occupy e_g state.

On the other hand, $4d$ electrons in Ca_2RuO_4 is much less localised, resulting in much larger interaction with the environment, making all four electrons occupy the t_{2g} states.

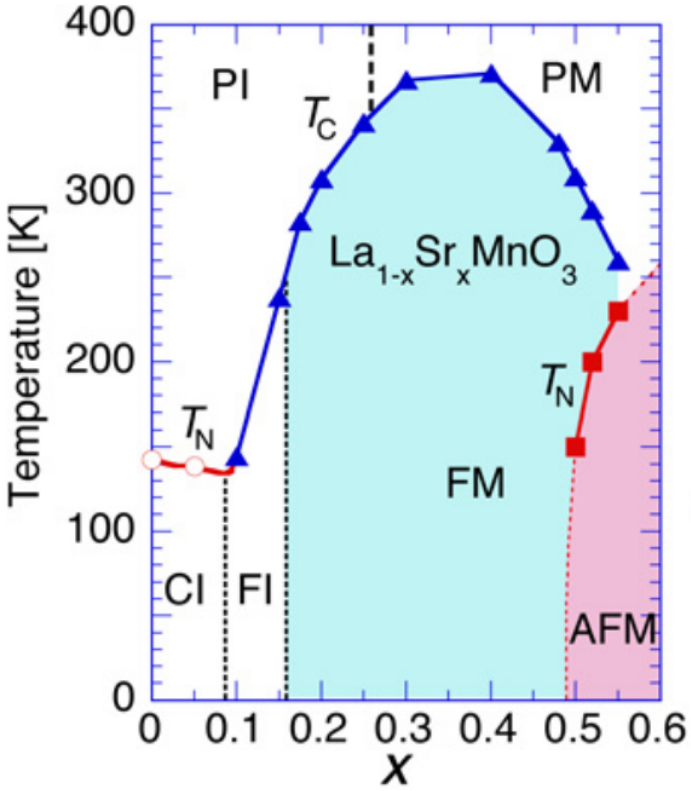

Fig. 5.32 A phase diagram of Sr-doped $LaMnO_3$. CI stands for canted insulating, FI stands for ferromagnetic insulation, PI stands for paramagnetic insulatings, FM stands for ferromagnetic metal, PM stands for paramagnetic metal, and AFM stands for antiferromagnetic metal. Figure credit: [145].

Both $LaMnO_3$ and Ca_2RuO_4 have Jahn-Teller distortion at manganate and ruthenate octahedra [145]. In $LaMnO_3$, the conduction electrons mainly come from e_g state (since d_{z^2} state hybridises strongly with the $2p$ electron in oxygen), the Jahn-Teller distortion makes the system becomes insulating according to the following mechanism: (i) The distortion lowers the energy of d_{z^2} and raises $d_{x^2-y^2}$. When the e_g electron from one site moves to another site, it can singly occupy $d_{x^2-y^2}$ (not energetically favourable due to Jahn-Teller splitting) or doubly occupy d_{z^2} (again, not energetically favourable due to Hund's coupling) [21]. (ii) The distortion reduces the hybridisation to the $2p$ electron from oxygen, hence lowering the hopping parameter of d_{z^2} state [145]. This picture is effectively the same as the Mott-Hubbard model, where electrons get jammed and become an insulator. The Jahn-Teller

effect causes $LaMnO_3$ to be insulators. In Ca_2RuO_4, the mechanism for being an insulator is different since there is no electron occupying e_g state. The reduction in bandwidth in Ca_2RuO_4 mainly comes from the tilt in the RuO_6 octahedra.

When lanthanum (trivalent atom) in $LaMnO_3$ is replaced by strontium (a divalent atom), manganese loses one more electron and becomes Mn^{4+}, which is not a Jahn-Teller atom. The distortion is completely removed when $x = 0.175$, where x is the doping level in $La_{1-x}Sr_xMnO_3$ [21]. This is also similar to the effect of pressure on Ca_2RuO_4 [3, 4]. When the doping level exceeds $x = 0.175$, lanthanum manganite becomes ferromagnetic metal. The mechanism for this ferromagnetic metallic is the double exchange interaction [21], where electrons are delocalised if all local spins align (otherwise, it is not favourable for electrons to hop around due to Hund's coupling). Furthermore, this ferromagnetic exhibits a strong negative magnetoresistance, called the colossal magnetoresistance. The CMR in $La_{1-x}Sr_xMnO_3$ is believed to be connected to double exchange in ferromagnetic: As electrons can hop better when neighbour spins are aligned (due to Hund's coupling), magnetic field reduces resistivity as it makes local spin align in the same direction. [21]. We also observed the CMR in ferromagnetic Ca_2RuO_4 (figure 5.24), showing how similar they are.

One important feature to notice is that the magnetic ordering temperature in $La_{1-x}Sr_xMnO_3$ is an order of magnitude larger than that in high-pressure Ca_2RuO_4. The cause of this discrepancy is likely to come from the dimensionality of the system. In two dimensional system, there is no true long-range order due to the large fluctuation. That means we expect the ordering temperatures in high-pressure Ca_2RuO_4 to be much smaller than $La_{1-x}Sr_xMnO_3$ due to its quasi-2D in nature. Moreover, a two-dimensional system promotes superconductivity [98], and that is why superconductivity arises in Ca_2RuO_4 but not $La_{1-x}Sr_xMnO_3$.

As we have seen, the pressurised Ca_2RuO_4 could turn out to be the two-dimensional analogy of the strontium-doped $LaMnO_3$. The origin of the similarities between these two scenarios is still unclear. However, this may make the high-pressure antiferromagnetic Ca_2RuO_4 more convincing.

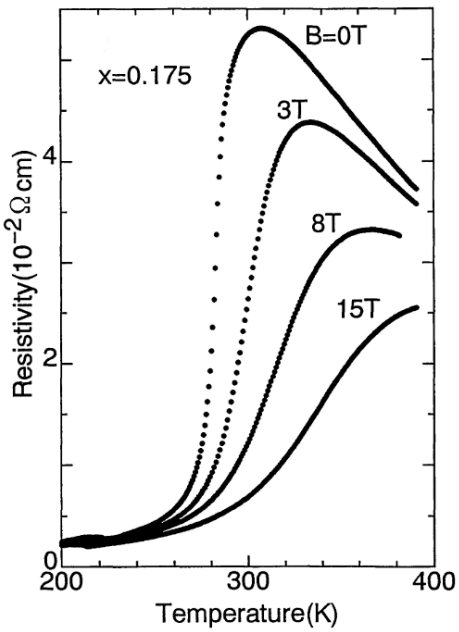

Fig. 5.33 Magnetoresistance in $La_{1-x}Sr_xMnO_3$ with $x = 0.175$. Figure credit: [147].

5.3.2 Sr_2RuO_4

As there is much evidence of competition between antiferromagnetic and ferromagnetic tendencies in Sr_2RuO_4, it was suspected that the order parameter might change the parity by the application of pressure [89]. The story in high-pressure Ca_2RuO_4 may be similar. One difference between high-pressure Ca_2RuO_4 and Sr_2RuO_4 is that the former is unstable towards magnetic ordering. As pointed out in [98] that superconductivity with antiferromagnetic interaction is more stable than ferromagnetic interaction; the same thing happens in high-pressure Ca_2RuO_4. Superconductivity in Ca_2RuO_4 becomes observable when ferromagnetic ordering disappears [4], and the transition temperature rises when the system is tuned away from ferromagnetism (and go into an antiferromagnetic state).

5.4 Summary

There have been many extensive studies on Ca_2RuO_4 over the past twenty years, ranging from pressure works, isovalent doping, the effect of electric field and magnetic field. For the pressure works, they were done mainly in piston-cylinder pressure cells. The detailed resistivity measurement above 30 kbar still lacks. We expand the works by doing detailed

resistivity studies in the ferromagnetic phase. Firstly, we found that resistivity in the ordered state is well-described by the scattering between electrons and gapped magnons. Furthermore, resistivity above the transition temperature follows the power-law $\rho \sim T^{4/3}$, agreeing to the result from the SCR theory of 2D ferromagnetic. The nature of the transition was also studied carefully. It was found that the transition is of second-order up to 75 kbar as there is no hysteresis in warmup-cooldown and the divergence in susceptibility. The differential in resistivity shows that the transition of the ordered state is broad, despite being second-order in nature. This broad transition feature needs to be understood theoretically in the future. Magnetoresistance of both the ferromagnetic phase and the paramagnetic phase are negative. The ferromagnetic phase shows a giant percentage negative magnetoresistance, up to 80% at 9T, 2.5 K.

At the pressure above 100 kbar, we observed the cross-over from $\rho \sim T^{4/3}$ to $\rho \sim T$ in the resistivity measurements. The suggests a change in the magnetic interaction from 2D ferromagnetic to 2D antiferromagnetic. Furthermore, we also observed a magnetic ground state, according to the flattening of the resistivity at low temperatures. Combining these results, we conjecture that the ferromagnetic ground state has transformed into an antiferromagnetic ground state at high pressure.

Chapter 6

Iron-Based Superconductor YFe_2Ge_2 and Frustrated Magnet $PdCrO_2$

This chapter contains two small pieces of work - high pressure study of iron-based superconductor YFe_2Ge_2 and high-pressure study of geometically frustrated magnet $PdCrO_2$. The main theme of this chapter is the exploration of unknown phases.

6.1 YFe_2Ge_2

6.1.1 Introduction and Literature Review

Iron-based superconductivity is a relatively new class of superconductors. It was first discovered in 2006 in LaOFeP [77], which shows superconductivity at 4 K. The discovery was a big surprise in the field since element iron, which is a d-metal, is highly magnetic. In terms of the transition temperature, the highest T_c that has been discovered to date is 55 K in $SmFeAsO_{0.85}$ [119], exceeding the maximum T_c expected for conventional BCS superconductor. Moreover, they are promising to exhibit a large critical field. For instance, $BaFe_{1.8}Co_{0.2}As_2$ was predicted to have an upper critical field of 43 T by measuring the coherence length using scanning tunnelling spectroscopy and vortex imaging techniques [165]. Therefore, iron-based superconductivity attracts much attention in the condensed matter community in both fundamental study and its potential applications in industry.

Many iron-based superconductors combine with pnictogen [1] and chalcogen[2] and can be classified by the a different chemical formula. They can be classified into a few groups:

[1] Pnictogen are materials in group 15

[2] Chalcogen are materials in group 16

1. 11-family has a general formula of FeX where X is a chalcogen. Some examples of materials in this class are FeSe [117] and FeTe [46].

2. 111-family has a general formula of AFeX where A is an alkaline metal and X is a pnictogen. Some examples of material in this class are LiFeAs [152] and NaFeAs [37].

3. 122-family has a general formula of $AeFe_2X_2$ where Ae is an alkaline-earth metal and X is a pnictogen. Some examples of material in this class are $BaFe_2As_2$ [123] and $SrFe_2As_2$ [126].

4. 1111-family has a general formula of RFeXO where R is a rare-earth metal and X is pnictogen. Some examples of material in this class are LaFeAsO [78], SmFeAsO [36], and PrFeAsO [119].

5. More exotic families, such as 42622-family with a notable example of $Sr_2ScFePO_3$ [164].

Although all of these families seem very different in structure, all of them have layers of iron with pnictogen/chalcogen, which is seen in figure 6.1 (This somehow resembles the cuprate superconductors where they have layers of copper oxide instead). It becomes clear afterwards that it is these two-dimensional electronic structures that gives rise to high-temperature superconductivity. The 2D behaviours are observed in the intraplane and interplane magnetic coupling. In cuprate superconductor, $J_\perp/J \sim 10^{-5}$ whereas $J_\perp/J \sim 10^{-4}$ in 1111 pnictides and $J_\perp/J \sim 10^{-2}$ in 122 pnictides [86]. Another evidence is the electronic band structures which are usually in the form of two-dimension cylindrical sheets [80].

Usually, these undoped iron-based compounds have a spin density wave ground state at ambient pressure. The doping of electron/hole, isovalent doping, or external pressure can usually suppress the magnetically ordered state, and eventually, superconductivity emerges around the expected quantum critical point. A general phase diagram of the iron-based superconductor is shown in figure 6.2. Notice that the phase diagrams of iron-based superconductors have some similarity to cuprates, as superconductivity arises when a magnetic order gets suppressed[3].

The belief that iron-based superconductor is unconventional stems from (i) the high transition temperature, exceeding the BCS prediction[4], (ii) the similarity of the phase diagram between iron-based superconductor and cuprates.

[3]One of the most significant differences between cuprate superconductors and iron-based superconductors is that the parent compounds of the former are insulator whereas the latter are conductors.

[4]This way of looking may be dubious since there are a few materials that exhibit close to room temperature superconductor (however, under extremely high pressure) but are conventional ones. Examples are hydrogen

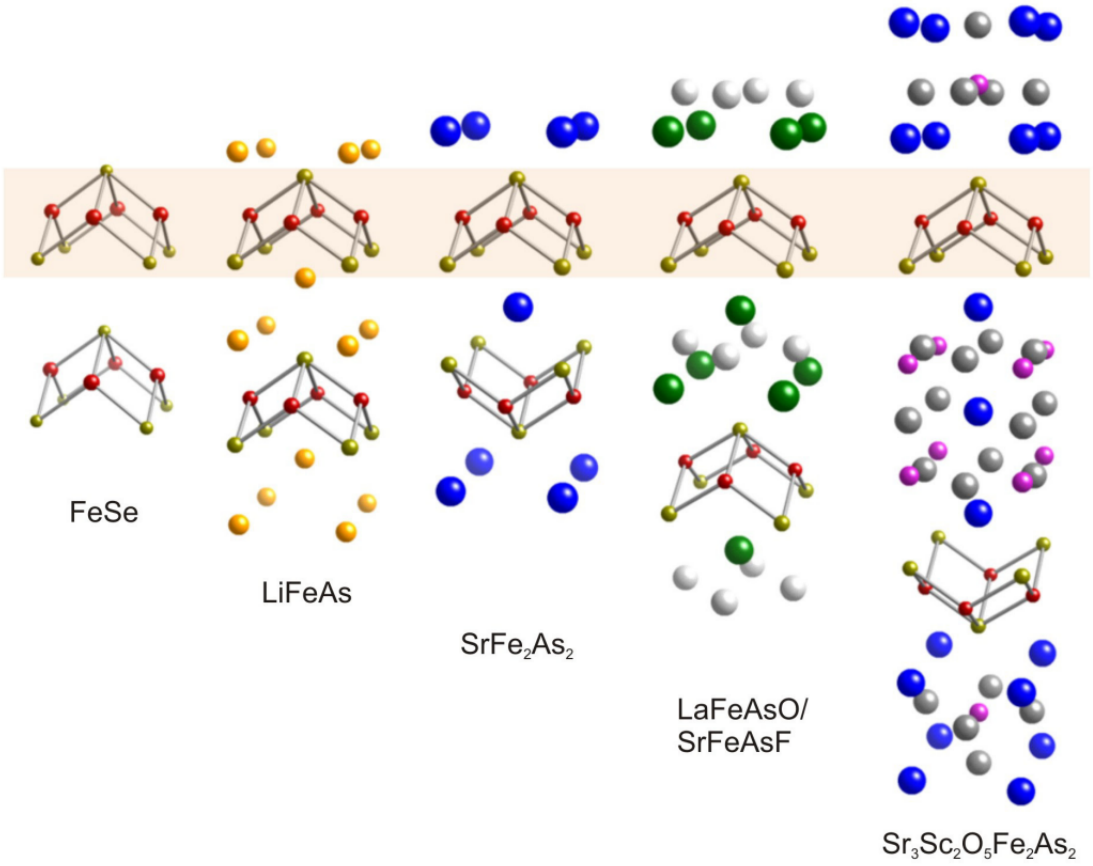

Fig. 6.1 Structures of iron-based superconductors coming from five different families in chemical formula. The figure was taken from [110]

Although not a consensus, it is widely believed that the pairing mechanism must come from magnetic fluctuations. It may not be difficult to convince ourselves that it should be the case by looking at the phase diagram. In these unconventional superconductors, the parent compounds usually have some magnetic order. As we suppress the magnetic order and reach the phase boundary where magnetic fluctuation is strongest[5], superconductivity arises[6]. In contrast to cuprate, which is believed to be d-wave, many experiments and theoretical predictions point the iron-based superconductors toward an s-wave [16, 38, 65, 107] superconducting order parameter. However, there is a significant difference to

sulfide and carbonaceous sulfur hydride [132]. This may be something very fundamentally incomplete to the way we think about superconductivity.

[5]This is due to the divergence in correlation functions.

[6]Hence, the quantum phase transition is the subject that is currently growing very fast and is needed for a better understanding of unconventional superconductors.

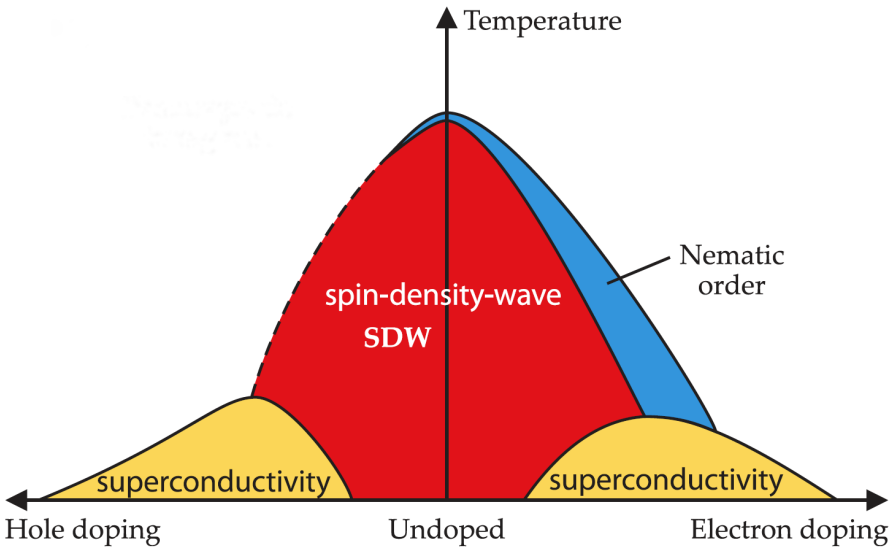

Fig. 6.2 General phase diagram of iron-based superconductors, based on $BaFe_2As_2$. The figure was taken from [80].

conventional superconductors, namely that there is a relative sign change amongst different Fermi surfaces. This pairing mechanism is called $s\pm$-wave.

Now, we give an overview of a particular material, YFe_2Ge_2, which we have been working on and will be the main subject in this section. YFe_2Ge_2 is classified into the 122-family iron-based superconductor. However, it does not fall into either pnictide or chalcogenide categories. Instead, Fe is combined with the carbon group, which is group 14 in the periodic table. We can identify the valency of this material by counting as follows: Firstly, the electronegativity of Y $<$ Fe $<$ Ge, meaning that yttrium tends to give all valence electrons, and germanium tends to fill its shells. Yttrium has valence $4d^1\ 5s^2$, iron has valence $3d^6\ 4s^2$, and germanium has valence $4s^2\ 4p^2$. In this material, Ge-Ge forms a covalent bonds, sharing two electrons together. Therefore, germaniums take only 6 electrons in total, and iron needs to give 1.5 electrons each. The electronic configuration is then 6.5 electrons per iron.

YFe_2Ge_2 has a tetragonal structure shown in figure 6.3. As the value of $c/a = 2.64$ is comparatively smaller than other iron-based superconductors (for example, $c/a = 3.61$ in KFe_2As_2 at ambient pressure [136]), it is expected that this material exhibits more three-dimensional character rather than quasi-two-dimensional. The 3D character arises because of the covalent bond between Ge-Ge, which is strong enough to collapse the structure and make it tightly packed. The Fermi surface of YFe_2Ge_2 is shown in figure 6.3 shows very much 3D character compared to its sibling compound KFe_2As_2. By applying external pressure,

KFe_2As_2 undergoes a structural phase transition and becomes the 'collapsed' tetragonal structure, which is very similar to YFe_2Ge_2 in both structures and the Fermi surface (with a difference only at the vicinity of Γ point).

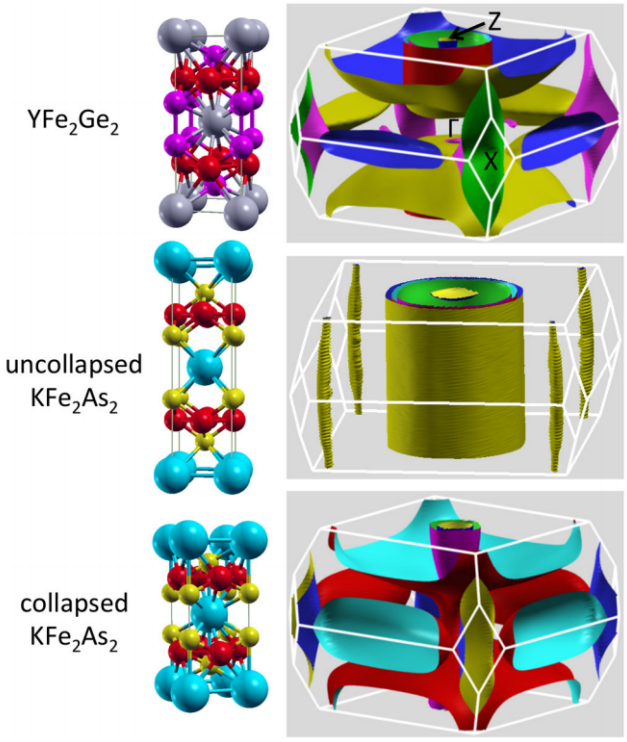

Fig. 6.3 (Upper figure) Left: The structure of YFe_2Ge_2 with the lattice parameters $a = 3.9617(5)$, $c = 10.421(1)$ and the position of Ge atoms in c-direction is 0.3789(3). Right: Fermi surface of YFe_2Ge_2. The Z and X labels indicate hole pocket and electron pocket, respectively. (Middle figure) Left: Structure of uncollapsed KFe_2As_2. Right: Fermi surface of uncollapsed KFe_2As_2. (Bottom figure) Left: Structure of collapsed KFe_2As_2. Right: Fermi surface of collapsed KFe_2As_2. The figure was taken from [35].

YFe_2Ge_2 at ambient pressure has a superconducting ground state. The transition temperature depends heavily on the amount of the disorders which suggests its superconductivity is unconventional. It was first observed to be a superconductor in 2014 [168], but any detailed studies are complicated due to the effect of disorders in YFe_2Ge_2. In 2020, Dr Jiasheng Chen managed to grow high-quality single crystal of YFe_2Ge_2 with an RRR of better than 400, which opens up the possibility to investigate the intrinsic properties of superconductivity in this material. The observed transition temperature is approximately between 1.5-1.8 K. In this aspect, YFe_2Ge_2 is quite different from most iron-based superconductors since most of them have a magnetic ground state at ambient pressure. In the normal state above superconducting,

YFe_2Ge_2 shows non-Fermi liquid behaviour in resistivity, with a power-law $\rho \sim T^{3/2}$. The exponent $3/2$ is not well understood but is speculated to arise from the vicinity of a QCP. Therefore, it is desirable to investigate the effect of pressure on YFe_2Ge_2, especially to see if it can be tuned away from the proposed QCP by applying pressure.

It is also worth noting a sibling compound $LuFe_2Ge_2$ which has an AFM ground state. The ordering temperature of $T_N = 9$ K (at ambient pressure) is observed to increase as a function of pressure. On the other hand, the effect of chemical substitution of Lu by Y gives the opposite result. This can be view as the effect of chemical pressure - lutetium has a smaller atomic radius (227 pm) than yttrium (240 pm) and thus gives rise to negative chemical pressure (larger average unit cell). Substituting Lu by Y in $Lu_{1-x}Y_xFe_2Ge_2$, the Néel temperature is suppressed completely at $x = 0.2$. The phase diagrams are shown in figure 6.4.

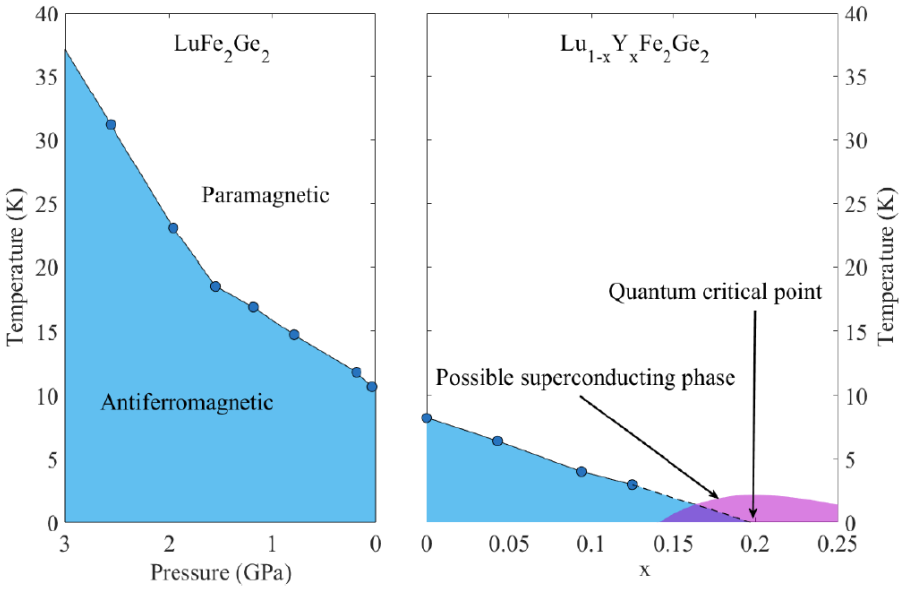

Fig. 6.4 Phase diagram of $LuFe_2Ge_2$ in two situtations. The left figure is the phase diagram under pressure. The right figure is the phase diagram under chemical substitution of Y to Lu. The figure was taken from [128], and the data come from [56, 118].

Why study YFe_2Ge_2?

The reasons why this material is very interesting can be summarised as follows:

1. It is now possible to grow very high-quality samples of YFe_2Ge_2 with a residual resistivity ratio of more than 600. This is very crucial in the studying of unconventional superconductors due to its sensitivity to the impurity level.

2. With these high-quality samples, it is now possible to map out every single sheet of the Fermi surface in YFe_2Ge_2. This is very important to fundamental studies. Without these conclusive experimental results, it would be impossible to understand iron-based superconductivity fully.

3. Low superconducting transition temperature allows us to study the normal-state properties without any interference from phonon, which is again very important since we only focus on magnetic interactions in these unconventional superconductors.

4. Dimensionality: YFe_2Ge_2 has a very different character from other iron-based superconductors. The covalent Ge-Ge bonds change the usual 2D character to a 3D character. This means that we can understand the role of dimensionality better by studying YFe_2Ge_2.

6.1.2 Previous High Pressure Works in AC Susceptibility Measurement

This section quotes previous measurements in AC susceptibility study at high-pressure done by Dr Patricia Alireza and Dr Jiasheng Chen. Figure 6.5 shows the result from AC susceptibility measurement from ambient pressure to 70 kbar, giving a significant result that the superconductivity in YFe_2Ge_2 can be suppressed entirely by applying pressure of 70 kbar. Interestingly, there is not much effect in pressure up to 40 kbar, but superconductivity is suppressed quickly above 40 kbar and eventually disappears at 70 kbar.

The study in AC susceptibility which follows the transition temperature as a function of pressure raised a new question: what kind of phase is YFe_2Ge_2 in after suppressing superconductivity? The answer to this question will led us construct the phase diagram of YFe_2Ge_2, which would answer the origin of the unusual power-law behaviour in resistivity. Therefore, the desired experiment is resistivity measurement. We will pay attention closely on the development of the power-law exponent in resistivity as a function of pressure.

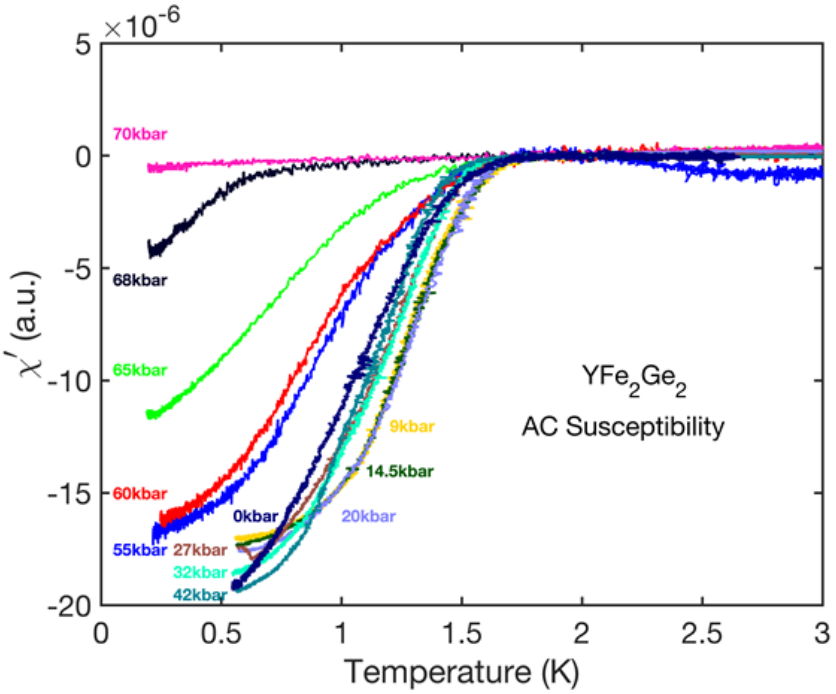

Fig. 6.5 AC susceptibility measurement in YFe_2Ge_2 from ambient pressure up to 70 kbar.

6.1.3 Results and Discusstions

This project results from collaborations between Puthipong Worasaran, Dr Patricia Alireza, and Dr Jiasheng Chen. PW and PLA set up two resistivity pressure cells for YFe_2Ge_2 (PLA, PW, JC prepared the samples, and PW prepared the pressure cells). The sample was grown by JC, and he did the measurement in the DMS system.

The difficulty in this project is the following: since YFe_2Ge_2 is an unconventional superconductor, the transition temperature is highly sensitive to the impurity concentration. In order to get a reliable result, the measurement of all pressure points needs to be done on a single sample. This poses a significant difficulty due to the high failure rate in pressure cells, meaning we have to start over from zero if the pressure cell breaks. Because of this, we use a different strategy to maximise efficiency. Our strategy is to set up two pressure cells. The first pressure cell was set up to go quickly to 80 kbar only for exploration and to confirm that the project is worth pursuing. The second pressure cell is dedicated to more careful studies by going up slowly in pressure.

Superconducting Transition

In both pressure cells, the samples are contacted using a 4-point measurement technique with the straight line contacts geometry. The liquid medium used is glycerol. The anvil is moissanite with the culet of 0.8 mm. We have measured the first pressure cell at 3.5 kbar, 58 kbar, 68 kbar, and 79 kbar. The second pressure cell was measured with smaller interval, from 6 kbar to 61 kbar. The current used in the first pressure cell (and a first few pressure points in the second cell) is 0.3 mA with a room-temperature transformer, while 0.1 mA was used with a low-temperature transformer in most of the measurements in second pressure cell.

We start by showing data in the first pressure cell as a preliminary study. Figure 6.6 shows the overall results from resistivity measurements in this first pressure cell. Note that the data at 3.5 kbar was shifted slightly due to non-zero voltage in the superconducting state. There are a few possibilities for the offset in resistivity. Firstly, voltage wire and current wire could be touching each other, giving rise to a non-zero signal coming from reading contact resistance. However, by a careful optical inspection through a microscope, it is unlikely that this happens (although we cannot say with certainty since the sample is tiny). Secondly, the common-mode problem in the DMS is more likely to happen in this case (as a similar problem also happens in the second pressure cell - the resistivity goes below zero - this was eventually fixed by replacing resistive measurement wires with superconducting wires). Interestingly, there is still some trace of superconducting in the sample even at 79 kbar, which is in contrast with the susceptibility measurement, suggesting that there may be some filaments of superconducting left at this pressure.

We are not certain about why the data at 58 kbar shows almost twice resistivity to those at 68 and 79 kbar. However, since the measurement system was not very reliable (using conductive wires and no low-temperature transformer) in this first pressure cell, the measurement in this cell can be used as only a guide.

Now, we present data from the second pressure cell, which was done more carefully with a better measurement setup. Firstly, superconducting transition is almost completely suppressed at pressure $\sim$60 kbar, agreeing well with the first pressure cell. Secondly, there is no jump in the residual resistivity anymore (as in the 58 kbar data of the first pressure cell). This suggests that the jump in the first pressure cell is likely to be an artifact.

We extract the superconducting transition temperature from the point at which resistivity drops by 50% to the normal state resistivity. Figure 6.8 shows the effect of pressure on the superconducting transition temperature.

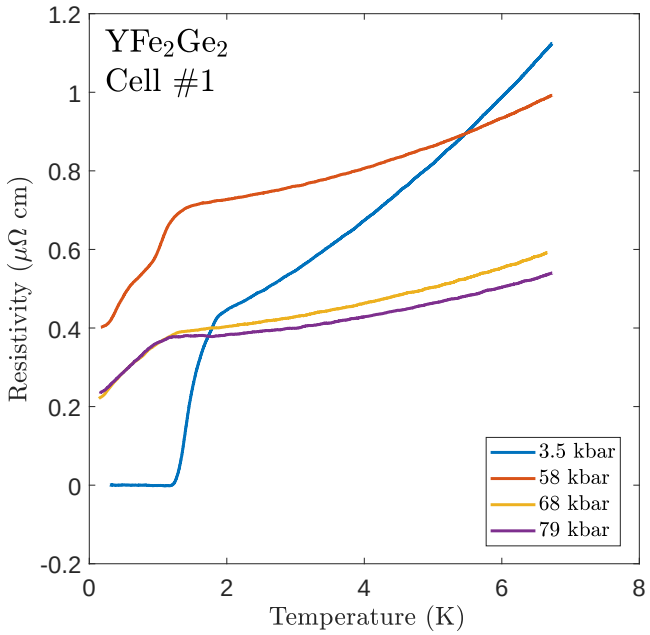

Fig. 6.6 Resistivity measurement in YFe_2Ge_2 in the cell #1 from ambient pressure up to 79 kbar.

Normal State Power Law

In the preliminary measurement of the first pressure cell, we study the power-law behaviour by fitting normal-state resistivity to the equation $\rho = \rho_0 + AT^n$. It can be seen clearly that the value of the exponent n increases as a function of pressure as shown in figures 6.9. At low pressure, the power law exponent is approximately $n \sim 1.6$. Then the exponent reaches $n \sim 1.9 - 2$ at about 80 kbar. At this pressure, superconductivity has disappeared in the AC susceptibility measurement.

The careful study was performed in the second pressure cell, confirming the trend that has been observed in the first pressure cell. The plot of the power-law exponent as a function of pressure is shown in figure 6.10. The increase in the power-law exponent can be interpreted as the cross-over from non-Fermi liquid to Fermi liquid. This result is also suggestive that superconductivity arises from the vicinity to a QCP, showing a similar phase diagram to cuprates.

This result is very curious when comparing with the doped material $Lu_{1-x}Y_xFe_2Ge_2$. In the simplest picture, the substitution of yttrium by lutetium in YFe_2Ge_2 should resemble the effect of presure (as lutetium atom is smaller than yttrium atom). However, the recovery of Fermi liquid at high pressure makes it impossible to connect the high-pressure YFe_2Ge_2 to

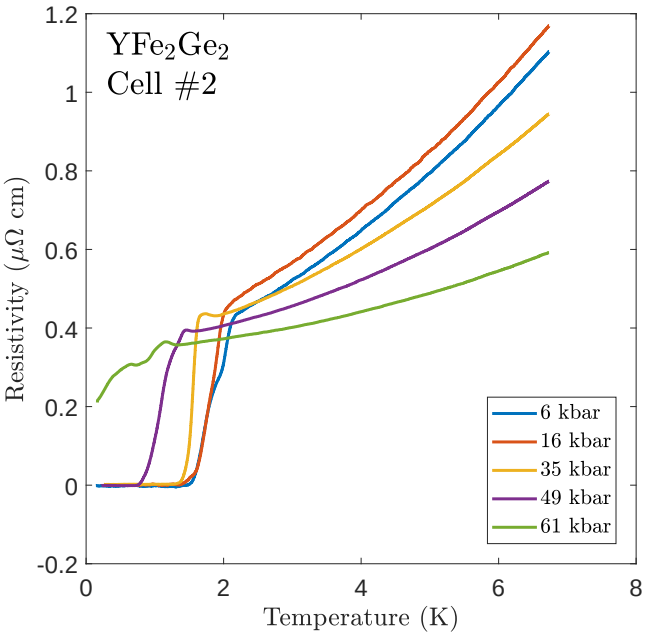

Fig. 6.7 Resistivity measurement in YFe_2Ge_2 in the cell #2 from ambient pressure up to 61 kbar.

the antiferromagnetic phase in $LuFe_2Ge_2$. It is also possible that the effect of pressure is not the same as a chemical substitution. For instance, YFe_2Ge_2 exhibits two types of spin-fluctuation, $(\pi,0,\pi)$ and $(0,0,\pi)$ [159], while $LuFe_2Ge_2$ shows only the latter one [56, 159]. Therefore, it is possible that Lu-Y substitution affects $(0,0,\pi)$ more than $(\pi,0,\pi)$, while pressure affects both. The effect of pressure is to increase the kinetic energy of electrons, broadening energy bands and lowering density of states. A criterion for magnetic instability is $Ug(\varepsilon_F) > 1$ ($g(\varepsilon_F)$ is density of state at Fermi energy: this is the Stoner criterion for ferromagnetism), or more generally, $U\chi^{(0)}(\boldsymbol{q}) > 1$ ($\chi^{(0)}(\boldsymbol{q})$ is the Lindhard function of non-interaction electrons system). Therefore, we may not expect to find any magnetic order at higher pressure. A few things we can do to investigate further: (i) track the antiferromagnetic transition in $LuFe_2Ge_2$ at a broader pressure range. One may expect the antiferromagnetic transition to go down when pressure is applied futher. However, this is not practical as the signature of the antiferromagnetic ordering transition in resistivity is very subtle [56]. Any inhomogeneity at high pressure will smear out the transition completely. Although the heat capacity measurement gives more visible hump, it is not simple to do it accurately in a smaller pressure cell (thus limit the pressure range). (ii) produce high-quality samples of yttrium-doped $LuFe_2Ge_2$ to see if superconductivity can be observed, and then study the power-law behaviour under pressure.

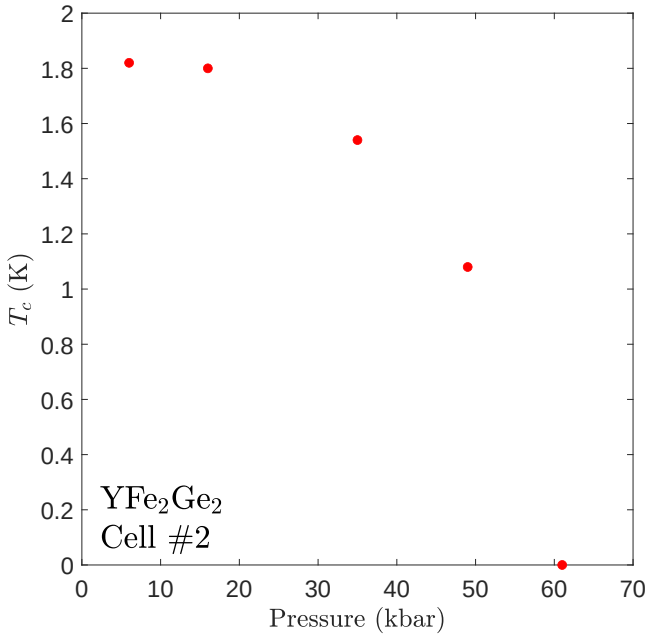

Fig. 6.8 Superconducting transition temperature versus pressure in YFe_2Ge_2 in the cell #2.

We conclude this section by drawing the temperature-pressure phase diagram of YFe_2Ge_2, shown in figure 6.11, from the results of our study. The phase diagram represents superconducting ground state of YFe_2Ge_2 at ambient pressure with non-Fermi liquid state above it. We have seen the suppression of superconductivity and the Fermi liquid signature in the power-law study. This allows us to make a phase diagram and understand the position of this material much better.

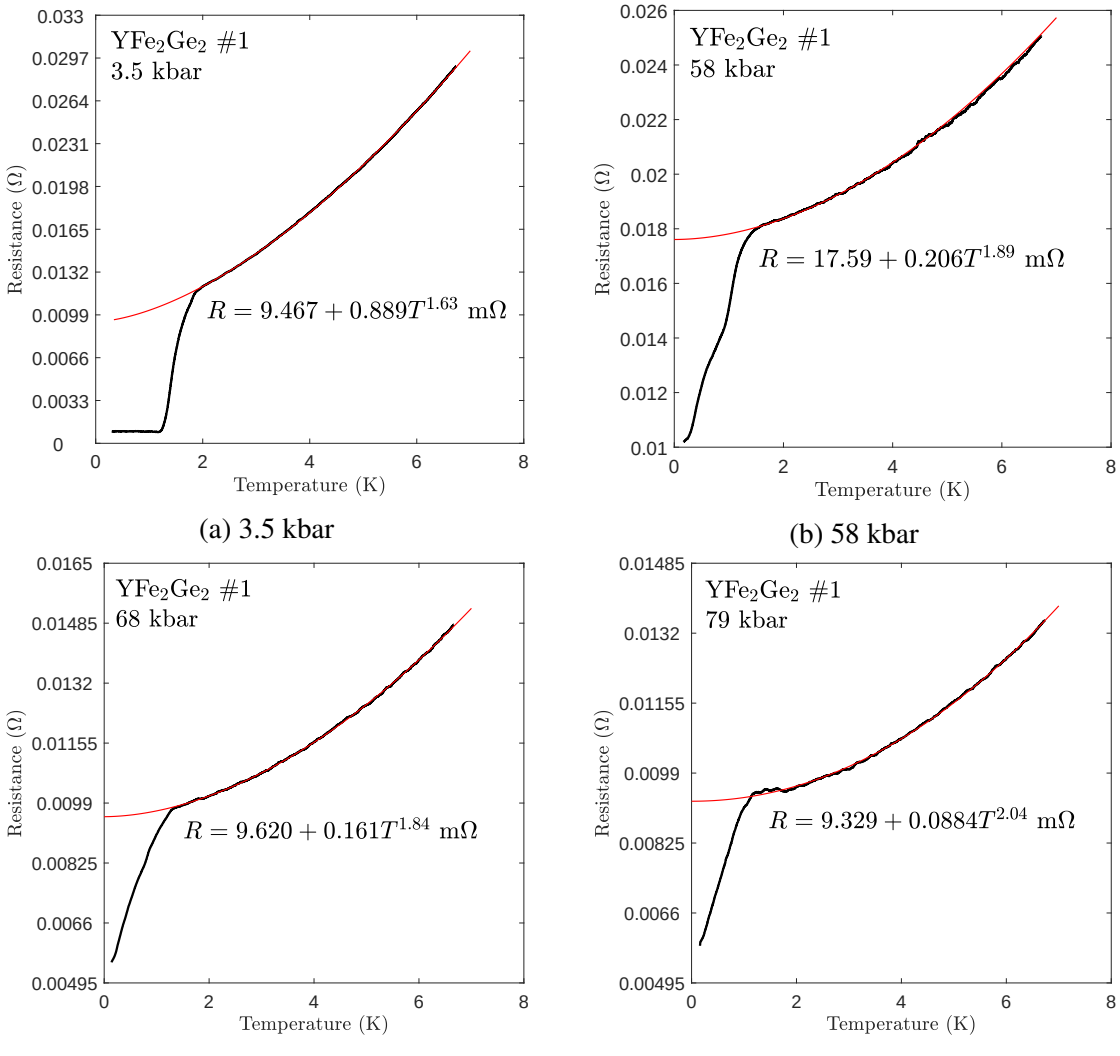

(a) 3.5 kbar

(b) 58 kbar

(c) 68 kbar

(d) 79 kbar

Fig. 6.9 Power law fitting to the normal state resistivity of high pressure YFe_2Ge_2. The red lines are the guides for the eye.

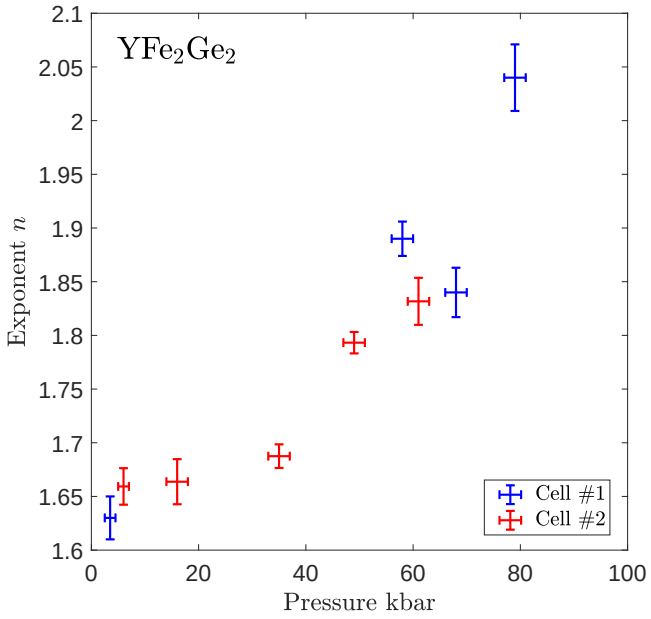

Fig. 6.10 Power-law exponent as a function of pressure. The averaging is done before the fitting. The range of the fitting is between 2 K and 6.7 K.

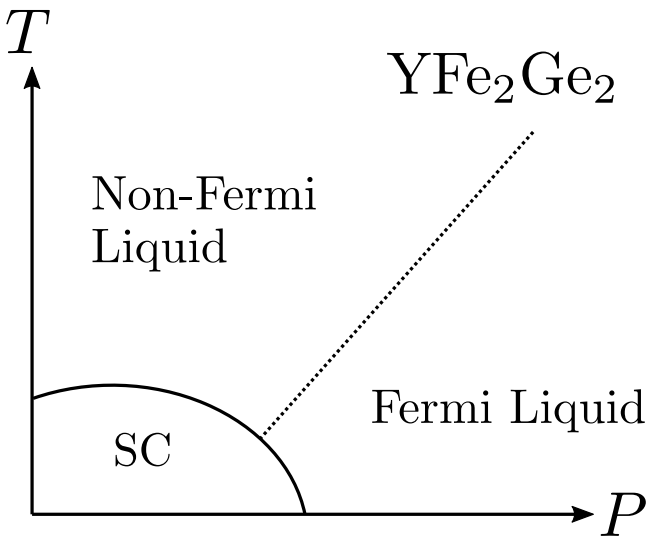

Fig. 6.11 Temperature-Pressure phase diagram of YFe_2Ge_2.

6.2 $PdCrO_2$: Exploration

6.2.1 Introduction and Literature Review

Magnetic frustration in the spins system has been a subject of significant interest for many decades. There are two types of frustration - random (spin glass is an example of this type) and geometrical. We will focus on geometrical frustration here since it is directly related to our work. The geometry of the underlying lattice can cause geometrical frustration. This phenomenon occurs specifically in the spin system with antiferromagnetic interaction, in which two adjacent spins prefer to align antiparallel to each other. We give a simple example of how this happens by considering the antiferromagnetic Ising spin system (in which spins are forced to be in either up or down direction). For a square lattice, the ground state is simply an antiferromagnetic Néel state, as shown in figure 6.12a. On the other hand, triangular lattice could not fulfil the condition of the Néel state, which is demonstrated in figure 6.12b. When two spins at the bottom of the triangle are opposite, the third spin cannot be antiparallel with those two spins simultaneously.

The situation above implies that the ground state is highly degenerate. When we extend the situation above to the whole lattice, the degeneracy is usually of the order of total lattice site number. In a triangular lattice, this degeneracy gives a non-zero entropy of $S = 0.323Nk_B$ down to zero temperature [14]. The frustration, in turn, enhances spin fluctuation and destroys magnetic order. If the fluctuation is strong enough, there may be no magnetic ordering even at absolute zero. This state is the so-called spin liquid state, which Philip Anderson predicted to be the ground state of the frustrated spin-1/2 system [7]. The degrees of frustration is defined to be $f = |\Theta_{CW}| / T_c$ where Θ_{CW} is a parameter from the Curie-Weiss susceptibility $\chi \sim (T - \Theta_{CW})^{-1}$ and T_c is the magnetic transition temperature. For non-frustrated system, we have $f = 1$. With frustration, the transition temperature gets suppressed due to the fluctuation, giving rise to a larger value of f. Some other interesting related examples of geometrical frustration is the spin-ice system, which gives a very exotic magnetic monopole elementary excitation [31]. Application-wise, frustration systems are also good candidates for adiabatic demagnetisation refrigeration at low temperatures since the ground state entropy is highly tunable by magnetic field [144]. Furthermore, it has a potential to be realised in quantum computing technology [124].

Palladium Chromate, or $PdCrO_2$, is a delafossite layered material with a triangular lattice. The crystal is made of stacks of conducting Pd layers alternating with Mott insulating CrO_2 layers, as shown in figure 6.13.

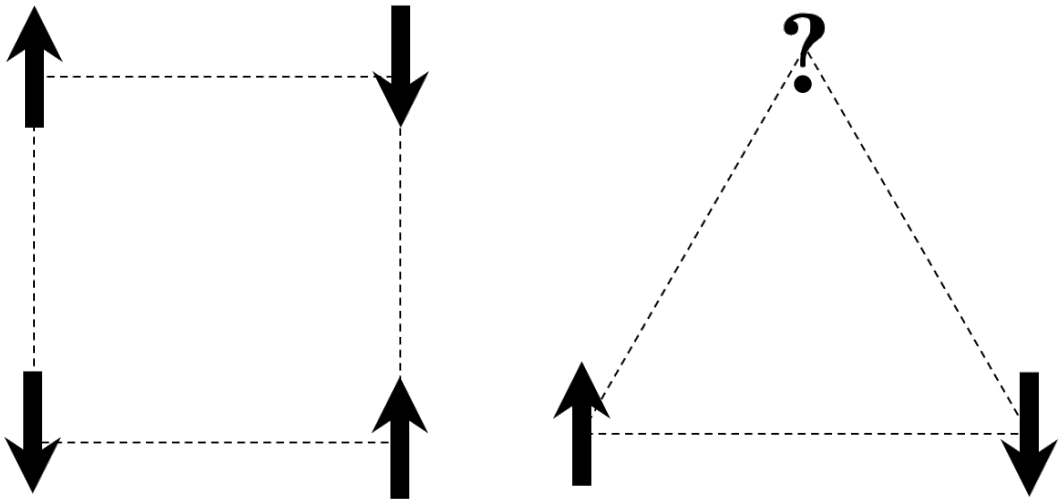

(a) Square lattice (b) Triangular lattice

Fig. 6.12 Demonstration of magnetic frustration due to lattice geometry. The interaction between spins is of AFM type.

$PdCrO_2$ has a local moment of $S = 3/2$ located at each Cr^+ site, forming a frustrating triangular lattice. The valence electrons $3d^3$ of chromium atom split due to the octahedral crystal field into half-filled t_{2g} and empty band e_g. The strong electron-electron interaction drives the CrO_2 plane into a Mott insulator [63]. The local spin is found to behave in accordance with the Heisenberg spin from the susceptibility measurement [141]. Due to the local moment being larger than 1/2, the frustration is partially relaxed by having a short-range 120 degrees antiferromagnetic order even at room temperature [137]. At the temperature $T_N = 37.5$ K, $PdCrO_2$ undergoes a weakly first-order antiferromagnetic transition with 120 degrees spins alignment. The moment direction is mostly on *ab*-plane. [63, 94, 140]. This transition can be observed clearly in electrical transport, magnetic susceptibility, and heat capacity measurements [142]. The result from magnetic susceptibility gives $f = 13$, which indicates extreme frustration in the system. The Pd plane, sandwiched between chromate layers, is metallic due to the itinerant 4d conduction electrons. Because of this two-dimensional nature, $PdCrO_2$ shows an extreme anisotropy between the ab-plane and the c-direction. The anisotropy can be observed directly in resistivity measurement, in which resistivity in the c-axis is significantly larger than that in the ab-plane by a factor of $\rho_c/\rho_{ab} \sim 150$ depending on temperature [141]. The quantum oscillation technique also mapped out the Fermi surface of $PdCrO_2$, and it matches the reconstructed Fermi surface of $PdCoO_2$ into magnetic unit cell [63], suggesting the strong interacting between itinerant 4d electrons in the Pd planes and localised magnetic electrons in the CrO_2 planes.

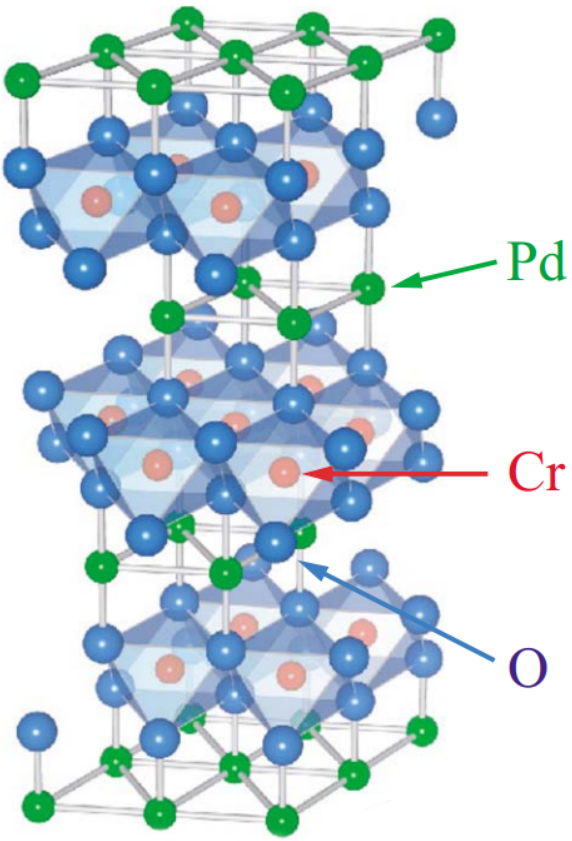

Fig. 6.13 Structure of $PdCrO_2$. The lattice constants are $a = b = 2.930$ Å and $c = 18.087$ Å. The figure was taken from [142].

Although there are many studies already in $PdCrO_2$, no pressure study has been conducted in this material. Therefore, this project aims to study the effect of pressure on the AFM transition and explore any unknown high-pressure phase.

The other intriguing aspect of this material is that it has anomalously small residual resistivity, reported to be 0.05 $\mu\Omega$·cm in [141], suggesting some kind of enhancements in conductivity. In fact, the small residual resistivity was observed in this family of materials, including $PdCoO_2$ and $PtCoO_2$ [106]. Moreover, there are evidence that the flow of electrons in these materials are in the hydrodynamic limit [97].

6.2.2 Results and Discusstions

We present our result of resistivity measurement of $PdCrO_2$ under pressure, up to 108 kbar. The moissanite anvil of 0.8 mm culet and beryllium copper gasket was employed in the experiment. Glycerol was used as the liquid medium. We make contacts in the straight-line

geometry with the voltage contacts on the ab-plane without touching the side to avoid any anisotropy. The AC transport mode in PPMS was used with a current of 8 mA and 23 Hz. The value of resistivity is obtained by comparing the ambient pressure resistivity of 9.4 $\mu\Omega \cdot$cm from [141]. The sample we used has RRR$\gtrsim$100, which is of very high quality. The small resistivity at room temperature, and even a hundred times smaller at 2 K, makes it rather challenging to observe the antiferromagnetic transition (since we need both excellent temperature control and an immaculate measurement system - it is not easy to have both at the same time). This fact has posed another problem in our measurement in the PPMS, as we describe in the following section.

Inductive Cross-Talk Problem in PPMS

In the PPMS anatomy, there is a vacuum feedthrough made of 'Inconel' (this is the trademark name, it is nickel-chromium superalloy) at the bottom of the system. Inconel, in turn, has a peak in magnetic susceptibility between 25 K and 40 K. When performing AC transport or AC susceptibility, there is an inductive cross-talked between the current leads to the Inconel and to the voltage leads (and the temperature-dependent susceptibility in Inconel manifests the same effect as changing the vacuum magnetic permeability). This induction effect will distort the waveform measured by the ACT option, resulting in a spurious peak in the translated value right at the temperature of the peak in Inconel's susceptibility. This effect does not appear in most measurements because the signal from inductive cross-talk is usually tiny compared to a sample signal. However, when we work with samples with very small resistance as is the case here, the cross-talk with the Inconel vacuum feedthrough becomes much more pronounce and can be seen in the measured signal. The way to deal with this kind of cross-talk is to suppress the peak in the susceptibility by applying a few hundred Oes of magnetic field. The full explanation of this issue is given in [47].

In our PPMS, the peak in AC susceptibility is right at 38 K (very close to the antiferromagnetic transition in the sample), making it difficult to notice this problem in the low-pressure region. This effect manifests as a dip (or a hump) in the resistivity measurement, as shown in figure 6.14. The dip at 38 K is not the transition that we are looking for, but it comes from the cross-talk with the Inconel. The nature of AFM should be kink-like rather than a dip, which can be seen in figure 6.15. Because of this reason, we do not have good data below 37 kbar.

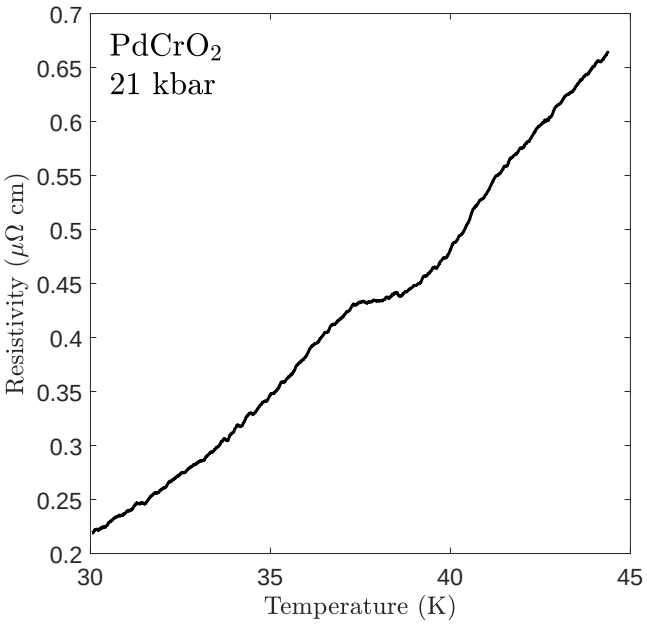

Fig. 6.14 Resistivity measurement in $PdCrO_2$ at 21 kbar between 30 K to 45 K. The dip at 38 K is not due to the sample, but the cross-talk with the Inconel.

Resistivity Measurement

In this section, we present data from 37 kbar up to 108 kbar. Due to the problem with Inconel cross-talk, we applied a magnetic field of 500 Oe. We start by presenting the overall resistivity in the vicinity of the transition at all pressure points, showing in figure 6.16. The temperature sweep rate is 0.02 K/min.

There are a few features we will talk about in this graph. The most noticeable feature is the significant increase in resistivity in the 85 kbar data compared to lower pressure data, suggesting that we may have entered into some unknown phase. However, the nature of this phase is unclear, and we have not investigated this further. At this pressure, we were unable to observe any antiferromagnetic transition, which may be because of inhomogeneity in liquid medium. Therefore, we need to clearify if the antiferromagnetic transition temperature can be suppressed to zero, or if the material undergoes a structural transition before the antiferromagnetic ordering gets completely suppressed. A follow-up experiment to do in the future is to perform the same experiment but with better liquid medium, and study more carefully at pressure above 80 kbar. Power-law study down to base temperature is very much desirable to study as the data at 108 kbar shows the resistivity flattening at low temperature. Once the antiferromagnetic transition is truly suppressed, we may expect

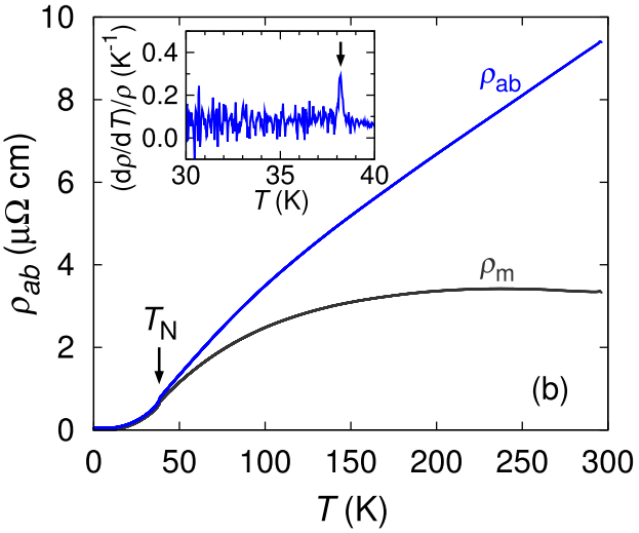

Fig. 6.15 Resistivity measurement in $PdCrO_2$ at ambient pressure. The figure was taken from [141].

to see superconductivity emerging at sub-Kelvin temperature as it is the case in many unconventional superconductors.

Now, we show the data in the pressure range between 37 kbar and 75 kbar for clarity in the kinks. The plot of the data is shown in figure 6.17. The kink at 37 kbar is highly apparent, whereas it gets broadened at a higher pressure and almost disappears at 75 kbar due to inhomogeneity of the pressure medium. To extract the AFM transition temperature properly, we differentiate the resistivity curve and obtain the peak right at the transition temperature, as shown in figure 6.19. The plot in figure 6.18 shows the transition temperature as a function of pressure. In this phase diagram, the AFM transition initially goes up, reaching almost 45 K at 46 kbar, and drops back down slowly. The error bars in the graph are obtained by measuring the half-width of the peak in the differential resistivity.

In conclusion, the antiferromagnetic transition temperature is insensitive to external pressure. The high-pressure transition gets broadened due to pressure medium inhomogeneity. It is desirable to study more carefully using a better pressure medium, such as an organic liquid medium or a compressed gas, at a pressure higher than 50 kbar. The studies at about 85 kbar also deserve more attention, as there may be a structural phase transition below this pressure.

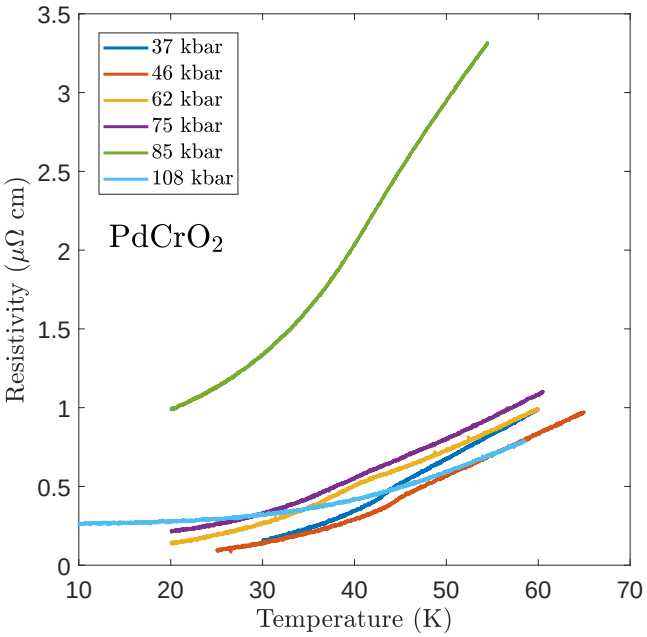

Fig. 6.16 Resistivity measurement in $PdCrO_2$ from 37 kbar to 108 kbar.

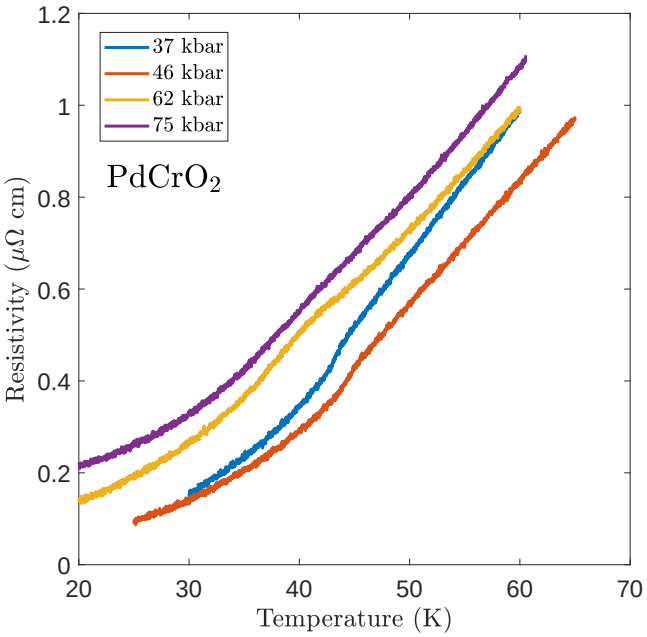

Fig. 6.17 Resistivity measurement in $PdCrO_2$ from 37 kbar to 75 kbar.

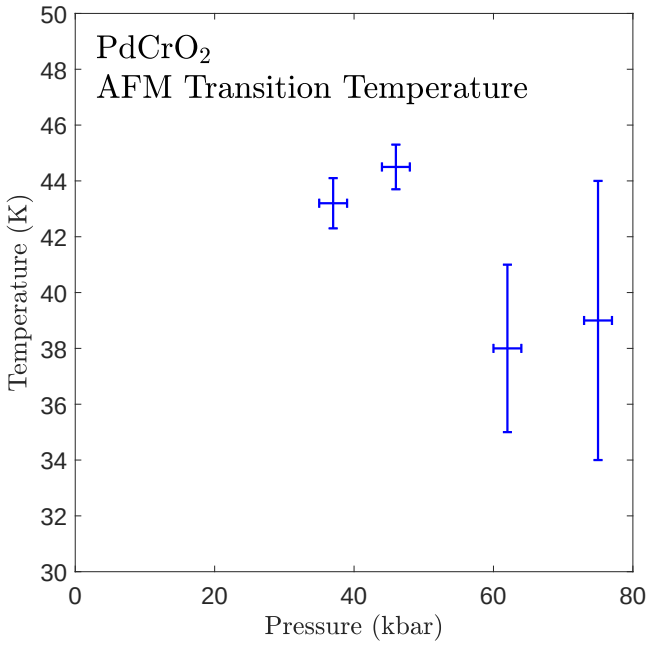

Fig. 6.18 Antiferromagnetic transition temperature of $PdCrO_2$ as a function of pressure.

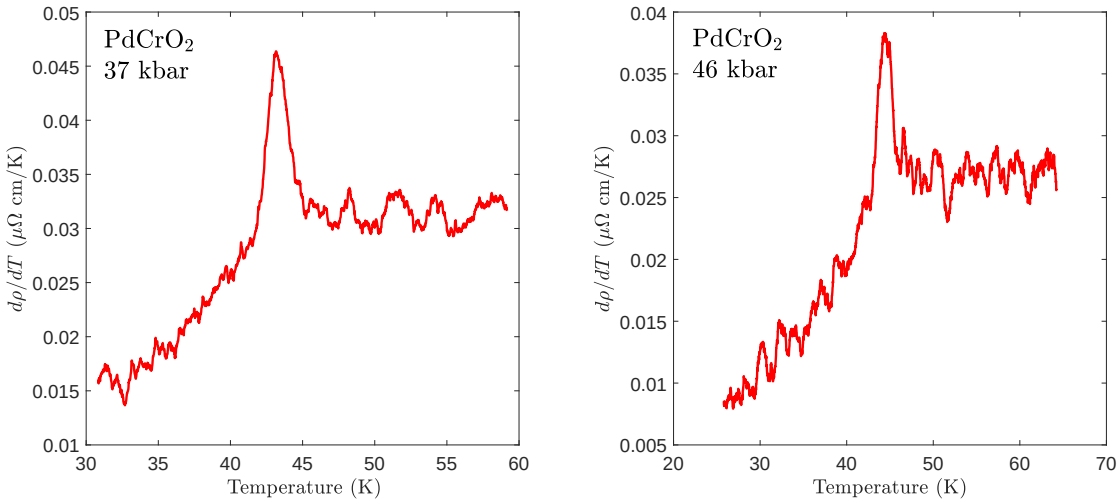

(a) 37 kbar

(b) 46 kbar

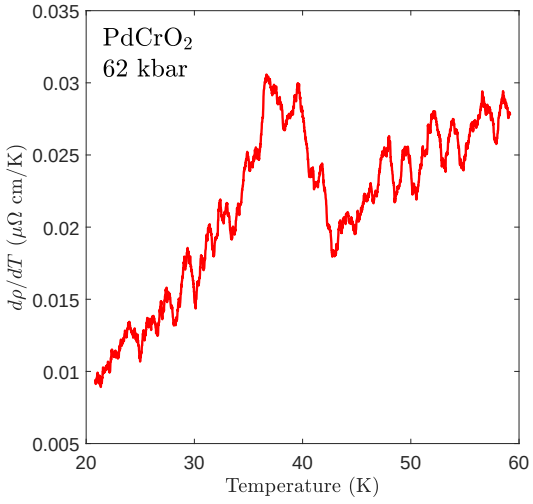

(c) 62 kbar

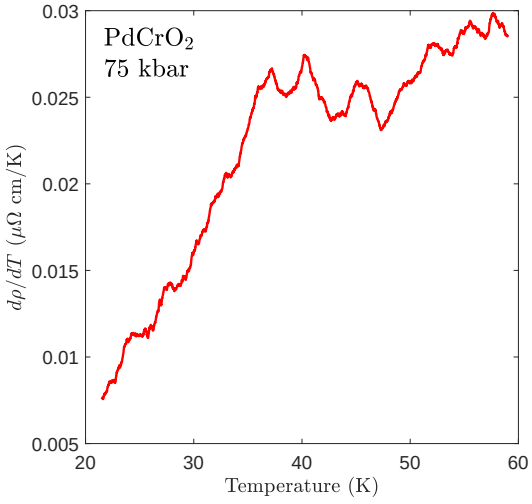

(d) 75 kbar

Fig. 6.19 Differential in resistivity with respect to the temperature of $PdCrO_2$ at different pressure.

6.3 Summary

In this chapter, we have presented our works on YFe_2Fe_2 and $PdCrO_2$.

In the YFe_2Fe_2 project, we studied an unconventional superconductor which is speculated to be in the quantum critical region. We have managed to suppress superconductivity and enter the Fermi liquid state. This result matches the high-pressure susceptibility measurement done previously, which also showed suppression in superconductivity. However, in our case, we still observed a slight trace of superconductivity, even at the pressure as high as 79 kbar, suggesting some filament of the superconducting left. The power-law study shows the cross-over from non-Fermi liquid ($n \sim 1.5 - 1.6$) at ambient pressure to Fermi liquid ($n \sim 1.9 - 2.0$) at pressure about 80 kbar.

Then, we explored high-pressure $PdCrO_2$, which is entirely new. We could track the antiferromagnetic transition of the frustrated lattice up to 75 kbar. However, the transition temperature is very insensitive to external pressure. At 85 kbar, the low-temperature resistivity suddenly by a factor of 5-10 compared to the lower pressure resistivity at the same temperature, suggesting the presence of a new unknown phase. A thorough study of this phase in the future is desirable, especially to study power-law behaviour and also explore the sub-Kelvin regime at this pressure.

Chapter 7

Outlook

Further Evidence of Aubry's Transition in Sb-II

Incommensurate host-guest antimony (Sb-II) is unexpectedly different from incommensurate host-guest bismuth (Bi-III). At low temperature, antimony shows a quadratic relationship between resistivity and temperature whereas the relationship is linear in bismuth. Moreover, there is a well-defined first-order phase transition at high temperature in Sb-II, which was not observed in Bi-III. These, in themselves, are very interesting since both materials have the same crystal and electronic structure. We proposed the solution to these discrepancies by interpreting that Sb-II undergoes a symmetry-breaking transition (i.e. Aubry's transition) at temperature below room temperature.

This Aubry's transition is intriguing since it has never been observed in any real materials before (although the transition has been observed already in optical lattices [24, 30]). One of the reasons why it is very difficult to observe in a real material is that incommensurate host-guest structure is relatively rare to find, and many of them require exceedingly high pressure to access this phase.

To investigate more whether Aubry's transition really happens in Sb-II, the list of possible further experiments are:

- High-pressure low-temperature x-ray diffraction, which will resolve low-temperature Sb-II structure and give us more insight into the anomalous transition at about 250 K.
- High-pressure heat capacity measurements in Bi-III and Sb-II. In the case of Bi-III, we may expect to see a very small Debye temperature due to a significant contribution of phason mode. With the phason-pinning in mind, we anticipate Sb-II to have a relatively large Debye temperature. However, the heat capacity measurement in Sb-II will be

very difficult as we require at least 86 kbar of pressure. In this case, we may need to use thermocouple technique, in which it is not possible to obtain the absolute value of heat capacity.

Antiferromagnetic in High-Pressure Ca_2RuO_4

The observation of the change in power-law exponent of resistivity has led us to the speculation of a possible antiferromagnetic phase at a pressure above 100 kbar. Since the superconducting phase was observed at the border of ferromagnetism, it was believed that the pairing mechanism must due to the presence of ferromagnetic correlation, hence spin-triplet pairing. The antiferromagnetic phase has changed our understanding of this material and the nature of superconductivity in Ca_2RuO_4 completely. In term of pairing mechanism, due to our results, electrons should from a pair in a spin-singlet channel rather than spin-triplet. Moreover, the antiferromagnetic implies that there is a strong competition between ferromagnetic and antiferromagnetic interaction, which can be fine-tuned by hydrostatic pressure.

As we go to higher and higher pressure, we should expect the complete suppression of antiferromagnetic (due to stronger fluctuations). In this view, it may be possible to have a quantum critical point at very high pressure, and we might be able to observe the rise in transition temperature in superconductivity, which may make Ca_2RuO_4 becomes another high-T_c superconductor at high pressure.

A list of potential future experiments are:

- Higher pressure studies of the superconducting transition. This can be done in resistivity measurement or AC susceptibility measurement in diamond anvil cell. To see the substantial change in superconducting transition temperature, we may need to go to pressure higher than 200 kbar.

- High-pressure neutron scattering: this will provide the direct evidence of any magnetic ordering in the material.

- As mentioned in the introduction section in Chapter 5, there is a metamagnetic transition at magnetic field of about 9 T. In such a high quality sample as the one we currently have, it would be possible to observe the quantum oscillation close to the meta magnetic transition. This would also be a great opportunity to study the quantum oscillatory phenomena in correlated insulating state.

Ambient Pressure Quantum Critical Point YFe_2Ge_2

In this project, we have successfully answered the origin of the unusual power-law exponent in normal state resistivity of YFe_2Ge_2. The suppression of superconductivity and the recovery of Fermi liquid led us to the interpretation that YFe_2Ge_2 is located right at the quantum critical point at ambient pressure. The fact that YFe_2Ge_2 is in non-Fermi liquid state above quantum critical point would allow us to do definitive studies on the quantum oscillatory phenomena in non-Fermi liquid state. This study was not possible before because (1) to access the non-Fermi liquid state, we need to do doping or applying pressure to a sample. This will cause impurity or inhomogeneity to a sample. which will smear out any possible quantum oscillation. (2) YFe_2Ge_2 is our in-house grown sample, which is now possible to grow a single crystal with residual resistivity ratio of above 600. This means that it would be possible to observe the quantum oscillation at very low enough field, where we are still in the non-Fermi liquid state. Therefore, the quantum oscillation study in the non-Fermi liquid state in YFe_2Ge_2 would give us the opportunity to understand the microscopic physics of non-Fermi liquid for the first time.

Furthermore, the experiment to prove the quantum criticality in YFe_2Ge_2 is the uniaxial strain experiment. The quantum criticality without quantum tuning is observed in very few materials such as $YbAlB_4$ [104], which is still currently under debates. Therefore, it would also be a good opportunity to have another material that exhibits similar behaviour to extend our understanding.

Further Studies of High-Pressure Phase in $PdCrO_2$

As $PdCrO_2$ has an unusual antiferromagnetic ordering at low temperature with two-dimensional in nature, it would be possible to have superconductivity emerges from a point where antiferromagnetic ordering is completely suppressed. However, as the antiferromagnetic transition temperature only changes slightly up to 75 kbar of pressure, the required pressure to suppressed the antiferromagnetic ordering might be much higher than 100 kbar. Some possible future experiments are:

- High-pressure resistivity measurement using better pressure medium (e.g. ethanol-methanol mixture or a noble gas such as argon). This will allow us to track the antiferromagnetic transition at high pressure

- High-pressure AC susceptibility: it is easier to go to high pressure in AC susceptibility then in resistivity. This will allow us to investigate any possibility of superconductivity at higher pressure.

References

[1] Abrikosov, A. A. (1988). *Fundamentals of The Theory of Metals*. Dover Publications.

[2] Agterberg, D. F., Rice, T. M., and Sigrist, M. (1997). Orbital dependent superconductivity in Sr_2RuO_4. *Physical Review Letters*, 78(17):3374–3377.

[3] Alireza, P. L. (2003). High-pressure studies of calcium rethenate. *PhD Dissertation, University of Cambridge*.

[4] Alireza, P. L., Nakamura, F., Goh, S. K., Maeno, Y., Nakatsuji, S., Ko, Y. T. C., Sutherland, M., Julian, S., and Lonzarich, G. G. (2010). Evidence of superconductivity on the border of quasi-2D ferromagnetism in Ca_2RuO_4 at high pressure. *Journal of Physics Condensed Matter*, 22(052202).

[5] Altland, A. and Simons, B. (2013). *Condensed Matter Field Theory (Second Edition)*. Cambridge University Press.

[6] Andersen, N. H. and Smith, H. (1979). Electron-magnon interaction and the electrical resistivity of Tb. *Physical Review B*, 19(1):384–387.

[7] Anderson, P. W. (1973). Resonating Valence Bonds: A New Kind of Insulator? *Mat. Res. Bull.*, 8(February):153–160.

[8] Aoki, K., Fujiwara, S., and Kusakabe, M. (1983). New Phase Transition Into The BCC Structure in Antimony at High Pressure. *Solid State Communications*, 45(2):161–163.

[9] Arapan, S., Mao, H. K., and Ahuja, R. (2008). Prediction of incommensurate crystal structure in Ca at high pressure. *Proceedings of the National Academy of Sciences of the United States of America*, 105(52):20627–20630.

[10] Armitage, N. P. (2019). Superconductivity mystery turns 25. *Nature*, 576(7787):386–387.

[11] Ashcroft, N. (1968). Metallic Hydrogen: A High-Temperature Superconductor? *Physical Review Letters*, 21(26):1748–1749.

[12] Ashcroft, N. W. and Mermin, N. D. (2021). *Solid state physics*. Cengage Learning.

[13] Aubry, S. and André, G. (1980). Analyticity breaking and Anderson localization in incommensurate lattices. *Ann. Israel Phys. Soc*, 3(133):133–164.

[14] Balents, L. (2010). Spin liquids in frustrated magnets. *Nature*, 464(7286):199–208.

[15] Balla, D. and Brandt, N. B. (1965). Investigation of the effect of uniform compression on the temperature dependence of the electrical Conductivity of bismuth. *Soviet Physics JETP*, 20(5):1111–1117.

[16] Bang, Y. and Stewart, G. R. (2017). Superconducting properties of the s± wave state: Fe-based superconductors. *Journal of Physics Condensed Matter*, 29(123003).

[17] Bednorz, J. G. and Müller, K. A. (1986). Possible High T c Superconductivity in the Ba-La-Cu-O System. *Zeitschrift für Physik B Condensed Matter and Quanta*, 64:189–193.

[18] Behnia, K., Balicas, L., and Kopelevich, Y. (2007). Signatures of electron fractionalization in ultraquantum bismuth. *Science*, 317(5845):1729–1731.

[19] Belitz, D. and Kirkpatrick, T. R. (1999). First order transitions and multicritical points in weak itinerant ferromagnets. *Physical Review Letters*, 82(23):4707–4710.

[20] Binz, B., Vishwanath, A., and Aji, V. (2006). Theory of the helical spin crystal: A candidate for the partially ordered state of MnSi. *Physical Review Letters*, 96(207202).

[21] Blundell, S. (2014). *Magnetism in Condensed Matter*. Oxford University Press.

[22] Braden, M. and André, G. (1998). Crystal and magnetic structure of Magnetoelastic coupling and the metal-insulator transition. *Physical Review B*, 58(2):847–861.

[23] Brandt, N. B., Gaidukov, Y. P., Itskevich, E. S., and Minina, N. Y. (1965). Influence of pressure on oscillation effects in bismuth. *Soviet Physics JETP*, 20(2):301–306.

[24] Brazda, T., Silva, A., Manini, N., Vanossi, A., Guerra, R., Tosatti, E., and Bechinger, C. (2018). Experimental Observation of the Aubry Transition in Two-Dimensional Colloidal Monolayers. *Physical Review X*, 8(011050).

[25] Bridgman, P. W. et al. (1952). *Physics of high pressure*. G. Bell.

[26] Brinkman, W. F. and Engelsberg, S. (1968). Spin-Fluctuation Contributions to the Specific Heat. *Physical Review*, 169(2).

[27] Brown, P. (2017). High-pressure states of bismuth. *PhD Dissertation, University of Cambridge*.

[28] Brown, P., Semeniuk, K., Vasiljkovic, A., and Grosche, F. M. (2015). Pressure-induced Semimetal-to-Semiconductor Transition in Bismuth. *Physics Procedia*, 75:29–33.

[29] Brown, P., Semeniuk, K., Wang, D., Monserrat, B., Pickard, C. J., and Grosche, F. M. (2018). Strong coupling superconductivity in a quasiperiodic host-guest structure. *Science Advances*, 4(4).

[30] Bylinskii, A., Gangloff, D., Counts, I., and Vuletić, V. (2016). Observation of Aubry-type transition in finite atom chains via friction. *Nature Materials*, 15:717–721.

[31] Castelnovo, C., Moessner, R., and Sondhi, S. L. (2008). Magnetic monopoles in spin ice. *Nature*, 451(7174):42–45.

[32] Chang, H. (2016). High Pressure Quantum Oscillation Study of the Mott Insulator NiS_2. *PhD Dissertation, University of Cambridge*.

[33] Chen, A. L., Lewis, S. P., Su, Z., Yu, P. Y., and Cohen, M. L. (1992). Superconductivity in arsenic at high pressures. *Physical Review B*, 46(9):5523–5527.

[34] Chen, J. (2019). Unconventional superconductivity in the layered iron germanide YFe_2Ge_2. *PhD Dissertation, University of Cambridge*.

[35] Chen, J., Semeniuk, K., Feng, Z., Reiss, P., Brown, P., Zou, Y., Logg, P. W., Lampronti, G. I., and Grosche, F. M. (2016). Unconventional Superconductivity in the Layered Iron Germanide YFe_2Ge_2. *Physical Review Letters*, 116(127001).

[36] Chen, X. H., Wu, T., Wu, G., Liu, R. H., Chen, H., and Fang, D. F. (2008). Superconductivity at 43 K in $SmFeAsO_{1-x}F_x$. *Nature*, 453(7196):761–762.

[37] Chu, C. W., Chen, F., Gooch, M., Guloy, A. M., Lorenz, B., Lv, B., Sasmal, K., Tang, Z. J., Tapp, J. H., and Xue, Y. Y. (2009). The synthesis and characterization of LiFeAs and NaFeAs. *Physica C: Superconductivity and its Applications*, 469(9-12):326–331.

[38] Chubukov, A. and Hirschfeld, P. J. (2015). Iron-based superconductors, seven years later. *Physics Today*, 68(6):46–52.

[39] Coak, M. (2017). Quantum tuning and emergent phases in charge and spin ordered materials. *PhD Dissertation, University of Cambridge*.

[40] Coak, M. J., Liu, C., Jarvis, D. M., Park, S., Cliffe, M. J., and Goddard, P. A. (2020). SquidLab - A user-friendly program for background subtraction and fitting of magnetization data. *Review of Scientific Instruments*, 91(023901).

[41] Cokey, D. and Bedell, K. S. (1993). Nonanalytic Contributions to the Self-Energy and the Thermodynamics of Two-Dimensional Fermi Liquids. *Physical Review Letters*, 71(7):1043–1046.

[42] Coleman, A. L., Stevenson, M., McMahon, M. I., and Macleod, S. G. (2018). Phase diagram of antimony up to 31 GPa and 835 K. *Physical Review B*, 97(144107).

[43] Coleman, P. (2017). *Introduction to Many-Body Physics*. Cambridge University Press.

[44] Dasoundhi, M. K., Rajput, I., Kumar, D., and Lakhani, A. (2021). Extremely large linear magnetoresistance in antimony crystal. *Journal of Physics D: Applied Physics*, 54(195303).

[45] Degtyareva, O., McMahon, M. I., and Nelmes, R. J. (2004). Pressure-induced incommensurate-to-incommensurate phase transition in antimony. *Physical Review B - Condensed Matter and Materials Physics*, 70(184119).

[46] Deguchi, K., Mizuguchi, Y., Kawasaki, Y., Ozaki, T., Tsuda, S., Yamaguchi, T., and Takano, Y. (2011). Alcoholic beverages induce superconductivity in $FeTe_{1-x}S_x$. *Superconductor Science and Technology*, 24(055008).

[47] Design, Q. (2004a). Distorted low-level signal readback of AC signals in the PPMS in the temperaturerange 25-35 K due to Inconel mitigation of inductive cross talk.

[48] Design, Q. (2004b). Physical Property Measurement System Hardware Manual.

[49] Dun, K. and Bundy, F. (1982). Pressure-induced superconductivity in strontium and barium. *Physical Review B*, 25(1):194–197.

[50] Dunstan, D. J. (1989). Theory of the gasket in diamond anvil high-pressure cells. *Review of Scientific Instruments*, 60(12):3789–3795.

[51] EI-Rahman, A. and Datars, W. R. (1986). Pressure Dependence of the Hole Fermi Surface Anisotropy in Antimony. *Journal of Low Temperature Physics*, 63:247–267.

[52] Eremin, I., Manske, D., Ovchinnikov, S. G., and Annett, J. F. (2004). Unconventional superconductivity and magnetism in Sr_2RuO_4 and related materials. *Annalen der Physik (Leipzig)*, 13(3):149–174.

[53] Fauqué, B., Yang, X., Tabis, W., Shen, M., Zhu, Z., Proust, C., Fuseya, Y., and Behnia, K. (2018). Magnetoresistance of semimetals: The case of antimony. *Physical Review Materials*, 2(114201).

[54] Fazekas, P. (2003). *Lecture Notes on Electron Correlation and Magnetism*. World Scientific Publishing.

[55] Fontes, M. B., Trochez, J. C., Giordanengo, B., Bud'ko, S. L., Sanchez, D. R., Baggio-Saitovitch, E. M., and Continentino, M. A. (1999). Electron-magnon interaction in RNiBC (R=Er, Ho, Dy, Tb, and Gd) series of compounds based on magnetoresistance measurements. *Physical Review B*, 60(9):6781–6789.

[56] Fujiwara, T., Aso, N., Yamamoto, H., Hedo, M., Saiga, Y., Nishi, M., Uwatoko, Y., and Hirota, K. (2007). Pressure effect on magnetic short range ordering of $LuFe_2Ge_2$. *Journal of the Physical Society of Japan*, 76:60–61.

[57] Ghosh, S., Shekhter, A., Jerzembeck, F., Kikugawa, N., Sokolov, D. A., Brando, M., Mackenzie, A. P., Hicks, C. W., and Ramshaw, B. J. (2021). Thermodynamic evidence for a two-component superconducting order parameter in Sr_2RuO_4. *Nature Physics*, 17(2):199–204.

[58] Goh, S. K., Alireza, P. L., Klintberg, L. E., Murphy, T., Nakamura, F., Singh, D. J., and Sutherland, M. (2012). Quantum Oscillations in the High Pressure Metallic State of Ca_2RuO_4. *arXiv*.

[59] Gough, H. J. and Cox, H. L. (1930). The Behaviour of a Single Crystal of Antimony subjected to Alternating Torsional Stresses. *Proceeding of The Royal Society A*, CXXVII:431–453.

[60] Grimvall, G. (1981). *The electron-phonon interaction in metals*. North-Holland Publisher.

[61] Hartstein, M., Liu, H., Hsu, Y.-T., Tan, B. S., Hatnean, M. C., Balakrishnan, G., and Sebastian, S. E. (2020). Intrinsic Bulk Quantum Oscillations in a Bulk Unconventional Insulator SmB_6. *iScience*, 23(11):101632.

[62] Hastings, J. M., Pouget, J. P., Shirane, G., Heeger, A. J., Miro, N. D., and Macdiarmid, A. G. (1977). One-Dimensional Phonons and Phase-Ordering Phase Transition in $Hg_{3-d}AsF_6$. *Physical Review Letters*, 39(23):1484–1487.

[63] Hicks, C. W., Gibbs, A. S., Zhao, L., Kushwaha, P., Borrmann, H., Mackenzie, A. P., Takatsu, H., Yonezawa, S., Maeno, Y., and Yelland, E. A. (2015). Quantum oscillations and magnetic reconstruction in the delafossite $PdCrO_2$. *Physical Review B*, 92(014425).

[64] Hicks, C. W., Kirtley, J. R., Lippman, T. M., Koshnick, N. C., Huber, M. E., Maeno, Y., Yuhasz, W. M., Maple, M. B., and Moler, K. A. (2010). Limits on superconductivity-related magnetization in Sr_2RuO_4 and $PrOs_4Sb_{12}$ from scanning SQUID microscopy. *Physical Review B*, 81(214501).

[65] Hirschfeld, P. J. (2016). Using gap symmetry and structure to reveal the pairing mechanism in Fe-based superconductors. *Comptes Rendus Physique*, 17(1-2):197–231.

[66] Hofmann, P. (2006). The surfaces of bismuth: Structural and electronic properties. *Progress in Surface Science*, 81(5):191–245.

[67] Ishida, K., Mukuda, H., Kitaoka, Y., Asayama, K., Mao, Z. Q., Mori, Y., and Maeno, Y. (1998). Spin-triplet superconductivity in Sr_2RuO_4 identified by O_{17} Knight shift. *Nature*, 396:658–660.

[68] Itskevich, E. and Fisher, L. (1967). Change of the Parameters of the Electron Energy Spectrum in Bismuth Under Pressure. *Soviet Physics JETP*, 26(6):1072–1074.

[69] Itskevich, E., Krechetova, I., and Fisher, L. (1967). Deformation of the Bismuth Fermi Surface by Pressures to to 8 kbar. *Soviet Physcs JETP*, 25(1):41–44.

[70] Iwasaki, H. and Kikegawa, T. (1986). Pressure-Induced Phase Transition In Antimony at Elevated Temperatures. *Physica B*, 139:259–262.

[71] Jaggi, R., Jain, A., and Weibel, H. (1963). Pressure dependence of the galvanomagnetic effects in bismuth. *Physics Letters*, 7(3):181–182.

[72] Jaoui, A., Fauque, B., and Behnia, K. (2021). Thermal resistivity and hydrodynamics of the degenerate electron fluid in antimony. *Nature Communications*, 12(195).

[73] Jo, N. H., Wu, Y., Wang, L. L., Orth, P. P., Downing, S. S., Manni, S., Mou, D., Johnson, D. D., Kaminski, A., Bud'Ko, S. L., and Canfield, P. C. (2017). Extremely large magnetoresistance and Kohler's rule in $PdSn_4$: A complete study of thermodynamic, transport, and band-structure properties. *Physical Review B*, 96(165145).

[74] Jones, C. K., Hulm, J. K., and Chandrasekhar, B. S. (1964). Upper critical field of solid solution alloys of the transition elements. *Reviews of Modern Physics*, 36(1):74–76.

[75] Kakehashi, Y. and Fulde, P. (2005). Marginal fermi liquid theory in the Hubbard model. *Physical Review Letters*, 94(156401).

[76] Kallin, C. (2012). Chiral p-wave order in Sr_2RuO_4. *Reports on Progress in Physics*, 75(042501).

[77] Kamihara, Y., Hiramatsu, H., Hirano, M., Kawamura, R., Yanagi, H., Kamiya, T., and Hosono, H. (2006). Iron-based layered superconductor: LaOFeP. *Journal of the American Chemical Society*, 128(31):10012–10013.

[78] Kamihara, Y., Watanabe, T., Hirano, M., and Hosono, H. (2008). Iron-Based Layered Superconductor $LaO_{1-x}F_xFeAs$ (x = 0 .05 - 0.12) with $T_c = 26$ K. pages 3296–3297.

[79] Katoh, K., Maeda, M., Matsuda, S., and Ochiai, A. (1997). Magnetic and transport properties of single-crystal Ca_2RuO_4: Relationship to superconducting Sr_2RuO_4. *Physical Review B*, 56(6):2916–2919.

[80] Kreisel, A., Hirschfeld, P. J., and Andersen, B. M. (2020). On the remarkable superconductivity of fese and its close cousins. *Symmetry*, 12(9):1–72.

[81] Longo, J. M., Raccah, P. M., and Goodenough, J. B. (1968). Magnetic Properties of $SrRuO_3$ and $CaRuO_3$. *Journal of Applied Physics*, 39(2):1327–1328.

[82] Lonzarich, G. (1997). *Electron: A Centenary Volume (Chapter 6 - The Magnetic Electron)*. Cambridge University Press.

[83] Mackenzie, A. P., Haselwimmer, R. K., Tyler, A. W., Lonzarich, G. G., Mori, Y., Nishizaki, S., and Maeno, Y. (1998). Extremely Strong Dependence of Superconductivity on Disorder in Sr_2RuO_4. *Physical Review Letters*, 80(1):161–164.

[84] Mackenzie, A. P. and Maeno, Y. (2003). The superconductivity of Sr_2RuO_4 and the physics of spin-triplet pairing. *Reviews of Modern Physics*, 75(2):657–712.

[85] Mackenzie, A. P., Scaffidi, T., Hicks, C. W., and Maeno, Y. (2017). Even odder after twenty-three years: The superconducting order parameter puzzle of Sr_2RuO_4. *NPJ Quantum Materials*, 2(40).

[86] Marino, E. C. (2017). *Quantum Field Theory Approach To Condensed Matter Physics*. Cambridge University Press.

[87] Masahiko Hatatani, T. M. (1995). Ferromagnetic Spin Fluctuation in Two-Dimensional Metals. *Journal of the Physical Society of Japan*, 64(9):3434–3441.

[88] Mazin, I. I. and Singh, D. J. (1997). Ferromagnetic spin fluctuation induced superconductivity in Sr_2RuO_4. *Physical Review Letters*, 79(4):733–736.

[89] Mazin, I. I. and Singh, D. J. (1999). Competitions in layered ruthenates: Ferromagnetism versus antiferromagnetism and triplet versus singlet pairing. *Physical Review Letters*, 82(21):4324–4327.

[90] McMahon, M., Bovornratanaraks, T., Allan, D., Belmonte, S., and Nelmes, R. (2000). Observation of the incommensurate barium-IV structure in strontium phase V. *Physical Review B - Condensed Matter and Materials Physics*, 61(5):3135–3138.

[91] Mcmahon, M. and Nelmes, R. (2004). Incommensurate crystal structures in the elements at high pressure. *Zeitschrift für Kristallographie - Crystalline Materials*, 219(11).

[92] McMahon, M. I. and Nelmes, R. J. (2004). Chain melting in the composite Rb-IV structure. *Physical Review Letters*, 93(055501).

[93] McWhan, D. B. (1972). The Pressure Variable in Materials Research. *Science*, 176(4036):751–758.

[94] Mekata, M., Sugino, T., Oohara, A., Oohara, Y., and Yoshizawa, H. (1995). Magnetic structure of antiferromagnetic $PdCrO_2$ possible degenerate helices on a rhombohedral lattice. *Physica B*, 213-214(C):221–223.

[95] Minelli, A., Souliou, S. M., Nguyen-Thanh, T., Romero, A. H., Serrano, J., Hernandez, W. I., Verstraete, M. J., Dmitriev, V., and Bosak, A. (2019). Lattice dynamics and phase stability of rhombohedral antimony under high pressure. *Physical Review B*, 100(104305).

[96] Minina, N. Y. and Lavrova, V. V. (1969). Effect of Pressure on The Shubnikiv-de Haas Effect in Antimony. *Soviet Physics JETP*, 30(2):354–361.

[97] Moll, P. J. W., Kushwaha, P., Nandi, N., Schmidt, B., and Mackenzie, A. P. (2016). Evidence for hydrodynamic electron flow in $PdCoO_2$. *Science*, 351(6277):1061–1064.

[98] Monthoux, P. and Lonzarich, G. G. (1999). P-wave and d-wave superconductivity in quasi-two-dimensional metals. *Physical Review B - Condensed Matter and Materials Physics*, 59(22):14598–14605.

[99] Moodenbaugh, A. R. and Fisk, Z. (1973). The electrical resistivity of barium and yttrium at high pressure. *Physics Letters A*, 43(6):479–480.

[100] Moriya, T. and Ueda, K. (2003). Antiferromagnetic spin fluctuation and superconductivity. *Rep. Prog. Phys.*, 66:1299–1341.

[101] Nakamura, F., Goko, T., Ito, M., Fujita, T., Nakatsuji, S., Fukazawa, H., Maeno, Y., Alireza, P., Forsythe, D., and Julian, S. R. (2002). From Mott insulator to ferromagnetic metal: A pressure study of Ca_2RuO_4. *Physical Review B*, 65(220402).

[102] Nakamura, F., Sakaki, M., Yamanaka, Y., Tamaru, S., Suzuki, T., and Maeno, Y. (2013). Electric-field-induced metal maintained by current of the Mott insulator Ca2RuO4. *Scientific Reports*, 3(2536).

[103] Nakatsuji, S., Dobrosavljević, V., Tanasković, D., Minakata, M., Fukazawa, H., and Maeno, Y. (2004). Mechanism of hopping transport in disordered mott insulators. *Physical Review Letters*, 93(146401).

[104] Nakatsuji, S., Kuga, K., Machida, Y., Tayama, T., Sakakibara, T., Karaki, Y., Ishimoto, H., Yonezawa, S., Maeno, Y., Pearson, E., Lonzarich, G. G., Balicas, L., Lee, H., and Fisk, Z. (2008). Superconductivity and quantum criticality in the heavy-fermion system $\beta - YbAlB_4$. *Nature Physics*, 4:603–607.

[105] Nakatsuji, S. and Maeno, Y. (2000). Quasi-Two-Dimensional Mott Transition System $Ca_{2-x}Sr_xRuO_4$. *Physical Review Letters*, 84(12):2666–2669.

[106] Nandi, N., Scaffidi, T., Kushwaha, P., et al. (2018). Unconventional magneto-transport in ultrapure $PdCoO_2$ and PtCoO2. *Nature Quantum Materials*, 3(66).

[107] Ong, T., Coleman, P., and Schmalian, J. (2016). Concealed d-wave pairs in the s± condensate of iron-based superconductors. *Proceedings of the National Academy of Sciences of the United States of America*, 113(20):5486–5491.

[108] Opila, E. J., Tuller, H. L., Wuensch, B. J., and Maier, J. (1993). Oxygen Tracer Diffusion in $La_{2-x}Sr_xCuO_{4-y}$ Single Crystals. *Journal of the American Ceramic Society*, 76(9):2363–2369.

[109] Ostrikov, O. M. and Dub, S. N. (2003). Investigation of the mechanical twinning of antimony single crystals by nanoindentation. *Inzhenerno-Fizicheskii Zhurnal*, 76(1):170–172.

[110] Paglione, J. and Greene, R. L. (2010). High-temperature superconductivity in iron-based materials. *Nature Physics*, 6:645–658.

[111] Pfleiderer, C., Julian, S. R., and Lonzarich, G. G. (2001). Non-Fermi-liquid nature of the normal state of itinerant-electron ferromagnets. *Nature*, 414(6862):427–430.

[112] Pfleiderer, C., Reznik, D., Pintschovius, L., Löhneysen, H. V., Garst, M., and Rosch, A. (2004). Partial order in the non-Fermi-liquid phase of MnSi. *Nature*, 427(6971):227–231.

[113] Pippard, B. (1989). *Magnetoresistance in Metals*. Cambridge University Press.

[114] Pudalov, V. M. (2011). David Shoenberg and the beauty of quantum oscillations. *Low Temperature Physics*, 37(1):8–18.

[115] Pugh, E., Steiner, M. J., Forsythe, D., Walker, R., Saxena, S. S., Julian, S. R., Lonzarich, G. G., Mackenzie, A. P., Nishizaki, S., and Maeno, Y. (2004). Resistivity measurements on Sr_2RuO_4 under pressure. *Journal of Magnetism and Magnetic Materials*, 272-276:2003–2004.

[116] Pustogow, A., Luo, Y., Chronister, A., Su, Y. S., Sokolov, D. A., Jerzembeck, F., Mackenzie, A. P., Hicks, C. W., Kikugawa, N., Raghu, S., Bauer, E. D., and Brown, S. E. (2019). Constraints on the superconducting order parameter in Sr_2RuO_4 from oxygen-17 nuclear magnetic resonance. *Nature*, 574:72–75.

[117] Pustovit, Y. V. and Kordyuk, A. A. (2016). Metamorphoses of electronic structure of FeSe-based superconductors (Review Article). *Low Temperature Physics*, 42(11):995–1007.

[118] Ran, S., Bud'Ko, S. L., and Canfield, P. C. (2011). Effects of substitution on low-temperature physical properties of $LuFe_2Ge_2$. *Philosophical Magazine*, 91(34):4388–4400.

[119] Ren, Z. A., Che, G. C., Dong, X. L., Yang, J., Lu, W., Yi, W., Shen, X. L., Li, Z. C., Sun, L. L., Zhou, F., and Zhao, Z. X. (2008). Superconductivity and phase diagram in iron-based arsenic-oxides $ReFeAsO_{1-\delta}$ (Re = rare-earth metal) without fluorine doping. *Epl*, 83(1):12–16.

[120] Rice, T. M. and Sigrist, M. (1995). Sr_2RuO_4 : an electronic analogue of ^{3}He? *Journal of Physics: Condensed Matter*, 7(47):638–648.

[121] Robinson, V. N., Zong, H., Ackland, G. J., Woolman, G., and Hermann, A. (2019). On the chain-melted phase of matter. *Proceedings of the National Academy of Sciences of the United States of America*, 116:10297–10302.

[122] Rogalla, H. and Kes, P. H. (2012). *100 years of superconductivity*. CRC Press/Taylor and Francis Group.

[123] Rotter, M., Tegel, M., and Johrendt, D. (2008). Superconductivity at 38 K in the iron arsenide $(Ba_{1-x}K_x)Fe_2As_2$. *Physical Review Letters*, 101(10):4–7.

[124] Sachdev, S. (2008). Quantum magnetism and criticality. *Nature Physics*, 4(3):173–185.

[125] Sachdev, S. (2011). *Quantum phase transitions*. Cambridge University Press.

[126] Sasmal, K., Lv, B., Lorenz, B., Guloy, A. M., Chen, F., Xue, Y. Y., and Chu, C. W. (2008). Superconducting Fe-based compounds $(A_{1-x}Sr_x)Fe_2As_2$ with A = K and Cs with transition temperatures up to 37 K. *Physical Review Letters*, 101(107007).

[127] Schwarz, U., Akselrud, L., Rosner, H., Ormeci, A., Grin, Y., and Hanfland, M. (2003). Structure and stability of the modulated phase Sb-II. *Physical Review B*, 67(214101).

[128] Semeniuk, K. (2018). Correlated low temperature states ofYFe_2Ge_2 and pressure metallised NiS_2. *PhD Dissertation, University of Cambridge*.

[129] Shechtman, D., Blech, I., Gratias, D., and Cahn, J. W. (1984). Metallic phase with long-range orientational order and no translational symmetry. *Physical Review Letters*, 53(20):1951–1953.

[130] Shoenberg, D. (2009). *Magnetic oscillations in metals*. Cambridge University Press.

[131] Smith, R. P., Sutherland, M., Lonzarich, G. G., Saxena, S. S., Kimura, N., Takashima, S., Nohara, M., and Takagi, H. (2008). Marginal breakdown of the Fermi-liquid state on the border of metallic ferromagnetism. *Nature*, 455:1220–1223.

[132] Snider, E., Dasenbrock-Gammon, N., Mcbride, R., Debessai, M., Vindana, H., Vencatasamy, K., Lawler, K. V., Salamat, A., and Dias, R. P. (2020). Room-temperature superconductivity in a carbonaceous sulfur hydride. *Nature*, 588(7837):373–377.

[133] Snow, C. S., Cooper, S. L., Cao, G., Crow, J. E., Fukazawa, H., Nakatsuji, S., and Maeno, Y. (2002). Pressure-Tuned Collapse of the Mott-Like State in $Ca_{n+1}Ru_nO_{3n+1}$ $(n = 1,2)$: Raman Spectroscopic Studies. *Physical Review Letters*, 89(226401).

[134] Spatek, J. and Oles, A. (1977). Ferromagnetism in narrow s-band with inclusion of intersite correlations. *Physica B+C*, 86-88:375–377.

[135] Steffens, P., Friedt, O., Alireza, P., Marshall, W. G., Schmidt, W., Nakamura, F., Nakatsuji, S., Maeno, Y., Lengsdorf, R., Abd-Elmeguid, M. M., and Braden, M. (2005). High-pressure diffraction studies on Ca_2RuO_4. *Physical Review B*, 72(094104).

[136] Struktur, Z. and As, V. K. (2014). Crystal Structure of KFe_2As_2, KCo_2As_2, KRh_2As_2. *Zeitschrift fur Naturforschung B*, 36(12):1668–1670.

[137] Sun, D., Sokolov, D. A., Bartlett, J. M., Sannigrahi, J., Khim, S., Kushwaha, P., Khalyavin, D. D., Manuel, P., Gibbs, A. S., Takagi, H., Mackenzie, A. P., and Hicks, C. W. (2019). Magnetic frustration and spontaneous rotational symmetry breaking in $PdCrO_2$. *Physical Review B*, 100(094414).

[138] Sutter, D., Fatuzzo, C. G., Moser, S., Kim, M., Fittipaldi, R., Vecchione, A., Granata, V., Sassa, Y., Cossalter, F., Gatti, G., Grioni, M., Rønnow, H. M., Plumb, N. C., Matt, C. E., Shi, M., Hoesch, M., Kim, T. K., Chang, T. R., Jeng, H. T., Jozwiak, C., Bostwick, A., Rotenberg, E., Georges, A., Neupert, T., and Chang, J. (2017). Hallmarks of Hunds coupling in the Mott insulator Ca_2RuO_4. *Nature Communications*, 8(15176).

[139] Syassen, K. (2008). Ruby under pressure. *High Pressure Research*, 28(2):75–126.

[140] Takatsu, H., Nénert, G., Kadowaki, H., Yoshizawa, H., Enderle, M., Yonezawa, S., Maeno, Y., Kim, J., Tsuji, N., Takata, M., Zhao, Y., Green, M., and Broholm, C. (2014). Magnetic structure of the conductive triangular-lattice antiferromagnet $PdCrO_2$. *Physical Review B*, 89(104408).

[141] Takatsu, H., Yonezawa, S., Michioka, C., Yoshimura, K., and Maeno, Y. (2010). Anisotropy in the magnetization and resistivity of the metallic triangular-lattice magnet $PdCrO_2$. *Journal of Physics: Conference Series*, 200(012198).

[142] Takatsu, H., Yoshizawa, H., Yonezawa, S., and Maeno, Y. (2009). Critical behavior of the metallic triangular-lattice Heisenberg antiferromagnet $PdCrO_2$. *Physical Review B*, 79(104424).

[143] Tateiwa, N. and Haga, Y. (2010). Appropriate pressure-transmitting media for cryogenic experiment in the diamond anvil cell up to 10 GPa. *Journal of Physics: Conference Series*, 215(012178).

[144] Tokiwa, Y., Bachus, S., Kavita, K., Jesche, A., Tsirlin, A. A., and Gegenwart, P. (2021). Frustrated magnet for adiabatic demagnetization cooling to milli-Kelvin temperatures. *Communications Materials*, 2(42).

[145] Tokura, Y. (2006). Critical features of colossal magnetoresistive manganites. *Reports on Progress in Physics*, 69(3):797–851.

[146] Tokura, Y., Tomioka, Y., Kuwahara, H., Asamitsu, A., Moritomo, Y., and Kasai, M. (1996). Origins of colossal magnetoresistance in perovskite-type manganese oxides (invited). *Journal of Applied Physics*, 79(8 PART 2A):5288–5291.

[147] Tokura, Y., Urushibara, A., Moritomo, Y., Arima, T., Asamitsu, A., Kido, G., and Furukawa, N. (1994). Giant Magnetotransport Phenomena in Filling-Controlled Kondo Lattice System $La_{1-x}Sr_xMnO_3$. *Journal of the Physical Society of Japan*, pages 3931–3935.

[148] Varma, C. M., Littlewood, P. B., Schmitt-Rink, S., Abrahams, E., and Ruckenstein, A. E. (1989). Phenomenology of the normal state of cu-o high-temperature superconductors. *Physical Review Letters*, 63(497):1996–1999.

[149] Vereshchagin, L. F. and Kabalkina, S. S. (1965). Phase transitions in antimony at high pressures. *High Pressure Research*, 33(1):158–164.

[150] Walker, I. R. (1999). Nonmagnetic piston-cylinder pressure cell for use at 35 kbar and above. *Review of Scientific Instruments*, 70(8):3402–3412.

[151] Wang, X., Kunc, K., Loa, I., Schwarz, U., and Syassen, K. (2006). Effect of pressure on the Raman modes of antimony. *Physical Review B*, 74(134305).

[152] Wang, X. C., Liu, Q. Q., Lv, Y. X., Gao, W. B., Yang, L. X., Yu, R. C., Li, F. Y., and Jin, C. Q. (2008). The superconductivity at 18 K in LiFeAs system. *Solid State Communications*, 148(11-12):538–540.

[153] Watson, C. A., Gibbs, A. S., Mackenzie, A. P., Hicks, C. W., and Moler, K. A. (2018). Micron-scale measurements of low anisotropic strain response of local Tc in Sr_2RuO_4. *Physical Review B*, 98(094521).

[154] Wells, A. F. (2012). *Structural Inorganic Chemistry*. Oxford University Press.

[155] Welzel, O. P. (2011). Transport Measurements of $Ca_3Ru_2O_7$ and $BaFe_2As_2$ using Micropatterned Anvils. *PhD Dissertation, University of Cambridge*.

[156] Wen, X.-G. (2010). *Quantum Field Theory of Many-Body Systems*. Oxford University Press.

[157] Wittig, J. (1969). A study of the superconductivity of antimony under pressure and a search for superconductivity in arsenic. *Solid State Communications*, 7(5):1407–1410.

[158] Wittig, J. and Matthias, B. T. (1969). Superconductivity of barium under pressure. *Physical Review Letters*, 22(13).

[159] Wo, H., Wang, Q., Shen, Y., Zhang, X., Hao, Y., Feng, Y., Shen, S., He, Z., Pan, B., Wang, W., Nakajima, K., Ohira-Kawamura, S., Steffens, P., Boehm, M., Schmalzl, K., Forrest, T. R., Matsuda, M., Zhao, Y., Lynn, J. W., Yin, Z., and Zhao, J. (2019). Coexistence of Ferromagnetic and Stripe-Type Antiferromagnetic Spin Fluctuations in YFe_2Ge_2. *Physical Review Letters*, 122(217003).

[160] Wu, M. K., Ashburn, J. R., Torng, C. J., Hor, P. H., Meng, R. L., Gao, L., Huang, Z. J., Wang, Y. Q., and Chu, C. W. (1987). Superconductivity at 93 K in a new mixed-phase Yb-Ba-Cu-O compound system at ambient pressure. *Physical Review Letters*, 58(9):908–910.

[161] Wu, W., Wang, X., and Tremblay, A.-M. (2021). Non-Fermi liquid phase and linear-in-temperature scattering rate in overdoped two dimensional Hubbard model. *arXiv*.

[162] Yabuuchi, T., Matsuoka, T., Nakamoto, Y., and Shimizu, K. (2006). Superconductivity of ca exceeding 25 k at megabar pressures. *Journal of the Physical Society of Japan*, 75(8):083703.

[163] Yamada, H. and Takada, S. (1972). Negative Magnetoresistance of Ferromagnetic Metals due to Spin Fluctuations. *Progress of Theoretical Physics*, 48(6):1828–1848.

[164] Yates, K. A., Usman, I. T., Morrison, K., Moore, J. D., Gilbertson, A. M., Caplin, A. D., Cohen, L. F., Ogino, H., and Shimoyama, J. (2010). Evidence for nodal superconductivity in $Sr_2ScFePO_3$. *Superconductor Science and Technology*, 23(022001).

[165] Yin, Y., Zech, M., Williams, T. L., Wang, X. F., Wu, G., Chen, X. H., and Hoffman, J. E. (2009). Scanning tunneling spectroscopy and vortex imaging in the iron pnictide superconductor $BaFe_{1.8}Co_{0.2}As_2$. *Physical Review Letters*, 102(097002).

[166] Y.Maeno (1994). Superconductivity in a layered perovskite without copper. *Nature*, 372(December):532–534.

[167] Zhang, S., Wu, Q., Liu, Y., and Yazyev, O. V. (2019). Magnetoresistance from Fermi surface topology. *Physical Review B*, 99(035124).

[168] Zou, Y., Feng, Z., Logg, P. W., Chen, J., Lampronti, G., and Grosche, F. M. (2014). Fermi liquid breakdown and evidence for superconductivity in YFe_2Ge_2. *Physica Status Solidi - Rapid Research Letters*, 8(11):928–930.